Aus dem
Lehrstuhl für Molekularbiologie, Biomedizinisches Centrum (BMC)
Institut der Ludwig-Maximilians-Universität München
Vorstand: Prof. Dr. Peter Becker

Making a Multiciliated Cell: The Role of SUV4-20H1 in Xenopus Multiciliogenesis

Dissertation

zum Erwerb des Doktorgrades der Naturwissenschaften
an der Medizinischen Fakultät der
Ludwig-Maximilians-Universität München

vorgelegt von
Janet Catherine Tait

aus
Toronto, Canada

Jahr
2024

Mit Genehmigung der Medizinischen Fakultät
der Ludwig-Maximilians-Universität München

Betreuter: Prof. Dr. Ralph A. W. Rupp

Zweitgutachter: Prof. Dr. André Werner Brändli

Dekan: Prof. Dr. med. Thomas Gudermann

Tag der mündlichen Prüfung: 24. Februar 2025

Affidavit

Tait, Janet

Surname, first name

I hereby declare, that the submitted thesis entitled

Making a Multiciliated Cell: The Role of SUV4-20H1 in Xenopus Multiciliogenesis

is my own work. I have only used the sources indicated and have not made unauthorised use of services of a third party. Where the work of others has been quoted or reproduced, the source is always given.

I further declare that the dissertation presented here has not been submitted in the same or similar form to any other institution for the purpose of obtaining an academic degree.

München, 26.08.2024

Place, Date

Janet Tait

Signature doctoral candidate

LMU LUDWIG-MAXIMILIANS-UNIVERSITÄT MÜNCHEN

Dekanat Medizinische Fakultät
Promotionsbüro

Confirmation of congruency between printed and electronic version of the doctoral thesis

Doctoral candidate: Janet Tait

I hereby declare that the electronic version of the submitted thesis, entitled

Making a Multiciliated Cell: The Role of SUV4-20H1 in Xenopus Multiciliogenesis

is congruent with the printed version both in content and format.

München, 26.08.2024 Janet Tait

Place, Date Signature doctoral candidate

List of Publications

Part of this dissertation has been published in an article entitled:

Angerilli, A.*, **Tait, J.***, Berges, J., Shcherbakova, I., Pokrovsky, D., Schauer, T. et al. The histone H4K20 methyltransferase SUV4-20H1/KMT5B is required for multiciliated cell differentiation in Xenopus. *Life Science Alliance* **6** (2023).

Summary

In the developing embryo, regulating gene expression is crucial to generate a vast array of cell types from a common genetic blueprint. One of the mechanisms by which this regulation is achieved is through methylation of lysine residues on histone tails. These marks are controlled by histone methyltransferases, demethylases, and reader proteins. Here, we explore a surprising link between a histone H4 lysine 20 (H4K20) methyltransferase, suv4-20h1/kmt5b, and multiciliated cells (MCCs).

MCCs are a highly specialized cell type found in the brain and respiratory tract of mammals and on the *Xenopus* embryonic epidermis. These cells are characterized by hundreds of motile cilia that beat to generate fluid flow, and impairment of MCC differentiation or function is implicated in a number of pathologies. Our lab previously discovered that double knockdown of suv4-20h1 and suv4-20h2/kmt5c, the enzymes that write H4K20me2/3, leads to a ciliogenic phenotype, which disrupts cilia formation in MCCs as a consequence of a concerted downregulation of ciliogenic genes.

In this thesis, we further investigate the relationship between H4K20 methylating enzymes and MCCs using *Xenopus* as a model system. Strikingly, we demonstrate that the transcription of ciliogenic genes is regulated by the catalytic activity of suv4-20h1 but not suv4-20h2. Chromatin in cells depleted of suv4-20h1 activity is enriched for H4K20me1, a modification with unclear impact on gene transcription. The cilia defects can be partially rescued by the catalytic activity of PHF8, an H4K20me1 demethylase. In contrast, overexpression of multicilin, the master regulator of multiciliogenesis, cannot rescue ciliogenic structure or gene expression, and expression of downstream ciliogenic regulators is not affected by suv4-20h1 knockdown. This indicates that suv4-20h1 regulates MCC differentiation through an alternative pathway to the canonical multiciliogenic transcription program. While our data suggest that the conversion from H4K20me1 to H4K20me2 by suv4-20h1 is needed for normal levels of ciliogenic gene expression, ATAC-Seq analysis indicates that suv4-20h1 has a minor effect on chromatin accessibility. These findings shed further light on the intriguing connection between a specialized cellular structure and the epigenetic landscape.

Zusammenfassung

Im sich entwickelnden Embryo ist die Regulierung der Genexpression von entscheidender Bedeutung für die Entstehung einer Vielzahl von Zelltypen auf der Grundlage eines gemeinsamen genetischen Bauplans. Einer der Mechanismen, mit dem diese Regulierung erreicht wird, ist die Methylierung von Lysinresten an Histonschwänzen. Diese Markierungen werden durch Histon-Methyltransferasen, Demethylasen und sog. „Reader"-Proteinen kontrolliert. Hier untersuchen wir eine überraschende Verbindung zwischen suv4-20h1/KMT5B, einer Histon-H4-Lysin-20 (H4K20)-Methyltransferase, und multizilierten Zellen.

Multizilierte Zellen sind ein hochspezialisierter Zelltyp, der im Gehirn und in den Atemwegen von Säugetieren sowie in der Epidermis von *Xenopus*-Embryonen vorkommt. Diese Zellen zeichnen sich durch Hunderte von beweglichen Zilien aus, deren Schlag einen gerichteten Flüssigkeitsstrom zu erzeugt. Eine Beeinträchtigung dieses Zilienapparats wird mit einer Reihe von Krankheiten in Verbindung gebracht. Unser Labor hat zuvor entdeckt, dass die gleichzeitige Depletion der Enzyme suv4-20h1 und suv4-20h2/kmt5c, die H4K20me2/3 Markierungen im Chromatin katalysieren, zu einem ciliogenen Phänotyp führt, der die Zilienbildung in multizilierten Zellen als Folge einer konzertierten Herunterregulierung von ciliogenen Genen unterbricht.

In dieser Arbeit untersuchen wir die Beziehung zwischen H4K20 methylierenden Enzymen und multizilierten Zellen im Modellorganismus *Xenopus*. Wir konnten zeigen, dass die Transkription von ciliogenen Genen ausschließlich durch die katalytische Aktivität von suv4-20h1, nicht aber von SUV4-20H2, reguliert wird. In Zellen, denen die suv4-20h1-Aktivität fehlt, ist das Chromatin mit H4K20me1 angereichert, eine Modifikation, deren Auswirkungen auf die Gentranskription unklar sind. Die Ziliendefekte können teilweise durch die katalytische Aktivität von PHF8, einer H4K20me1-Demethylase, behoben werden. Im Gegensatz dazu kann die Überexpression von Multicilin, dem Hauptregulator der Multiciliogenese, weder die ciliogene Struktur noch die Genexpression in retten, und die Expression nachgeschalteter ciliogener Regulatoren wird durch die Ausschaltung von suv4-20h1 nicht beeinflusst. Dies deutet darauf hin, dass suv4-20h1 die multizilierten Zellen-Differenzierung über einen alternativen Weg zum kanonischen multizilierten Zellen-Transkriptionsprogramm reguliert. Während unsere

Daten darauf hindeuten, dass die Umwandlung von H4K20me1 in H4K20me2 durch suv4-20h1 für ein normales Niveau der ciliogenen Genexpression erforderlich ist, zeigt die ATAC-Seq-Analyse, dass suv4-20h1 lediglich eine geringe Auswirkung auf die Chromatinzugänglichkeit hat. Die Ergebnisse sind wegbereitend für zukünftige Experimente, um die Verknüpfung zwischen einem hochspezialisierten Zellorganell und einem Histon modifizierenden Enzym mechanistisch aufzuklären.

TABLE OF CONTENTS

1

INTRODUCTION

One of the major revolutions in life sciences was the sequencing of the human genome. Access to the genetic code gave biologists a powerful tool for research and critical insights into the molecular basis of life. It was a watershed moment that led to advances in medical treatment, birthed new fields and technologies, and ushered in a new era of collaboration and open science. However, the human genome did not function as a perfect blueprint, yielding one-to-one solutions for genetic disease or providing a clear map of embryonic development. Instead, it revealed unforeseen layers of complexity and demonstrated that the DNA sequence itself is only one aspect of regulating genetic information. Many of these additional levels of genome regulation are driven by epigenetic mechanisms.

1.1 Epigenetics

Epigenetics is the study of changes to gene expression without changes to the underlying genetic sequence[1]. Epigenetic modifications are critical in coordinating the genome throughout an organism's life cycle and are particularly important for regulating development[2]. Even though each cell in a developing embryo contains the same genetic information, the embryo must generate a vast array of cell types, each with distinct function and morphology, from a totipotent zygote[3]. Epigenetic changes guide the cell through this transition by tightly controlling gene expression and conveying epigenetic information through the chromatin.

1.1.1 Chromatin dynamics

DNA is an immensely long molecule that must fit into a tiny compartment, the cell nucleus. The human genome stretched end to end is estimated to be two meters long, and the typical cell nucleus is closer to 10 μm in diameter[4]. Additionally, DNA must be organized so that

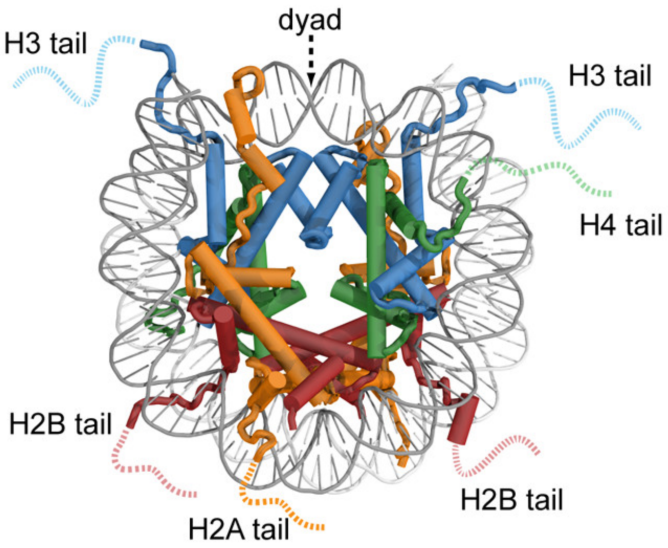

Figure 1.1: Nucleosome structure. The nucleosome consists of 147 base pairs of DNA wrapped around a core of histones. Adapted and reprinted with permission from ACS[7].

cellular machinery can access genes in a timely and tightly coordinated manner. To achieve this feat, DNA is highly compacted and organized into chromatin. Chromatin is the complex of biological molecules that package and regulate the genome of eukaryotes. It is located in the nucleus and comprises DNA, RNA, and proteins. The critical protein components of chromatin are histones, which act like molecular spools around which DNA is wound. Histones facilitate efficient packaging of DNA into the nucleus[5,6].

The functional unit of chromatin is the nucleosome, composed of 145-147 base pairs of DNA wrapped around an octameric core of histones (Figure 1.1)[5,6]. Histone octamers consist of two copies of canonical histones H2A, H2B, H3, and H4, and these can be replaced with histone variants, including H2A.Z and H2A.X for H2A, and H3.3 and CENP-A for H3[6]. Nucleosomes also include a small sequence of linker DNA bound by histone H1, which connects neighboring nucleosomes and generates the formation of the 30 nm fiber[8,9]. Chromatin is then arranged in loops and forms topologically associated domains (TADs), allowing long-range interactions between DNA and proteins that may not be close along the DNA sequence[10]. The levels of chromatin organization can be visualized in Figure 1.2.

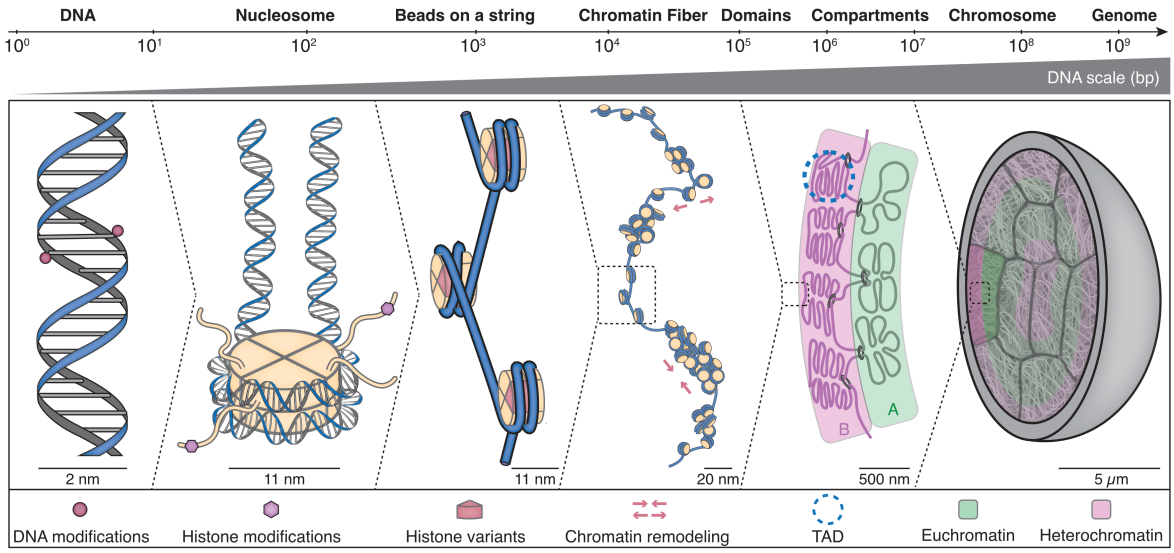

Figure 1.2: Chromatin Structure DNA is organized into many orders of structure. First, the DNA is wound around histones to form nucleosomes. Nucleosomal arrays form a "beads on a string" configuration, further compacted into the chromatin fiber. From there, chromatin goes on to form higher-order structures like topologically associated domains. Domains can then be organized into euchromatin and heterochromatin. Reprinted with permission from Dr. Christopher Mulholland.

There are generally two distinct states of chromatin: euchromatin and heterochromatin. These states differ in many aspects, including structure, degree of compaction, location in the chromatin, and histone modification context. Heterochromatin is highly condensed and tightly packed, making it less accessible to cellular regulators and transcriptionally silent[11,12]. Heterochromatin can be further split into two categories. Constitutive heterochromatin is enriched at the centromeric and telomeric repeats and on repetitive elements like tranposons[13,14]. Regardless of the cell type or developmental stage, these regions remain heavily compacted and repressed. Conversely, facultative heterochromatin typically encompasses genes expressed in a cell type-specific manner. These genes are stably repressed in specific cell types but can be switched on as required.

On the other hand, euchromatin is more loosely packed, making it accessible to transcriptional machinery. Euchromatin is generally found in gene-rich regions of the genome[15–17], including actively transcribed genes and regulatory elements like promoters and enhancers[18].

1.1.2 Histone post-translational modifications and the Histone Code

In addition to their role in packaging DNA, histones act as information hubs. Histones contain two domains, a globular core domain and an N-terminal tail domain, which can carry epigenetic information through post-translational modifications (PTMs)[6]. DNA and histone interactions are crucial drivers of many essential cellular processes, including transcription. Epigenetic modifications like DNA methylation and histone PTMs are necessary for regulating gene expression. A wide variety of histone modifications have been identified, including histone methylation, acetylation, phosphorylation, ubiquitylation, and SUMOylation[19]. Many sites of histone modifications are depicted in Figure 1.3.

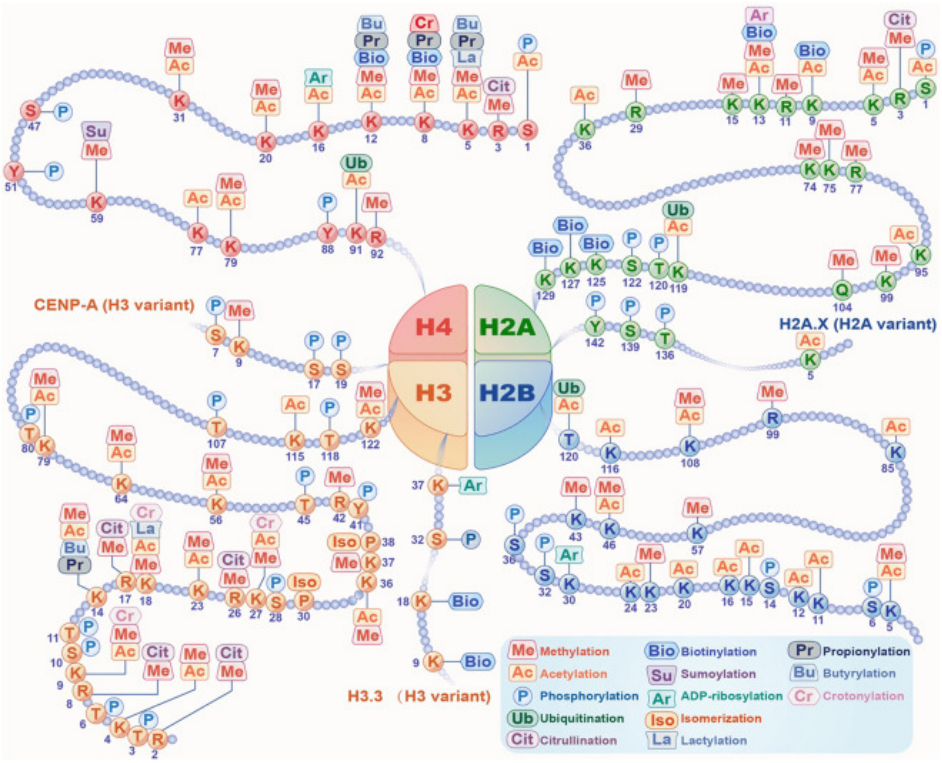

Figure 1.3: Histone modifications. Many potential histone modifications can be found on core histones and histone variants, including acetylation, methylation, phosphorylation, and sumoylation. Reprinted with permission from Elsevier[20].

Histone PTMs were first observed in the context of transcription in 1964 by Allfrey and Mirsky, who proposed that histone acetylation may be correlated to gene activation[21]. In the subsequent decades, histone methylation and acetylation were also discovered, but their

functions remained unknown[22]. In 1996, the connection between histone modifications and transcription was cemented with the discovery that a histone acetyltransferase was homologous to Gcn5, a transcriptional regulatory protein in yeast[23]. From those early findings came a surge in the identification of new histone marks and a recontextualization of those already known. From there, a "histone code" was first proposed. The histone code is the concept that specific combinations of histone modifications could be "read" to predict patterns of gene expression[12].

Today, it is clear that the functions of most individual histone modifications cannot be read on a one-to-one basis. The local context of a histone modification conveys essential information. For example, constitutive heterochromatin is characteristically marked by H3K9me3 and H4K20me3; facultative heterochromatin is defined by the presence of the polycomb mark, H3K27me3, and euchromatin is generally associated with histone acetylation and H3K4me3[16,24–27].

Different combinations of histone modifications at a particular site can also result in a different function. For example, bivalent promoters on ESCs exhibit transcriptionally active H3K4me3 and repressive H3K27me3[28]. Bivalent promoters tend to be found at lowly transcribed transcription factors, allowing them to switch on and off in different cell types at the right time for cellular differentiation. H3K4me3 also co-localizes with the repressive mark H4K20me3 at a subset of promoters in embryonic stem cells. In contrast to poised H3K4me3/H3K27me3 bivalent promoters, H3K4me3/H4K20me3 promoters are typically active. H4K20me3 co-localizes with similarly repressive H3K9me3, possibly providing functional redundancy[29]. Similarly, the functions of the modifications may be unclear or dependent on the local context. H3K4me1, typically found at promoters and enhancers, has been proposed to have roles in both transcriptional activation[30] and repression[31] depending on its location and the epigenetic identity of the surrounding histones. These examples highlight the importance of context in understanding histone PTM function. Many PTMs remain functionally ambiguous, and combinatorial effects preclude a simple and direct reading of the histone code.

1.1.3 Histone readers, writers and erasers

Histone modifications can be written, read, and erased by histone-modifying enzymes. Histone methyltransferases, or writers, catalyze the transfer of methyl groups from a donor molecule to target lysine or arginine residues. Histone methyltransferases contain a variety of conserved motifs, including SET domains, which recognize specific target sites and carry out the enzymatic reaction. As the name suggests, histone demethylases, or erasers, do the opposite by catalyzing the removal of methyl groups from histone tails. Histone demethylases can have different degrees of specificity of target sites and methyl states.

Histone modifications enact their functions through diverse mechanisms. They can alter chromatin compaction levels by influencing local electrostatic interactions. For instance, histone acetylation neutralizes the positive charge of histones, disrupting 30 nm fiber formation[32]. However, many functions are carried out by reader proteins. These proteins commonly possess specific domains for recognizing particular histone modifications. For example, bromodomains recognize lysine acetylation, chromodomains recognize lysine methylation, and PHD fingers recognize particular methylation states. Some readers can influence chromatin structure directly, like L3MBTL1, which binds to both H4K20me1/2 and H1bK26me1/2 and compacts neighboring nucleosomes that exhibit both of these marks, or the SWI/SNF remodeling complex, that binds acetylated histones, increasing chromatin accessibility[28]. So-called "reader-writer" proteins contain an additional writing domain and can further modify the chromatin[33]. Reader proteins can also act as scaffolding for the recruitment of molecules like DNA repair machinery, transcription factors, or the transcriptional machinery itself. H4K20me2, the most abundant histone modification on the chromatin, recruits 53BP1 to sites of DNA damage, which in turn recruits DNA damage-response proteins like RIF1[34,35]. ORC1 also reads H4K20me2 and carries out functions related to origin licensing and preventing origin refiring[36,37].

Histone readers, writers, and erasers create a dynamic chromatin environment where transcription can be finely tuned depending on which histone modifications are present and when. Over the course of development, a cell matures from pluripotency to a differentiated fate, and the epigenome must mature along with it. Many of the significant events of

epigenome maturation surround zygotic genome activation (ZGA) when transcription begins, and embryos transition from relying on maternally derived mRNA to newly transcribed zygotic RNA. This process differs across species[38] (Figure 1.4).

1.1.4 Epigenome maturation

In mice, the first bout of embryonic transcription occurs in the G2-phase of the first cell cycle, but major ZGA occurs at the transition between the 4- and 8-cell stage[39–41]. Before ZGA, the mouse genome must undergo total remodeling. Sperm nuclei are tightly packaged by positively charged protamines[42]. After fertilization, protamines in the male genome are replaced with maternal histones[43,44]. This repackaging establishes the context for ZGA[38,39]. The male and female genomes form distinct, physically separated pronuclei[45]. After the initial replacement, some maternal histones are replaced with histone variants. For example, canonical H3 is widely and rapidly replaced by H3.3 throughout the genome, helping to maintain chromatin openness[46–49]. Histone modifications can be seen in the early mouse embryo. H3K4me3, for example, is present in 5- to 10-kb domains around the 2-cell stage[50]. These broad domains contrast the characteristically sharp H3K4me3 peaks seen later in development. H3K4me3 is erased at ZGA before reappearing in sharp peaks, and H3K27me3 accumulates after H3K4me3[51]. Heterochromatic H4K20me3 is present in the maternal pronucleus after ZGA, then transiently lost at the 2-cell stage[52]. DNA methylation is also essential to early embryonic chromatin dynamics, and methylation strategies vary across species. Sperm DNA is highly methylated, and in mice, DNA becomes globally demethylated after fertilization[53]. Finally, throughout development, chromatin architecture is gradually established. TADs begin to form at the 2-cell stage but are not well defined until the 8-cell stage, after ZGA[54].

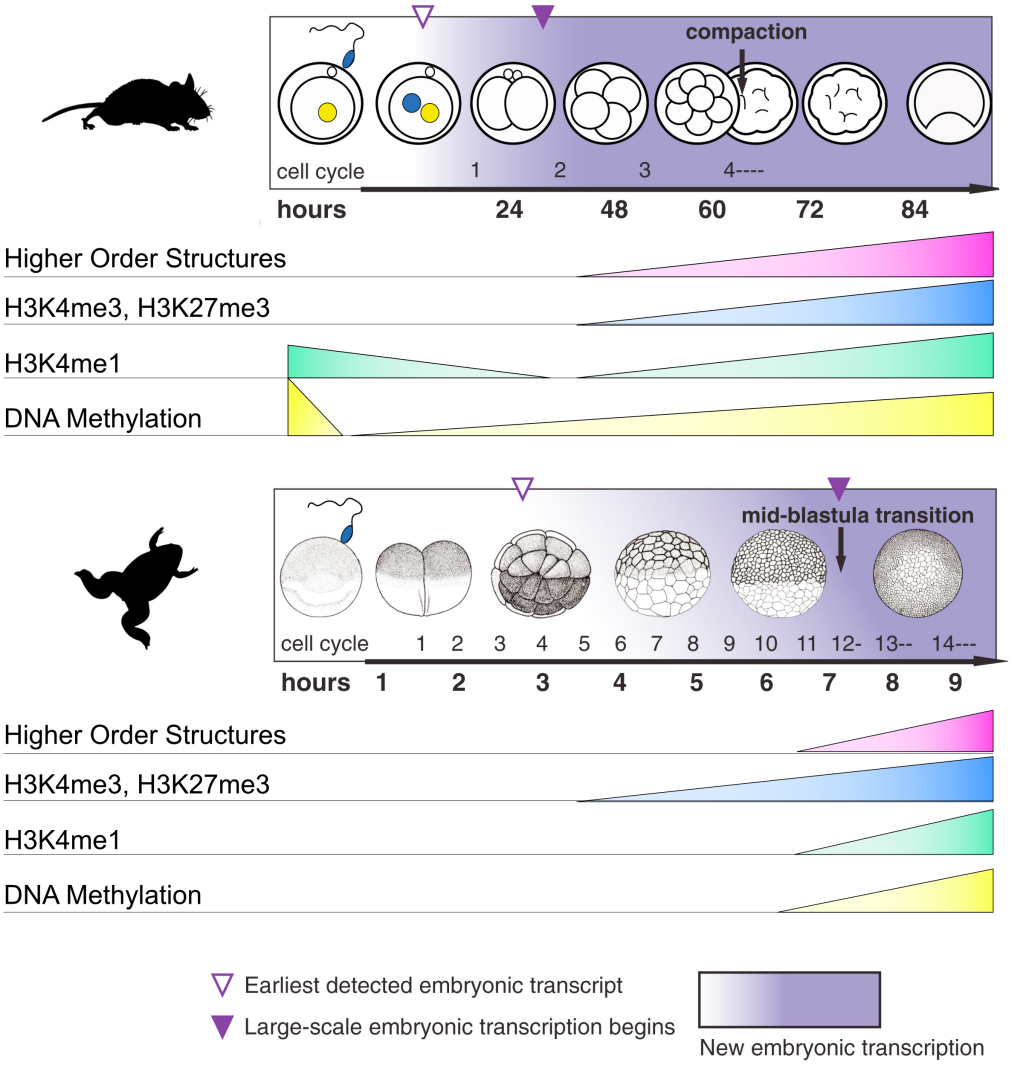

Figure 1.4: Comparison of epigenome maturation between mice and *Xenopus*. Key features of epigenome maturation include changes in DNA methylation, deposition of histone modifications, and establishment of higher-order chromatin structures. Adapted and reprinted with permission from Wiley[38,55].

The *Xenopus* epigenome begins largely devoid of modifications and accumulates epigenetic information over the course of development[55,56]. Similar to mice, *Xenopus* protamines are rapidly replaced with maternal histones, some of which, like maternal linker H1M, remain until the mid-blastula transition (MBT), which coincides with ZGA[38,57,58]. Just prior to ZGA, maternally derived H3K4me3 and H3K27me3 marks are established at promoters[56,59], then

propagated more widely across the genome after the blastula stage. Histone acetylation patterns are established after ZGA. H3K27ac, for instance, appears at the blastula stages and is found throughout the genome by the gastrula stages[60]. As development progresses, chromatin compartments must also be established through the deposition of heterochromatic marks like H3K9me2/3, H3K27me3, and H4K20me3 and the recruitment of repressive and heterochromatic proteins like HP1 and PRC2. Similar to mice, chromatin is largely unstructured in the early stages. Higher-order chromatin structures like TADs must be established and begin to form post-ZGA[61]. In contrast to mice, *Xenopus* DNA remains hypermethylated after fertilization[62,63]. The developing embryo is a highly dynamic system and this extends to the level of the epigenome. The process of epigenome maturation highlights the complexity and importance of establishing chromatin architecture and histone modifications for the progression of development and cellular differentiation (Figure 1.4).

Surrounding the sequencing of the human genome, genetic maps of other model species were also generated. Organisms with less complicated genomes, like *Arabidopsis thaliana* and *Drosophila melanogaster* , were sequenced in preparation for the more arduous task of the human genome. Additional models like mice, Zebrafish, and *Xenopus* were also sequenced after human genome sequencing. As the example of epigenome maturation demonstrates, studying many model organisms in-depth reveals species differences that ultimately shed light on our commonalities. The unique aspects of each model organism allow us to uncover fundamental insights that may not have otherwise been detected.

1.2 Meet *Xenopus*

Xenopus laevis became widely used as a model organism in biology and medicine in the early 1900s. In the 1930s *Xenopus* formed the basis of the first pregnancy test. Researchers found that if they injected a female frog with the urine of a pregnant woman, the frog would lay eggs the next day due to the presence of human chorionic gonadotropin (hCG) in the urine[64]. Two *Xenopus* species are commonly used in biological research: the South African *Xenopus laevis* and the Nigerian *Xenopus tropicalis*. *Xenopus laevis* is found throughout sub-Saharan Africa and lives in freshwater environments, including streams, ponds, and lakes. The frog

reaches metamorphosis in approximately eight weeks, becomes sexually mature within one year, and can live up to 30 years[65].

1.2.1 Xenopus as a model organism

Xenopus has historically been valued as a model organism and remains an excellent research animal. Its life cycle is entirely aquatic, making it easy to keep in a laboratory setting. It lays large clutches of eggs, providing ample experimental material. Egg laying can easily be induced by injection of hCG, the same trick that gave *Xenopus* early fame as a pregnancy test, and eggs can be fertilized with fresh or frozen sperm[66]. At approximately 1 mm in diameter, *Xenopus laevis* eggs and embryos are large, making microinjection, microdissection, and manipulation relatively easy. Their development is entirely extrauterine and can be non-invasively observed from start to finish. As a tetrapod, Xenopus sits between fish and mice on the evolutionary tree, and its physiology and organ function are more similar to mammals than that of fish.

Previously, while Zebrafish and mice were considered genetic models, *Xenopus* was only considered an embryological model. However, the toolbox available to *Xenopus* researchers has grown in recent years. Due to advances like the complete sequencing of the genome, the emergence of CRISPR technology, and the establishment of *Xenopus tropicalis* as an additional model organism – with a diploid genome, in comparison to the allotetraploid genome of *Xenopus laevis*, the African clawed frog is now a beneficial genetic organism that is complimentary to other systems like Zebrafish and mice[67]. A comparison of *Xenopus laevis* and *Xenopus tropicalis* can be found in Table 1.1.

Table 1.1: Comparison of *Xenopus laevis* and *Xenopus tropicalis* as model organisms.

	Xenopus laevis	***Xenopus tropicalis***
Ploidy	Allotetraploid	Diploid
Number of chromosomes (haploid)	18 chromosomes	10 chromosomes
Genome size	$3.1 * 10^9$ base pairs	$1.7 * 10^9$ base pairs
Optimal temperature	16-22°C	25-30°C
Brood size	2000 - 3000 eggs	500 - 2000 eggs
Generation time	1-2 years	4 months

1.2.2 Embryonic development

Thanks to its historical prominence as a model organism, *Xenopus* development is well understood. At fertilization, the sperm initiates an acrosomal reaction, pierces the protective jelly coat around the eggs, and enzymatically digests it, passing it to the egg's plasma membrane[68]. Then, the sperm fuses with the egg, allowing its nucleus to enter the cytoplasm and initiating downstream events. Sperm triggers both cortical rotation and a calcium spike, activating the cell cycle. Next, the egg and sperm nuclei fuse, forming the zygote, and fertilization is complete[69,70]. After fertilization, the embryo undergoes 11-12 rapid cell cleavages that last between 10 and 30 minutes and skip the gap phases[71–73]. Then, the embryo reaches the blastula stage and forms the blastocoel, a fluid-filled cavity within the blastula. At this stage, the nuclear to cytoplasmic ratio initiates a shift at the midblastula transition[74]. The zygotic genome is activated, the maternal store of protein is degraded, and the embryo goes through epigenetic maturation as described in subsection 1.1.4. Cell cycles lengthen to include gap phases and become asynchronous[72,75]. After these extensive genomic changes, the embryo undergoes extensive morphological changes during gastrulation, forming the germ layers. Prospective mesoderm, which is specified at the blastula stage and gives rise to the notochord, involutes over the dorsal lip of the blastopore and elongates the body axis of the embryo through convergent extension. Neuroectoderm, which gives rise to the spinal cord, also undergoes elongation by convergent extension[76].

The three germ layers give rise to distinct tissue types and structures in the embryo and fully developed adult. The endoderm gives rise to most internal organs, including the respiratory

and digestive tract[77]. The mesoderm gives rise to a wide variety of cell types, including the cardiac, musculoskeletal, and blood cells[78]. Finally, the ectoderm gives rise to the nervous system, neural crest, and epidermis[79]. During neurulation, part of the ectoderm differentiates into the neural tube, which forms the central nervous system. After this time, other organs, including the heart and somites, emerge. Then, the embryo becomes elongated, reaches the tail bud stages, and hatches. The early development of *Xenopus* is relatively rapid, where a fertilized embryo can develop to the stage of hatching in 2-3 days. The developing frog will complete metamorphosis in approximately eight weeks. Critical events in *Xenopus* development are summarized in Figure 1.5.

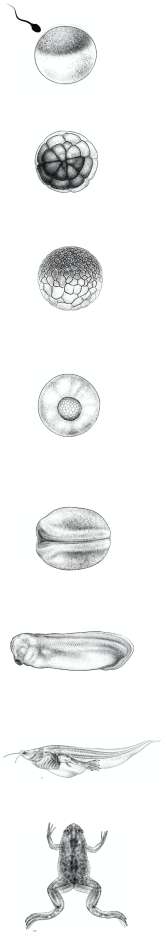

Stage name:	NF number:	Key events:
Zygote	1	Fertilization
Cleavage	2 - 6.5	Rapid, synchronous cells cycles
Blastula	7 - 9	Blastocoel formation MBT and ZGA Cell cycle lengthening
Gastrula	10 - 13	Gastruation Germ layer formation
Neurula	12 - 21	Neurulation Onset of organogenesis
Tailbud	22 - 34	Embryo elongation Hatching
Tadpole	34 - 66	Feeding Metamorphosis
Mature Frog	66+	Sexual Maturity Lifespan up to 30 years

Figure 1.5: Key events in *Xenopus* development. After fertilization, *Xenopus* embryos undergo rapid, synchronized cell divisions that lack gap phases. Early rapid cell cycles persist until the blastula stage, during which the blastocoel, a fluid-filled cavity, is formed, coinciding with the mid-blastula transition (MBT) and zygotic genome activation (ZGA). Cell cycles lengthen to include gap phases and become asynchronous at this stage. The embryo undergoes total remodeling at gastrulation, and the three germ layers are specified. The neurula stage overlaps with the gastrula stage. At this time, neurulation occurs, and some organs, including the heart and somites, are specified. After neurulation, the embryo enters the tailbud stage, increases in length, and hatches from the vitelline membrane. Following this, *Xenopus* tadpoles swim freely and begin to feed. After approximately eight weeks, the tadpoles will complete metamorphosis, and the adult frog can live for up to 30 years. Xenopus illustrations © Natalya Zahn (2022)[80].

1.3 Mucociliary epithelia

Xenopus has also emerged as a valuable model of mucociliary epithelia. Mucociliary epithelia are specialized tissue types that generate and clear mucous and make up a critical part of the vertebrate respiratory tract[81]. In the respiratory system, the mucociliary epithelium in the bronchi functions by trapping inhaled particles in mucous, which are then driven out by fluid flow generated by the coordinated beating of cilia, to mitigate the threat of pathogens[82]. The *Xenopus* embryonic epidermis is composed of a similar mucociliary epithelium. In the developing tadpole, mucous secretion and cilia beating enact several vital functions. Mucous creates a protective barrier, and ciliary beating distributes antimicrobial peptides and oxygenated water along the surface of the embryo[81].

Functional impairment of mucociliary epithelia contributes to several diseases[83,84]. Cystic fibrosis is caused by thickened mucus in the lungs, which leads to impaired ciliary clearance[85]. Patients with primary ciliary dyskinesia, a respiratory disorder, have stiff cilia that cannot beat efficiently[86]. Since the mucociliary epithelium is present on the embryo's surface, it is easy to access and image[81]. Epidermal organoids, known as animal caps, can also be easily generated from blastula-stage embryos, allowing for cleaner genomic analysis of the epidermis without including all of the cell types of a whole embryo. The similarities between the mucociliary epithelium of the mammalian lung and the *Xenopus* embryonic epidermis make *Xenopus* embryos a powerful model system for studying ciliopathies and respiratory illnesses involving the airway epithelium.

1.3.1 Cell composition of mucociliary epithelia

The *Xenopus* embryonic epidermis comprises two layers and five different cell types. The deep layer consists of basal stem cells, some of which are specified into cell types that go on to intercalate into the surface layer[81,87,88] (Figure 1.6). The surface layer consists of goblet cells, which are large, mucous-secreting cells and three intercalating cell types: ionocytes (ICs), small secretory cells (SSCs), and multiciliated cells (MCCs) (Figure 1.8 A). ICs are ion-secreting cells that help to regulate pH and osmolarity[89]. SSCs secrete mucus and serotonin, controlling

the rate of cilia beat. Finally, MCCs , which contain hundreds of motile cilia that beat to generate fluid flow. These five cell types form a characteristic mucociliary epithelium similar to what is found in the human respiratory tract, brain, or reproductive tract.

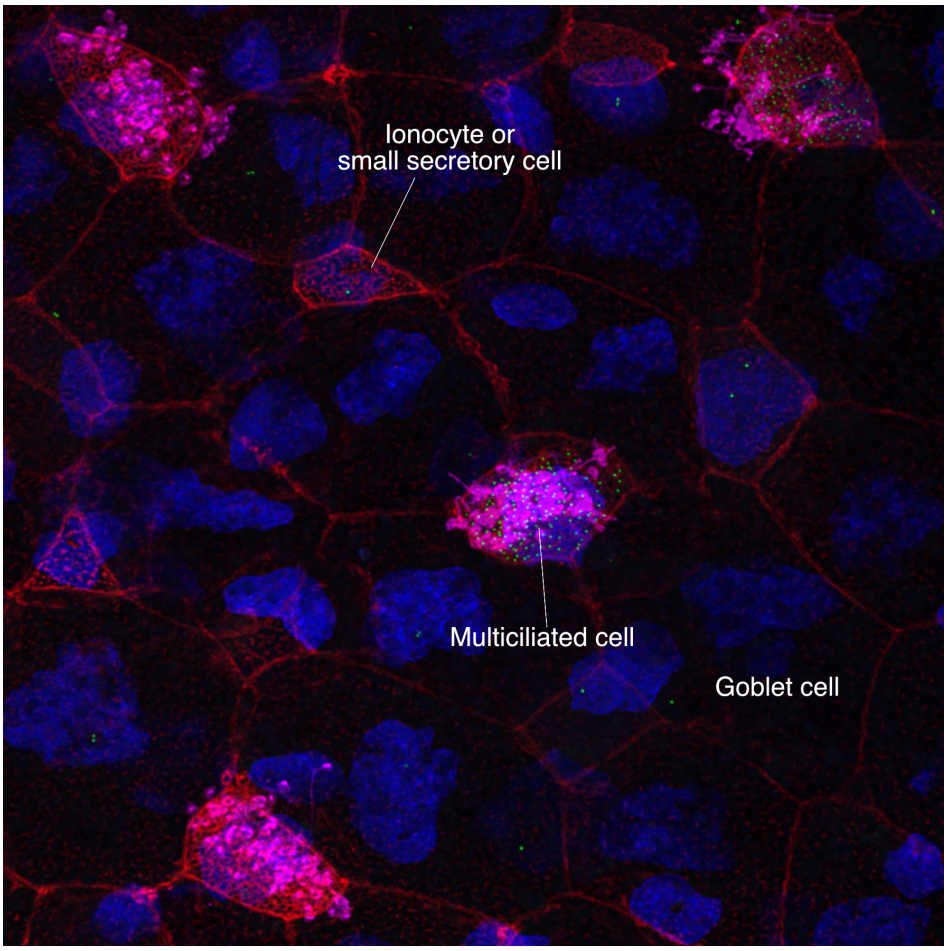

Figure 1.6: Cell types of the mucociliary epithelia. Confocal image showing the surface of an NF 28 *Xenopus laevis* embryo. Mucociliary epithelia are composed of two cell layers. The deep layer consists of basal stem cells that are specified into the intercalating cell types, ionocytes (ICs), multiciliated cells (MCCs), and small secretory cells (SSCs). These cells intercalate at the apices of goblet cells. Here, the actin of cell borders is stained with phalloidin (red), cilia are stained with an antibody against acetylated alpha-tubulin (magenta), basal bodies are marked with hyls1-GFP (green), and nuclei are stained with DAPI (blue).

1.3.2 Multiciliated cell structure

MCCs are a highly specialized and differentiated cell type found on the surface of the developing *Xenopus* embryo. They are motile and beat in a polarized and coordinated manner

to generate directional fluid flow from anterior to posterior. MCCs contain hundreds of ciliary axonemes, consisting of a typical 9+2 microtubule structure: 9 pairs of microtubules, with two additional undoubled microtubules[90–92]. Cilium motility is driven by the sliding of axonemal dynein arms, which bend relative to each other to generate cilia stroke. Each cilium is contained by a specialized membrane composed of phospholipids that adjoins to the surrounding plasma membrane. The ciliary membrane regulates many aspects of cilium biology, including forming and maintaining the axnoneme[93]. The region at the base of the cilium is known as the ciliary transition zone, which acts as a gate, controlling the entry and exit of ciliary proteins from the basal body to the axoneme[94,95]. The transition zone also contains the transition fibers responsible for anchoring the basal bodies to the ciliary membrane[93].

Each ciliary axoneme is nucleated by a specialized type of centriole called a basal body. Basal bodies consist of 9 microtubule triplets, typical of the centrioles found anchoring the primary cilia of cycling cells[91,96]. Basal bodies acquire several accessory structures, including transition fibers and basal feet for stabilization, and the rootlet, which helps anchor the cilia but also determines axoneme polarity and may act as an interface for cellular signaling[97].

Basal body spacing and polarity are supported by an apical lattice of F-actin[98,99]. This lattice is composed of two pools of actin, a meshwork-like actin cap that surrounds the basal bodies, allowing the cilia to emerge from the gaps and a deeper subapical meshwork that connects the basal bodies to the rootlets of neighboring basal bodies[99]. The apical F-actin meshwork coordinates cilia polarity and beating and reinforces basal bodies to withstand the shear stress of cilia movement[100,101]—see Figure 1.7 for an overview of motile cilia structure.

1.3.3 Multiciliogenesis

The formation of multiciliated cells, or multiciliogenesis, is a highly dynamic cellular process (shown in Figure 1.8). Once progenitor cells exit the cell cycle, they face the unique challenge of generating hundreds of centrioles that will mature into basal bodies. This massive centriole amplification stands in stark contrast to other cell types that only replicate their centrioles once per cell cycle[81,91,102]. The amplification of centrioles is achieved through three pathways.

The first is the centriole-dependent pathway, similar to canonical centriole amplification. The original mother centriole is used as a template for centriole amplification (Figure 1.8 B).

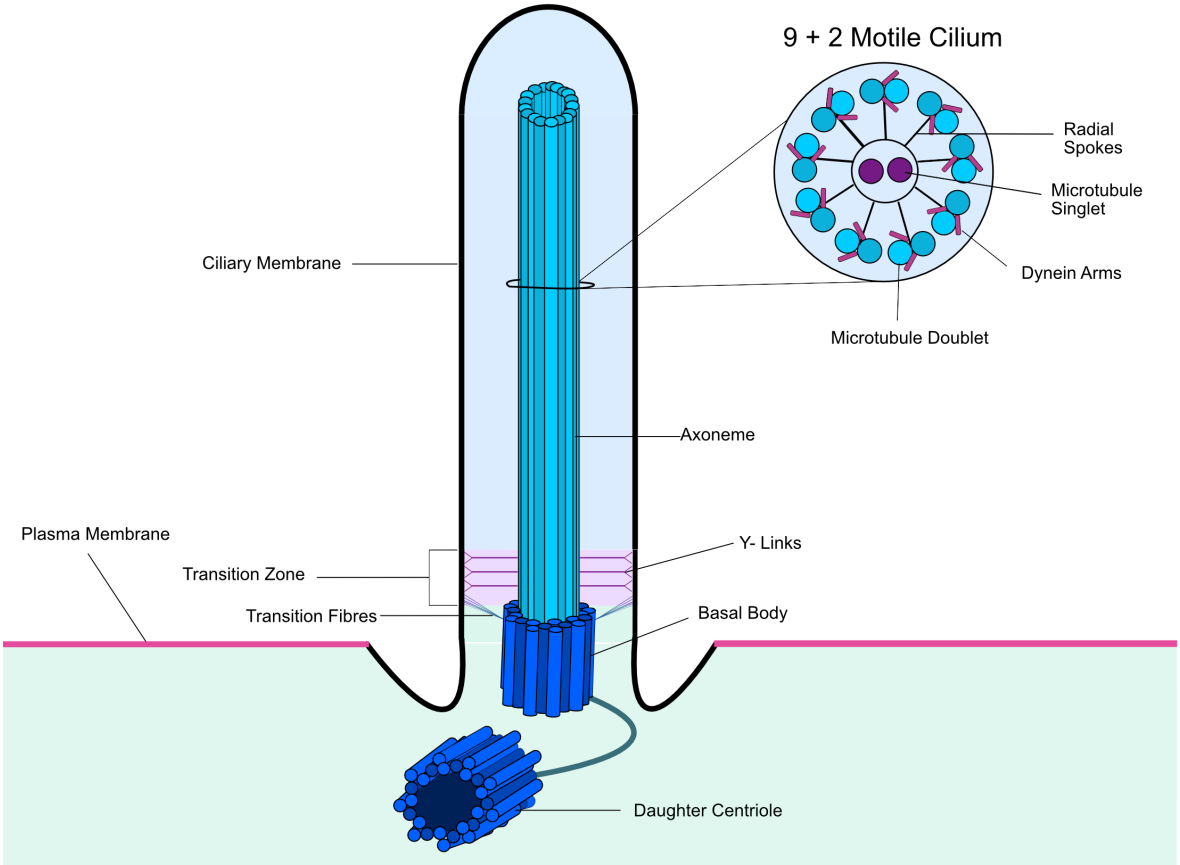

Figure 1.7: Model of a single motile cilia. The ciliary axoneme consists of a typical 9 + 2 microtubule structure: 9 pairs of microtubules around two central microtubule singlets connected by radial spokes[92]. Inner and outer dynein arms on the microtubule doublets generate force for ciliary beating. The ciliary axoneme is encapsulated in a specialized ciliary membrane that fuses to the cell's plasma membrane. The ciliary transition zone controls the entry and exit of proteins to the cilia. The axoneme is nucleated and anchored by a basal body, a specialized type of centriole.

The deuterosome-dependent pathway generates 90% of basal bodies and relies on an electron-dense structure called the deuterosome. The deuterosome, composed of a protein core of DEUP1, localizes to nuclear pore complexes and provides a platform for centriole formation[103,104]. After amplification, the centrioles on the surface of the deuterosome grow and mature into basal bodies and are released from the nuclear pore. The transition between these phases is controlled by attenuated levels of the mitotic oscillator, a series of cell cycle regulators that includes CDK1/2, PLK1, and APC/C[105].

It has recently been shown that centriole amplification can occur in the absence of both the deuterosome and centrioles. While the precise mechanism of *de novo* centriole amplification is unclear, procentrioles emerge from the pericentriolar cloud[106]. This pathway alone can generate typical basal body numbers, and the resulting MCCs look normal in function and morphology[107].

Once basal bodies are mature, they migrate to the apical surface of the cell by vesicular transport[108,109]. On the Xenopus epidermis, basal bodies dock with an even spacing facilitated by the apical actin network[98,99]. When the basal bodies reach the apical surface, the ciliary axoneme is assembled based on the transport of ciliary components along the axoneme microtubules by intraflagellar transport (IFT) machinery, which maintains the axoneme once multiciliogenesis is complete[110].

Underlying these cellular rearrangements, MCC fate is specified via a complicated gene expression program[102]. First, lateral Notch inhibition selects for MCC identity by inducing the expression of multicilin, the master regulator of the multiciliogenesis[111,112]. This can be further regulated in *Xenopus* by microRNAs, miR-34/449s, which repress notch signaling[113]. Multicilin then binds E2F4/5 transcription factors, which induce cell-cycle exit and initiate the differentiation program. Further downstream, transcription factors play essential roles in forming crucial MCC structures. C-MYB, a protein that typically promotes S-phase entry, orchestrates basal body formation. Loss of C-MYB causes a block in basal body amplification[111,112]. Depletion of CCNO, a cyclin-like protein, has been shown to have a similar phenotype to C-MYB depletion and plays a critical role in basal body biogenesis[111,112,114]. Simultaneously, RFX family transcription factors and FOXJ1 control cilia biogenesis by regulating genes associated with ciliary axoneme growth, apical docking, and cilia motility[115–117] (Figure 1.8 C).

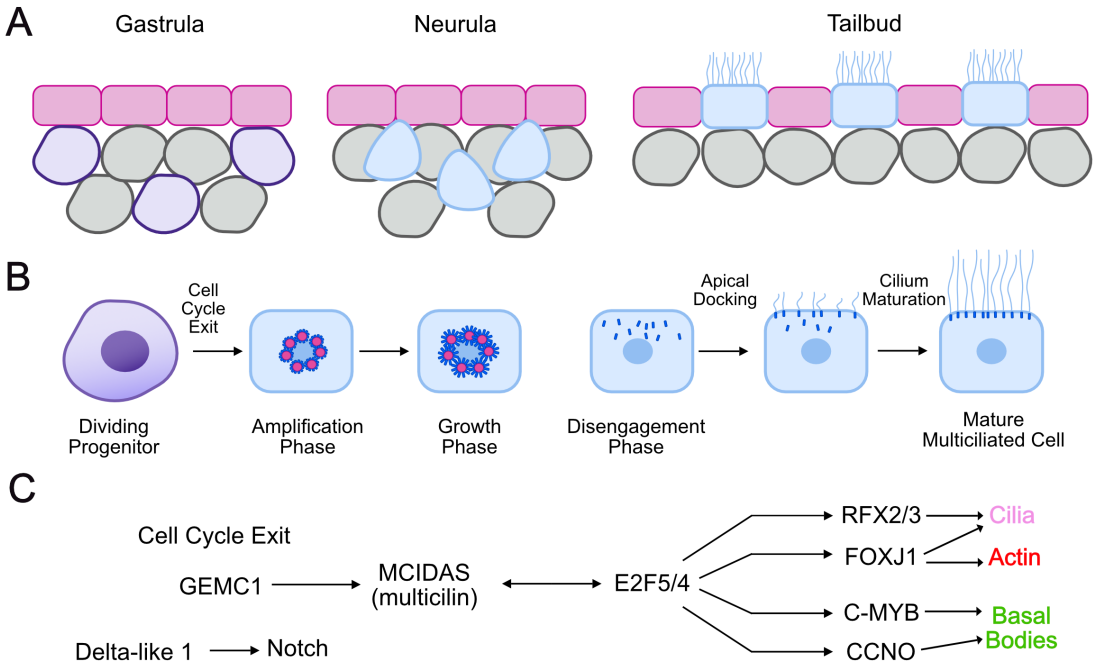

Figure 1.8: The cellular and genetic programs of multiciliogenesis. A) Multiciliated cells (MCCs) are specified from basal stem cells. At the neurula stage, MCC progenitors begin to intercalate into the upper cell layer at the apices of goblet cells. Intercalated MCCs mature and form cilia. B) Specified MCC progenitors exit the cell cycle and become post-mitotic. In the amplification phase, deuterosomes form on the nuclear pore complex and generate up to 300 basal bodies. During the growth phase, these basal bodies increase in size. At the disengagement phase, basal bodies are released from the deuterosomes and migrate to the cell's apical surface. Once they have docked, basal bodies enucleate ciliary axoneme formation, resulting in a mature multiciliated cell. Adapted from[118]. C) The Multiciliogenic gene expression program begins by specifying MCC progenitors by lateral Notch inhibition. Multicilin, the master regulator of multiciliogenesis, initiates a cascade of downstream ciliogenic transcription factors regulated through E2F4/5. This includes RFX2/3, which regulate cilia; FOXJ1, which controls cilia and actin formation; and C-MYB and CCNO, which regulate basal body biogenesis. Adapted with permission[102].

Multiciliated cells are highly specialized and must undergo total cellular remodeling. A network of transcription factors tightly controls this complex differentiation process. However, multiciliogenesis may also be controlled on the epigenetic level. Our lab previously proposed a link between multiciliated cells and H4K20 methylating enzymes[119].

1.4 H4K20 methylation

Methylation of H4K20 was one of the first described histone modifications[120,121] and can be mono- di- or tri-methylated. Each state is present at different abundances on the chromatin and conveys different functions. Approximately 10% of H4 is unmethylated, 10% is monomethylated, 80% is dimethylated, and only about 1% is trimethylated[122–125]. H4K20 is written in a cell-cycle dependent manner, and thus, the levels of each methylation state vary strongly across the cell cycle, as shown in Figure 1.9. During S-phase, newly synthesized, unmethylated histones are incorporated into the chromatin. Starting late in S-phase, SET8 writes the monomethyl mark in an indiscriminate manner[126]. The monomethyl mark persists until the G1 phase, when SET8 is degraded. At this point, H4K20me2, written by suv4-20h1/kmt5b and suv4-20h2/kmt5c, becomes the dominant mark on the chromatin. Following this, H4K20me3 is established at heterochromatin. Suv4-20h1 and 2 may have partially overlapping or redundant functions. In some systems, both enzymes have been shown to write the dimethyl mark, while in others, suv4-20h1 is solely responsible for writing the dimethyl mark, while suv4-20h2 writes the trimethyl mark[52,127]. Once again, in S-phase, DNA replication dilutes methylated histones, and the methylation cycle begins anew. H4K20 methylation levels also change throughout development, with the higher methylated states accumulating as the epigenome matures[122].

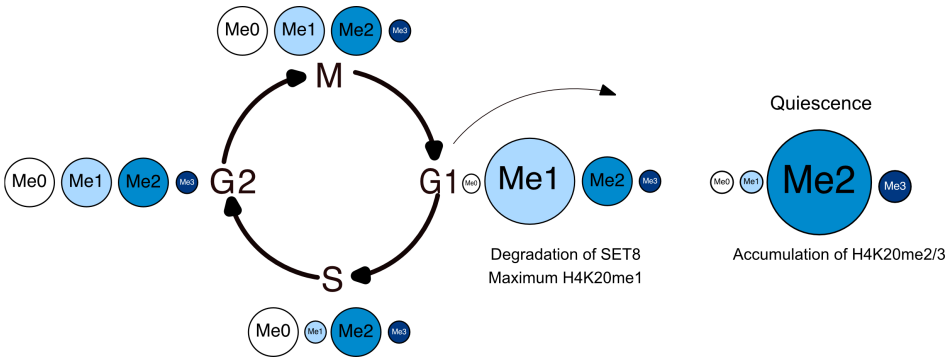

Figure 1.9: H4K20 methylation state abundance varies throughout the cell cycle. Adapted with permission[128].

H4K20 methylation marks are reversible, and there are several H4K20 demethylases (Figure 1.10). The first is PHF8, a JmjC domain-containing protein that erases H4K20me1 into

unmethylated H4K20. PHF8 also has activity towards H3K9me1/2[129,130]. It is targeted to promoters by its PHD finger, which binds to H3K4me3. H4K20me2 can be converted to H4K20me1 by RSBN1, a protein originally identified as a histone demethylase in *C. elegans*, where it is known as dpy-21. Inactivation of dpy-1 reduces X-chromatin compaction and disrupts the formation of TADs during X-inactivation[131]. The final H4K20 demethylase is hHR23b, which has been shown in vitro to have demethylating activity towards all three H4K20 methylation states, but this has not yet been verified *in vivo*. Mass spectrometry data and mathematical modeling from our lab have shown that in the absence of the cell cycle and S-phase dilution, H4K20 demethylases are required to maintain histone methylation at the observed levels[122], thus making histone demethylation an essential process in this system.

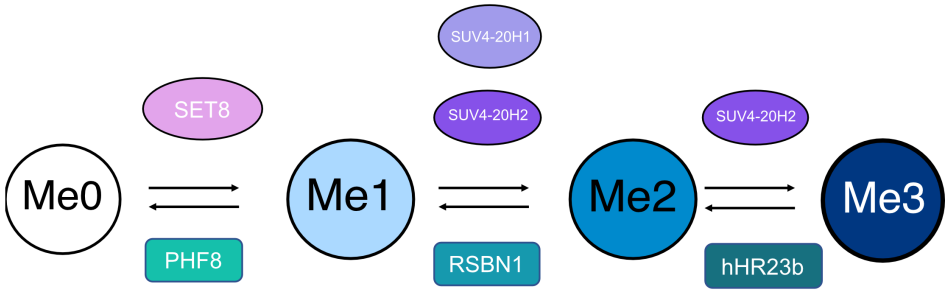

Figure 1.10: Writers and erasers of H4K20 methylation state. H4K20me1 is written by SET8 and erased by PHF8. H4K20me2 can be written by suv4-20h1/2, and suv4-20h2 further writes H4K20me3. RSBN1 erases H4K20me2 into H4K20me1, and hHR23b has demethylating activity towards all three methyl states.

Each H4K20 methyl state also has a distinct functional connotation. The function of unmethylated H4K20 is largely unknown, though it has been proposed to play roles in DNA repair. As previously mentioned, the dimethyl mark is the most abundant histone modification, present in up to 80% of H4 tails. H4K20me2 has several reader molecules which enact different functions[123]. H4K20me2 recruits 53BP1 to DNA damage sites to facilitate non-homologous end joining. ORC1 also reads H4K20me2, and H4K20me2 plays a role in ORC licensing and preventing ORC refiring[36]. H4K20me3 is a hallmark of constitutive heterochromatin. Suv4-20h2 is recruited via HP1 to heterochromatin, where it deposits the trimethyl mark. Its localization to heterochromatin makes it strongly associated with transcriptional repression[127].

The transcriptional effect of H4K20 monomethyl remains ambiguous, as this mark seems

to be both a transcriptional activator and repressor. In favor of transcriptional activation, the mark is found primarily in the gene bodies of active genes[132]. A chromatin immunoprecipitation (ChIP) with sequencing (seq) panel of 20 histone lysine and arginine methylation marks found all monomethylation marks to be linked to gene activation[133]. Correlated ChIP- and ATAC-seq data also suggest that H4K20me1 facilitates the expression of short housekeeping genes[132]. On the other hand, the knockdown of SET8 leads to a two-fold increase in the expression of H4K20me1 target genes[134]. In addition, H4K20me1 plays a role in chromatin compaction, as mammalian cells lacking the mark could not compact appropriately in preparation for mitosis. H4K20me1 is also read by L3MBTL1, which is directly involved in chromatin compaction[135,136137]. H4K20me1 has also been shown, using mintbodies, to coat the inactive X chromosome in mouse cells[138]. Lastly, demethylation by PHF8 has been demonstrated to derepress a subset of E2F1-regulated promoters[129]. The role of H4K20me1 in transcription is up for debate, and it could be that H4K20me1 function is dependent on local context or combinatorial effects with other histone modifications. In this study, we wrestle with the ambiguity of the transcriptional role of H4K20me1 by knocking down suv4-20h1 and suv4-20h2, the enzymes that write H4K20me2 and H4K20me3.

1.4.1 The role of H4K20 writers and erasers in development

The cast of enzymes that write and erase H4K20 methylation states also play critical roles in embryonic development and cellular differentiation[123]. SET8, the enzyme that writes H4K20me1, is required for embryo survival. Mice lacking SET8 die before reaching the 8-cell state, and SET8 knockdown in *Drosophila* leads to death by the late larval stage. SET8 is essential for cell cycle progression, DNA damage repair, and chromosome condensation in mammalian cells[126]. In U2OS cells, loss of SET8 has been shown to decrease overall chromatin compaction as well, and generally, H4K20me1 is considered necessary for maintaining genome stability[139]. Knockdown of PHF8, the H4K20me1 eraser, has deleterious effects on the cell cycle, causing G1/S delay in HeLa cells[129]. Additionally, PHF8 depletion has been shown to cause several developmental defects in zebrafish, including craniofacial abnormalities. The pharyngeal arches fail to develop correctly, and jaw development is impaired[130]. PHF8 is also linked to neurodevelopmental defects by causing apoptosis in the neural tube and brain.

PHF8 knockout mice have compromised learning and memory, and mutations of PHF8 are also linked to Siderius X-linked intellectual disability[140].

Suv4-20h1 and suv4-20h2 are often studied in parallel. These enzymes share sequence homology, some redundant functions, and a common methylation target but also have distinct structural and functional aspects. Both enzymes have a catalytic SET domain, an N-terminal helical domain, and a post-SET domain[141,142]. The catalytic domains of suv4-20h1/2 share 65% sequence similarity, and their homology to other SET domain-containing proteins is low[142]. However, while suv4-20h2 has very few splice isoforms, suv4-20h1 has a variety of alternative transcripts, which may point to differences in regulation, localization, or activity[141].

Suv4-20h1 and suv4-20h2 also play different roles in development. Suv4-20h1 is expressed ubiquitously during development in mice, while the abundance of suv4-20h2 is much lower, which may translate to different functional requirements of the two enzymes. Mice lacking suv4-20h1 are born at sub-mendelian ratios, and the pups are smaller and die soon after birth[127]. Suv4-20h1/2 double knockout mice also die perinatally. On the other hand, Suv4-20h2 null mice do not exhibit embryonic lethality and appear to develop normally[127]. In myeloid leukemia cells, suv4-20h1 depletion is associated with G1 arrest and growth inhibition. Suv4-20h1 is also a known autism spectrum disorder risk factor gene[143].

The consequences of suv4-20h1 and suv4-20h2 loss are also strong in Xenopus. Double knockdown of suv4-20h1/2 with translation-blocking morpholinos leads to several phenotypes of ectodermal origin. These embryos lack both melanocytes and eyes and have craniofacial abnormalities. Additionally, these embryos fail to undergo neuroectodermal differentiation, with the primary neuronal markers disappearing in knockdown embryos, including Notch ligand, Delta-like 1 (dll1)[144]. Outside of neurogenesis, dll1 is involved with the specification of MCCs through lateral inhibition. Increased levels of dll1 lead to repression of the multiciliogenic fate in favor of other intercalating cell types. Most interestingly, while dll1 was abolished from the primary neurons upon suv4-20h1/2 knockdown, it increased in the embryonic epidermis. This was the first indication that suv4-20h1/2 could have a function in multiciliogenesis[119].

1.4.2 Suv4-20h enzymes and multiciliated cells

Indeed, multiciliated cells from *Xenopus* embryos lacking suv4-20h1/2 are severely deformed. They have fewer, shorter cilia that fail to beat in a polarized manner, they have a reduced actin cap, and clumped basal bodies[145,146]. However, the molecular mechanisms behind this phenotype have not been fully elucidated. Additionally, since suv4-20h1/2 have primarily been depleted together, the individual contributions of these enzymes to ciliogenesis remain unknown.

Clearly, there are many open questions surrounding the role of suv4-20h1/2 in multiciliogenesis. Understanding the epigenetic regulation of multiciliated cells by H4K20 methylating enzymes will not only contribute to our knowledge around differentiation of specialized cell types, it could also have implications for respiratory illness involving mucociliary epithelia.

1.5 Objectives

This thesis aims to further explore the connection between H4K20 methylating enzymes and multiciliated cells and address three major objectives:

1. Determine whether an H4K20 demethylase can rescue the ciliogenic defect
2. Define the independent contributions of suv4-20h1 and suv4-20h2 to ciliogenesis
3. Explore the molecular mechanisms underlying the multiciliogenic defect

To reach these aims, we take advantage of the *Xenopus* embryonic system in a variety of ways. We generate mosaic embryos for phenotypic analysis by whole mount immunocytochemistry and confocal microscopy, profile H4K20 methylation state abundancies using mass spectrometry, and generate ectodermal explants, known as animal caps, to perform RNA-seq and ATAC-seq. This powerful combination of phenotypic, proteomic, and genomic analysis will provide valuable insight into the role of H4K20 methylation in development and cellular differentiation.

2

MATERIALS AND METHODS

2.1 Materials

Antibodies

Table 2.1: Antibodies

Name	Dilution	Method	Company
Monoclonal α -mouse acetylated α -tubulin	1:500	ICC Confocal	Sigma-Aldrich (T6793)
goat-α-mouse IgG AP-Conjugate	1:5000	ICC	Abcam (ab97262)
2° goat-α-mouse Alexa Fluor^{TM} 647	1:500	Confocal	Thermo Fisher Scientific (A21236)

Bacteria

Table 2.2: Bacterial strains for cloning

Name	Company
5-alpha Competent *E. coli* (High Efficiency)	New England Biolabs (C2987)
XL1-Blue Competent Cells	Stratagene (200249)

Dyes

Table 2.3: Dyes

Name	Dilution	Method	Company
DAPI	1:50	Confocal	Sigma (D9542)
Alexa Fluor™ 555 Phalloidin	1:20	Confocal	Cell Signalling (8953)
Dextran, Alexa Fluor™ 488	Diluted from 50mg/µl	ICC Embryological methods	Invitrogen (D22910)

Morpholinos

Table 2.4: Morpholinos and Sequences

Name	Sequence
Xl, Xt Suv4-20h1 (H1Mo)	5’ ggattcgcccaaccacttcatgcca 3’
Xl Suv4-20h2 (H2Mo)	5’ ttgccgtcaaccgatttgaacccat 3’
Xt Suv4-20h2 (H2Mo)	5’ccgtcaagcgatttgaacccatagt 3’
Control (CoMo)	5’ cctcttacctcagttacaatttata 3’

All morpholinos are ordered from GeneTools, LLC. Morpholinos were designed to target both homeologs for suv4-20h1/2.

Plasmids

Table 2.5: Plasmids for mRNA Microinjections

Name	Provided by	Restriction Enzyme	Polymerase
pCS2+suv4-20h1 wt (*X. tropicalis*)	R. Rupp / A. Angerilli	NdeI	SP6
pCS2+suv4-20h1 mut2 (*X. tropicalis*)	R. Rupp / J. Tait	NdeI	SP6
pCS2+PHF8 Full-length (Human)	Dharmacon / Horizon Discovery	FspI	SP6
pCS2+Hyls1-GFP (*X. laevis*)	A. Dammermann	NotI	SP6
pCS2+LacZ (nβ-Galactosidase)	R. Rupp	NotI	SP6
pCS2+MCI-hGR (*X. laevis*)	P. Walentek	NotI	SP6
pCS2+PHF8 (1-489) NLS wt (Human)	R. Shiekhattar	SalI	T7
pCS2+PHF8 (1-489) NLS mut (Human)	R. Shiekhattar	SalI	T7

Primers

Table 2.6: Primers for point mutagenesis

Name	Sequence
C.i. xtSuv4-20h1 N264A (Forward)	5’ ggctagggcccgctgcctttattgcccatgattgccggcctaactg 3’
C.i. xtSuv4-20h1 N264A (Reverse)	5’ cagttaggccggcaatcatgggcaataaaggcagcgggccctagcc 3’
C.i. xtSuv4-20h1 Y299A (Forward)	5’ ctggagaagagatttcctgttatgcaggggatggctttttggagaaaa 3’
C.i. xtSuv4-20h1 Y299A (Reverse)	5’ ttttctccaaaaaagccatcccccgtataacaggaaatctcttctccag 3’

Kits

Table 2.7: Kits

Kit Name	Application	Company
D5000 ScreenTape Kit	RNA-seq ATAC-seq	Agilent (5067-5582)
High Sensitivity D5000 ScreenTape Kit	RNA-seq ATAC-seq	Agilent (5067-5592)
High Sensitivity RNA ScreenTape Kit	RNA-seq	Agilent (5067-5579)
Illumina®Tagment DNA Enzyme and Buffer	ATAC-seq	Illumina (20034197)
NucleoBond®Xtra Midi	Cloning ATAC-seq	Machery Nagel (740410.50)
NucleoSpin®Gel and PCR Clean-up	Cloning ATAC-seq	Machery Nagel (740609.250)
NucleoSpin®Plasmid (NoLid)	Cloning ATAC-seq	Machery Nagel (740499.250)
NucleoSpin®RNA Clean-up	*In vitro* transcription RNA-seq	Machery Nagel (740903.10)
NEBNext®Poly(A) mRNA Magnetic Isolation Module	RNA-seq	New England Biolabs (E7490S)
NEBNext®Ultra™ II Directional RNA Library Prep Kit for Illumina	RNA-seq	New England Biolabs (E7760S)
NEBNext®Multiplex Oligos for Illumina®(Index Primers Set 1)	RNA-seq	New England Biolabs (E7335S)
NEBNext®Multiplex Oligos for Illumina®(Index Primers Set 2)	RNA-seq	New England Biolabs (E7500S)
MinElute®PCR Purification Kit	Cloning ATAC-seq	Qiagen (28006)
RNeasy®Mini Kit	*In vitro* transcription RNA-seq	Qiagen (74104)
QuikChange Site-Directed Mutagenesis Kit	Point Mutagenesis	Stratagene (Agilent) (200518)

Reagents

Table 2.8: Reagents used in the thesis

Solution	Application	Company
L-Cysteine hydrochloride monohydrate	Embryo Handling	Sigma-Aldrich (C7880-5006)
Gentamycin solution	Embryo Handling	Sigma Aldrich (G1272-100ML)
Agarose	Embryo Handling Electrophoresis	Bio&Sell (B520.46.50)
Human Chorionic Gonadotropin (Ovogest)	Frog Priming	MSD Animal Health
Nitro blue tetrazolium (NBT)	Immunocytochemistry	Roth (4421.3)
5-Bromo-4-Chloro-3-indoyl-phosphate (BCIP)	Immunocytochemistry	Roth (6468.2)
Heat Inactivated Lamb Serum	Immunocytochemistry	Life Technologies (16070096)
Bovine Serum Albumin (Fraction V)	Immunocytochemistry	GE Healthcare (K45-001)
Levamisole	Immunocytochemistry	Sigma-Aldrich (L9756-5G)
Benzonase	Protein Extraction	Merck (1.01654.0001)
ROTI®Load Lämmli Buffer	Protein Extraction	Roth (K929.1)
dNTPs	PCR	New England Biolabs (N0447S)
NAD	Cloning	New England Biolabs (B9007S)
T5 exonuclease	Cloning	New England Biolabs (M0363S)
Phusion Polymerase	Cloning	New England Biolabs (M0530S)
Taq Ligase	Cloning	New England Biolabs (M0208S)

Standard stock solutions

Table 2.9: Standard stock solutions

Solution	Application	Recipe
10x MMR	Embryo Handling	1 M NaCl 20 mM KCl 10 mM $MgSO_4 \cdot 7H_2O$ 20 mM $CaCl_2 \cdot 2H_2O$ 50 mM HEPES free acid pH adjusted to 7.4-7.8 with NaOH
10x MBS	Embryo Handling	880 mM NaCl 10 mM KCl 24 mM $NaHCO_3$ 8.2 mM $MgSO_4$ 3.3 mM $Ca(NO_3)_2$ 100 mM HEPES Adjust to pH 7.6 with NaOH 10 µg/ml Gentamycin (upon dilution)
10x Steinberg Solution (SS)	Embryo Handling	580 mM NaCl 6.7mM KCL 3.4 mM $CaNO_3$ 3.4 mM $CaNO_3$ 8.3 mM $MgSO_4$ 8.3 mM $MgSO_4$ 50 mM Tris 0.1g Kanamycin
Testes Buffer	Storage of Testes	0.8x MBS 20% Heat Inactivated Chicken Serum (Gibco) 200 U/ml Penicillin 200 U/ml Streptomycin
MEMFA	Immunocytochemistry	0.1M MOPS (3-(N-Morpholino)-propanesulfonic acid) 2 mM EGTA 1 mM $MgSO_4$ 3.7% Formaldehyde
AP Buffer	Immunocytochemistry	100 mM Tris/HCl pH 9.5 100 mM NaCl 50 mM $MgCl_2$ 0.1% Tween 20 0.25 mg/ml Levamisole

Solution	Application	Recipe
PBT	Immunocytochemistry	1x PBS 2mg/ml BSA 0.1% TritonX-100
Antibody Buffer	Immunocytochemistry	1x PBT 10% Heat inactivated lamb serum
20x SSC	Immunocytochemistry	3M NaCl 0.3 M Sodium citrate adjust to pH 7.0 with HCl
Bleaching Solution	Immunocytochemistry	1% Hydrogen Peroxide 5% Formamide 0.5% SCC
10x TBE (pH 8.6)	Gel Electrophoresis	100 mM Tris/HCl 83 mM borate 0.1 mM EDTA
20x TAE	Gel Electrophoresis	2 M Tris 1 M glacial acetic acid 0.05 M EDTA
SOC Medium	Cloning	20 mg/ml Tryptone 5 mg/ml Yeast extract 0.5 mg/ml NaCl 20 mM glucose
Gibson Assembly 5x Buffer	Cloning	450 mM Tris/Cl 25% PEG 8000 50 mM $MgCl_2$ 50 mM DTT 1 mM dNTPs 5 mM NAD
Gibson Assembly 1.33x Final Reagent Mix	Cloning	1.33x 5x Buffer 0.005x T5 exonuclease 0.033 U/µl Phusion Polymerase 5.33 U/µl Taq Ligase
RSB	ATAC-seq	10 mM Tris-HCl, pH 7.5 4 mM $MgCl_2$ 10 mM NaCl
ATAC Lysis Buffer	ATAC-seq	90% RSB 10% Igepal CA-630
Protein Lysis Buffer	Protein Extraction	10 mM Tris-HCl, pH 7.5 100 mM $NaCl_2$ 0.5 % NP40 0.1% SDS

Equipment

Table 2.10: Equipment

Item	Company
TapeStation 4200	Agilent
DS-11 Spectrophotometer	Denovix
Tabletop Centrifuge (Centrifuge 5424)	Eppendorf
Confocal microscope (TCS SP8X)	Leica
Stereomicroscope (M205 FA)	Leica
Qubit 3.0 Fluorometer	Life Technologies
Lightcycler 480	Roche
Flaming/Brown Micropipette Puller P-87	Sutter Instrument
Picoliter Injector PLI-100A	Warner Instruments
Dissecting Microscope (Stemi SV6)	Zeiss

Software

Table 2.11: Commercial software used in this thesis

Software	Company
Affinity Designer	Affinity
TapeStation Controller Software	Agilent
LASX	Leica
LAS v4.13	Leica
Image Studio Lite	LI-COR
Lightcycler 480 Software	Roche
SnapGene	SnapGene
Image J	Wayne Rasband

Indices for RNA-seq libraries

Table 2.12: Indices for RNA-seq: Suv4-20h/2 Double Knockdown

Sample Name	Index Number	Index Sequence
CoMo 1	1	ATCACG
Lacz 1	2	CGATGT
Phf8 1	3	TTAGGC
Rescue 1	4	TGACCA
CoMo 2	5	ACAGTG
Lacz 2	6	GCCAAT
Phf8 2	7	CAGATC
Rescue 2	8	ACTTGA
CoMo 3	9	GATCAG
Lacz 3	10	TAGCTT
Phf8 3	11	GGCTAC
Rescue 3	12	CTTGTA

Table 2.13: Indices for RNA-seq: Suv4-20h1 and Suv4-20h2 Single Knockdown

Sample Name	Index Number	Index Sequence
CoMo 1	4	TGACCA
H1 1	5	ACAGTG
H2 1	6	GCCAAT
CoMo 2	7	CAGATC
H1 2	8	ACTTGA
H2 2	9	GATCAG
CoMo 3	10	TAGCTT
H1 3	11	GGCTAC
H2 3	12	CTTGTA

Table 2.14: Indices for RNA-seq: MCI-hGR

Sample Name	Index Number	Index Sequence
CoMo 1	13	AGTCAA
CoMo + Dex 1	11	GGCTAC
CoMo + MCI 1	15	ATGTCA
H1 + MCI 1	16	CCGTCC
CoMo 2	18	GTCCGC
CoMo + Dex 2	19	GTGAAA
CoMo + MCI 3	20	GTGGCC
H1 + MCI 3	21	GTTTCG
CoMo 3	22	CGTACG
CoMo + Dex 3	23	GAGTGG
CoMo + MCI 3	25	ACTGAT
H1 + MCI 3	27	ATTCCT

All indexing primers come from NEBNext® Multiplex Oligos for Illumina® (Index Primers Sets 1 and 2)

Indices for ATAC-seq

Table 2.15: Indices for ATAC-seq

Sample Name	Index Name	Index Sequence
CoMo 1.1	Ad2.1	TAAGGCGA
CoMo 1.2	Ad2.2	CGTACTAG
H1 1.1	Ad2.4	TCCTGAGC
H1 1.2	Ad2.5	GGACTCCT
H1 1.3	Ad2.6	TAGGCATG
CoMo 2.1	Ad2.13	TGGATCTG
CoMo 2.2	Ad2.15	TGCTGGGT
H1 2.1	Ad2.16	AGGTTGGG
H1 2.2	Ad2.17	GTGTGGTG
H1 2.3	Ad2.18	TGGGTTTC
CoMo 3.3	Ad2.11	AAGAGGCA
H1 3.2	Ad2.19	TGGTCACA
H1 3.3	Ad2.20	TTGACCCT

ATAC-seq indexing primers are from [147].

2.2 Methods

2.2.1 *Xenopus* methods

Xenopus laevis and *Xenopus tropicalis* were acquired from Nasco and Xenopus1. *Xenopus* experiments adhere to the Protocol on the Protection and Welfare of Animals and are approved by the local Animal Care Authorities (license number: 03-22-042).

Xenopus laevis females were pre-primed by injecting 50 IU of human chorionic gonadotropin (hCG) (Ovogest®, MSD animal health) into the dorsal lymph sac one week before use. The

night before use in egg laying, they were stimulated by an injection of 500 IU of hCG. The frogs were kept at 16-18°C overnight and would begin to lay eggs approximately 15 hours after injection. *Xenopus tropicalis* females were primed the night before use with 10 IU of hCG and kept at 23°C overnight. The following day, they were boosted with 150 IU of hCG and began to lay within 5 hours of injection. The females were kept in 1x Marc's Modified Ringer's solution (MMR), laid eggs were collected from the buffer, and additional eggs were collected by gentle squeezing. Females were rested for three months before subsequent use.

Male frogs were anesthetized with 5 g/l tricaine methanesulphonate (Pharmaq). Once the animals were non-responsive (approximately 30 minutes), they were decapitated, and the testes were surgically removed and stored at 4°C in testes buffer for a maximum of 10 days (*Xenopus laevis*) or three days (*Xenopus tropicalis*).

In vitro fertilization and embryo culture

Testes were homogenized with a scalpel (*Xenopus laevis*) or a pestle fitted to an Eppendorf tube (*Xenopus tropicalis*) and diluted with 1x MMR. As much buffer as possible was removed from the Petri dish containing the oocytes and replaced with the testes solution. The oocytes were allowed to rest for 5-10 minutes, and then the Petri dish was flooded with 0.1x MMR. Embryos were incubated at 23°C and monitored after 20 minutes for cortical rotation, a sign of fertilization. The protective jelly coat of the embryos was removed after approximately one hour by incubating in 2% L-cysteine hydrochloride (monohydrate) in 0.1x MMR for 5-10 minutes, followed by three washes with -0.1x MMR. At 23°C, the first cleavage occurs after approximately 1.5 hours.

Microinjections

Embryos were fixed in place using Petri dishes half-filled with 1% agarose in 0.1x MMR and implanted using a silicone mold to create wells approximately the size of a *Xenopus* egg. Needles were made by pulling glass capillaries using a Flaming/Brown Micropipette Puller (Sutter Instrument Co, Model P-97) and pulled needles were calibrated under a stereomicroscope (Stemi SV6, Zeiss). First, the needle tip was broken to allow backward filling. Then, it was

broken further until it could deliver a drop size of approximately 5 nl at an injection pressure of 30 psi for 0.4 seconds. Injection time was further adjusted to deliver smaller volumes as necessary. Injections were performed using a Picoliter Injector (Warner Instrument PLI100A) at a fixed pressure of 30 psi. Depending on the embryo stage at injection time, injection duration ranged from 0.05 - 0.4 seconds. *Xenopus laevis* blastomeres were injected with a volume per cell of 5 nl at the 2-cell stage, 2.5 nl at the 4-cell stage, and 1.25 nl at the 8-cell stage. After microinjections, embryos were incubated in 0.1x MMR with 10 µg/ml gentamicin sulfate, an antibiotic that protects against bacterial infection. Culture temperature varied between 12-23°C depending on the application, and embryos were staged according to the Nieuwkoop Faber table of *Xenopus* development. The embryos were checked periodically, and dead embryos and debris were removed from the Petri dish.

Animal cap dissection, culture and induction

Mid- to late-blastula stage embryos (NF9) were placed in Steinberg's Solution. The blastocoel roof was cut with fine forceps (Fine Science Tools). The animal caps were then transferred to a fresh dish and placed into individual wells to avoid amalgamation and watched to ensure that they rounded up, indicating a successful explantation. They were incubated in Steinberg's Solution between 12-23°C alongside sibling embryos for staging. At the midgastrula stage (NF 11), 10 µM dexamethasone (Sigma) was added to induce nuclear translocation of hormone inducible multicilin (MCI-hGR) protein in injected animal caps.

2.2.2 Nucleic acid methods

Gel electrophoresis

Agarose gel electrophoresis was used to size-separate and visualize fragments of nucleic acids. Typically, gels were prepared from a 1% agarose solution in 1x TBE buffer. Samples were loaded onto the gel with 6x Gel loading dye (NEB) alongside 1 kb or 100 bp DNA ladders. Gels were stained with Midori Green Advance (NIPPON Genetics), run at a voltage between 75-130 V for 1-2 hours, and visualized using the G:BOX Gel Documentation System (Syngene).

Standard polymerase chain reaction (PCR)

For standard PCR, the following components were combined in a PCR tube:

Table 2.16: PCR Reaction Components

Component	Volume
5x Phusion HF GC Buffer	5 µl
Template	1 µl
Forward Primer	100 ng/µl
Reverse Primer	100 ng/µl
Phusion DNA Polymerase	0.5 µl
H_2O	to a final volume of 25 µl

The reactions were then run with the following cycling conditions:

Table 2.17: Cycling Conditions for PCR

Step	Temperature	Time	Cycles
Initial denaturation	94°C	30 seconds	1
Denaturation	94°C	30 seconds	variable
Annealing	55°C	30 seconds	variable
Elongation	72°C	30 seconds	variable
Final elongation	72°C	7 minutes	1
Cooling	4°C	Hold	

Quantitative real-time PCR

Quantitative real-time PCR was performed by adding the following components to a 384-well plate (Roche):

Table 2.18: qPCR Reaction Mix

Component	Volume
Template DNA	1µl
Fast SYBR Green MasterMix	5 µl
3 µM Forward Primer	1 µl
3 µM Reverse Primer	1 µl
Nuclease free H_20	2µl

The following thermal cycling program was run on a LightCycler 480 (Roche):

Table 2.19: Cycling Conditions for qRT PCR

Step	Temperature	Time	Cycles
Initial denaturation	95°C	5 minutes	1
Denaturation	95°C	10 seconds	2-4
Annealing	60°C	20 seconds	2-4
Elongation	72°C	30 seconds	2-4
Melting	95°C	5 seconds	2-4
Melting	65°C	1 minute	1
Cooling	4°C	30 seconds	1

In vitro transcription and mRNA synthesis

A volume of 10 µg of plasmid DNA were linearized in the following reaction conditions:

Table 2.20: *In vitro* Transcription Reaction Components

Component	Volume
10x Digestion Buffer	4 µl
Plasmid DNA	10 µl
Restriction Enzyme	3 µl
H_2O	40 µl

The samples were incubated for at least one hour at 37°C. The reaction products were then visualized on an agarose gel. Next, mRNA was synthesized by combining the following components in a 1.5 ml Eppendorf tube:

Table 2.21: mRNA Synthesis Reaction Components

Component	Volume
5x Transcription Buffer (Promega)	10 µl
10 mM NTP-Mix (Promega)	5 µl
2 µg Linearized Plasmid DNA	8 µl
25 mM G(’5)pppGcap analog (NEB)	5 µl
100 mM DTT (NEB)	5 µl
RNasin (NEB)	0.5 µl
SP6 RNA Polymerase (Promega)	2 µl
DEPC treated H_2O	40µl

The reaction was incubated for two hours at 37°C. An additional 1 µl of RNA polymerase was then added and incubated further for two hours. Subsequently, 1 µl of DNase was added, and the mixture was incubated for 30 minutes. The RNA was then purified using the RNeasy®Mini Kit (Qiagen) according to the manufacturer’s instructions. Briefly, the sample volume was adjusted to 100 µl with RNase-free water, followed by the addition of 350 µl of buffer RLT and 250 µl of 100% ethanol. The samples were then applied to an RNeasy mini column and centrifuged for 15 seconds in a tabletop centrifuge at 28000x g, with the flow-through discarded. This was followed by two washes with 500 µl of buffer RPE. The samples were

centrifuged for 15 seconds, then for 2 minutes, discarding the flow-through. An additional centrifugation for one minute was performed to dry the columns, and the RNA was eluted in 30-50 µl of RNase-free water, followed by a final spin for one minute. RNA concentrations were measured using a nanodrop spectrophotometer, visualized on an agarose gel, and stored at -80°C. The typical concentration of this reaction product ranged from 400 ng/µl to 2 µg/µl, with an injection dose of 50 to 900 pg/blastomere depending on the construct and application.

2.2.3 Cloning methods

Restriction digest

DNA digestion with restriction enzymes is used for two purposes. The first is to prepare plasmids for ligation by fragmenting DNA at known sites. This method also provides a simple way to check the validity of a plasmid during cloning. Since the restriction enzymes cut at known sites, the fragment sizes can be predicted and verified on an agarose gel. Restriction digest was performed by adding the following components to an Eppendorf tube:

Table 2.22: Restriction Digest Reaction Components

Component	Volume
Plasmid DNA	1 µg
Restriction Enzyme 1	1 µg
Restriction Enzyme 2	1 µl
CutSmart Buffer	2 µl
H_2O	Up to 20 µl

The reaction is then incubated for one hour at 37°C, stopped by heat inactivation for 15 minutes at 65°C.

Transformation and plasmid preparation

A volume of 5-7 µl of DNA was added to 100 µl of NEB^{TM} 5-alpha Competent *E. coli* (New England Biolabs), incubated on ice for 30 minutes, heat shocked at 42°C for 2 minutes, then incubated for 3 minutes on ice. The cell mixture was added to 500 µl of SOC medium and incubated for one hour at 37°C with shaking to confer Ampicillin resistance. Cells were plated on LB Agar plates with Ampicillin using a sterilized inoculating loop and incubated until individual colonies were visible and approximately 1 mm in diameter (typically 12-24 hours) at 37°C. Individual bacterial colonies were selected and incubated in 5ml of LB medium with 0.1% Ampicillin for 12-24 hours at 37°C.

Cells were centrifuged for 5 minutes at 3500 g, and the LB medium discarded. Plasmids were purified using Nucleospin®Plasmid Purification kit (Machery Nagel) according to the manufacturer's instructions. Plasmid identity was verified by restriction digest and Sanger sequencing. Midi preps were generated using the Plasmid DNA purification (NucleoBond®Xtra Midi/Maxi, Machery Nagel) kit and verified again by restriction digest.

Gibson Assembly

Gibson Assembly primers were designed to create overlaps between the vector and the fragment, with each primer having an overhang of 15-40 base pairs. The PCR reactions include the following components:

Table 2.23: Insert and Vector PCR Reaction Components

Component	Volume
5x Q5 Reaction Buffer	10 µl
10 mM dNTPs	1 µl
10 µM Forward Primer	2.5 µl
10 µM Reverse Primer	2.5 µl
Template	Genomic DNA: 1 ng - 1 µg Plasmid DNA: 1 pg - 1 ng
Q5 Polymerase	0.5 µl
H_2O	to a final volume of 50 µl

PCR reactions were performed separately for the vector and insert. The reaction is performed in a thermocycler using the following cycling conditions:

Table 2.24: Cycling Conditions for Vector and Insert PCR

Temperature	Time	Cycles
98°C	30 seconds	1
98°C	10 seconds	25-35
50-72°C	30 seconds	25-35
72°C	30 seconds	25-35
72°C	30 seconds/kb template	25-35
72°C	2 minutes	25-35
4°C	Hold	1

Next, the PCR products were visualized on a 1% TAE agarose gel. The insert and vector bands were then cut out of the gel, and the DNA extraction was performed using the NucleoSpin®Gel and PCR Clean-up (Machery Nagel) according to the manufacturer's instructions and eluted in 30 µl. The concentration was then measured on a NanoDrop spectrophotometer (Thermo Fisher Scientific).

The Gibson Assembly reaction was performed with 0.02 to 0.5 pMol total DNA and a vector-to-

insert ratio of 1:3 or 1:5. The final reaction volume was 20 µl, with 10 µl of homemade Gibson Assembly Mastermix. The reaction mix was briefly mixed and centrifuged, then incubated at 50°C for 60 minutes in a thermal cycler. Samples were then transformed into DH5α cells and further processed as described above.

Site-directed mutagenesis

Mutagenesis of the SET domain of the suv4-20h1 plasmid was performed using the Quikchange Site-Directed Mutagenesis Kit (Stratagene) according to the manufacturer's instructions (primers can be found in Table 2.1). Briefly, the following components were added to a PCR tube:

Table 2.25: Site-directed Mutagenesis Reaction Components

Component	Volume
10x Reaction Buffer	5 µl
DNA template	5-50 µl
Forward Primer	100 ng/µl
Reverse Primer	100ng/µl
dNTP mix	1 µl
Q5 Polymerase	0.5 µl
H_2O	to a final volume of 50 µl

Reactions were set up with increasing concentrations of plasmid DNA (5 ng, 10 ng, 20 ng, 50 ng) and overlaid with 30µl of mineral oil. The reactions were cycled in a thermal cycler according to the following conditions:

Table 2.26: Cycling Conditions for Site-directed Mutagenesis

Temperature	Time	Cycles
95°C	30 seconds	1
95°C	30 seconds	12-18
55°C	1 minute	12-18
68°C	1 minute/kb of plasmid length	12-18
4°C	Hold	1

Next, 1 µl of Dpn1 was added to the reaction and incubated for 1 hour to digest the parent DNA. Finally, 1 µl of Dpn1-treated DNA was transformed into XL1-Blue supercompetent cells (Stratagene) and further processed as described above.

2.2.4 RNA-sequencing

Either 10 *Xenopus laevis* animal caps or 30 *Xenopus tropicalis* animal caps per condition, per biological replicate were harvested. Intact animal caps were snap-frozen on liquid nitrogen and stored at -80°C until further use. RNA was extracted using the RNeasy®Mini Kit with On column DNAse digestion. In short, 10 µl β-mercaptoethanol was added to 1 ml Buffer RTL. The animal caps were homogenized in 350 µl of β-mercaptoethanol/Buffer RTL solution by shaking at full speed in a thermomixer at 4°C for five minutes. Next, 350 µl of 70% ethanol was mixed into the lysate. The samples were then transferred to an RNeasy Mini spin column and centrifuged at full speed in a tabletop centrifuge (Eppendorf). Next, on-column DNA digest was performed by incubating with DNase I at room temperature (approximately 24°C) for 15 minutes. Finally, RNA cleanup was performed by centrifuging the column once with Buffer RW1 and twice with Buffer RPE, followed by an additional centrifugation step to dry the column. Samples were then eluted in 30µl of RNase-free water.

Total RNA was diluted and measured on a 4200 Tapestation (Agilent) on the HS RNA ScreenTape (Agilent) using the RNA ScreenTape Ladder (Agilent) and RNA ScreenTape Sample Buffer

(Agilent). This allowed us to check RNA fragment size and provided an RNA integrity number equivalent (RIN^e) to measure RNA integrity, ensuring a score of at least 7. Library preparation was performed using NEBNext®Ultra™ II Directional RNA Library Prep Kit for Illumina®(New England Biolabs). PolyA(+) mRNA was selected for using the NEBNext®Poly(A) Magnetic Isolation Module (New England Biolabs). NEBNext®Multiplex Oligos for Illumina®(Index Primers Set 1 and 2) were used for sample indexing. Size selection was performed using AMPure XP beads (Beckman Coulter). After preparation, the finished libraries were rerun on a 4200 Tapestation (Agilent) using the HSD1000 ScreenTape (Agilent). Sequencing was performed on an Illumina NextSeq1000 (LAFUGA, Gene Center Munich, LMU), with 50bp paired-end reads to a depth of 20 million reads.

RNA-seq data analysis

All data processing methods were applied using default parameters unless specified. Expression quantification was performed using kallisto (version 0.48) using XENLA_10.1 version of the *Xenopus laevis* genome. In R/Bioconductor, expression data were collapsed from isoform to gene level for downstream processing. Differential expression was assessed using DESeq2 (version 1.42.1) using the experimental batch as random factor. RNA-seq data processing and analysis was performed by Tamas Schauer and Tobias Straub.

2.2.5 Assay for transposase-accessible chromatin with sequencing (ATAC-seq)

To profile the change in accessibility in suv4-20h1 knockdown animal caps, we performed ATAC-seq. This protocol was adapted from [148] and [147]. Two animal caps per condition were transferred into low-binding Eppendorf tubes with 1 ml of ice-cold PBS. Samples were centrifuged at 500 g for 5 minutes at 4°C. The PBS was removed, replaced with 50 µl of cold ATAC Lysis Buffer, and homogenized by pipetting with a p200 pipette tip until no remaining tissue was visible. The samples were centrifuged at 500 g for 20 minutes at 4°C. The supernatant was removed, replaced with 50 µl of TAG mix, consisting of:

Table 2.27: TAG mix components

Component	Volume
TDE1 Buffer	25 µl
TDE1 Enzyme	1.88 µl
Nuclease Free H_2O	to a final volume of 50 µl

The reaction components were mixed by pipetting and incubated in a thermal cycler at 37°C with 350 rpm shaking for precisely 30 minutes.

The reaction product was cleaned up using the MinElute®PCR Purification Kit (Qiagen). A volume of 250 µl of buffer PB was added to the sample, mixed by inverting, and applied to a MinElute column. The columns were centrifuged at top speed in a tabletop centrifuge (Eppendorf) for one minute. 750 µl of Buffer PE was added to the sample, which was again centrifuged for one minute at full speed. The columns were transferred to a fresh Eppendorf tube and centrifuged for another minute to dry the membrane. To elute the DNA, 11 µl of kit-provided elution buffer was added to the column, incubated for one minute, and centrifuged at full speed for another minute.

The transposed DNA was then amplified by PCR by combining the following components in a PCR tube:

Table 2.28: ATAC-seq Amplification PCR Reaction Components

Component	Volume
NEBNext 2x PCR Master Mix	25 µl
Transposed DNA	10 µl
25 µM PCR Primer Ad1, Index i5	2.5 µl
25 µM PCR Primer Ad2, Index i7	2.5 µl
Nuclease Free H_2O	10 µl

The reaction was carried out in a Thermal Cycler under the following conditions:

Table 2.29: Cycling Conditions for ATAC-seq PCR Amplification

Temperature	Time	Cycles
72°C	5 minutes	1
98°C	30 seconds	1
98°C	10 seconds	4
63°C	30 seconds	4
72°C	1 minute	4
4°C	Hold	

Once the transposed DNA had been amplified for 4 cycles, a qPCR side reaction was run to determine the optimal number of cycles required without over-amplifying the DNA. The following components were combined and plated onto a 384-well qPCR plate:

Table 2.30: ATAC-seq qPCR Side-reaction Components

Component	Volume
SensiMix SYBR 2x PCR Master Mix	7.5 µl
4 cycle-amplified DNA	5 µl
25 µM PCR Primer Ad1, Index i5	0.25 µl
25 µM PCR Primer Ad2, Index i7	0.25 µl
Nuclease Free H_2O	2 µl

The reaction was run using the LightCycler 480 (Roche) under the following qPCR program:

Table 2.31: Cycling Conditions for ATAC-seq qPCR Side-reaction

Temperature	Time	Cycles
95°C	10 minutes	1
98°C	10 seconds	30
63°C	30 seconds	30
72°C	1 minute	30
4°C	Hold	1

The cycle number corresponding to 1/4 of the cycles required to reach maximal fluorescence in the qPCR side reaction was added to the remaining 45 µl of PCR product. For example, if the side reaction required 20 cycles to reach maximum fluorescence, five more cycles would be performed under the above cycling conditions (Table 2.29). The amplified libraries were then purified using the Qiagen MinElute PCR Cleanup Kit as described above but eluted in 20 µl of kit-provided elution buffer. The concentration was verified with a Qubit 3.0 Fluorometer.

Bead-based size selection was then performed to enrich the libraries for fragments smaller than 600 bp. The following steps were performed at room temperature. Elution buffer was added to bring the sample volume to 50 µl. A volume of 30 µl of AMPure XP magnetic beads were added to the samples for a 0.6x bead-to-sample ratio, mixed well by pipetting and incubated for 10 minutes. The samples were then put in a magnetic stand, and once the beads were bound to the sides of the tube, the supernatant was transferred to a new tube. For a 2x bead-to-sample ratio, 70 µl of AMPure XP beads were added to the sample, mixed well by pipetting and incubated for 10 minutes. Again, the tubes were placed in a magnetic stand, and once the beads were bound to the side of the tube, the supernatant was removed and discarded. Then, the beads were washed twice on the magnetic rack with 200 µl of 80% ethanol. After removing ethanol, the beads were dried for 3-5 minutes, and the libraries were eluted from the beads in 17 µl of kit-provided elution buffer. Samples were mixed off the magnetic rack, rehydrated for two minutes, and then placed back on the magnetic rack. 15 µl of the supernatant containing the libraries was transferred to a fresh, low-binding Eppendorf tube.

The library concentrations were again verified using the Qubit 3.0 Fluorometer. The fragment size distribution of the libraries before and after size selection was visualized using the 4200 Tapestation (Agilent) on the D5000 ScreenTape (Agilent) using the D5000 ScreenTape Ladder (Agilent) and D5000 ScreenTape Sample Buffer (Agilent). The pre-size selection libraries were verified to show a nucleosomal ladder pattern to ensure optimal levels of tagmentation. The size-selected libraries were verified to show fragments primarily in the 150-600 bp range. Libraries were sequenced paired-end at 50 bp to 20 million reads on an Illumina NextSeq 1000 (LAFUGA, Gene Center Munich, LMU).

ATAC-seq data analysis

All data processing methods were applied using default parameters unless specified. After adapter trimming with cutadapt, sequencing reads were aligned to the XENLA_10.1 version of the *Xenopus laevis* genome using bowtie2 (version 2.4). Duplicates were marked and removed with Picard Tools. Peaks were called using macs2. Aligned reads were read in R/bioconductor, converted to coverages (library GenomicRanges), and exported to bigWig files (library rtracklayer). Differential accessibility was assessed using csw/edgeR and TMM normalization as described in the csaw workflow detailed in https://github.com/reskejak/ATAC-seq/blob/master/csaw_workflow.R. ATAC-seq data processing was performed by Tobias Straub.

2.2.6 Protein methods

Protein extraction

A total of 15 *Xenopus laevis* embryos were lysed in 75 µl of cold protein lysis buffer with protease inhibitors (e-complete 25x) and homogenized with a sterile 27 gauge needle until no remaining tissue was visible. The mixture was incubated on ice for 10 minutes. Nucleic acids were digested by adding 1 µl of benzonase and incubating for 20 minutes. The supernatant was then transferred to a new 1.5 ml Eppendorf tube (approximately 50 µl), and 15 µl of Rotiphoresis loading dye (Lämmli buffer) was added. The mixture was then snap-frozen in

liquid nitrogen and immediately thawed at 37°C. This freeze/thaw cycle was repeated 3-5 times to shear the remaining DNA. The protein extract was stored at -80°C.

Whole mount immunocytochemistry with Alkaline Phosphatase staining

Embryos were fixed in MEMFA (3.7% formaldehyde in 1x MEM) for 1.5-2 hours at room temperature. They were then rinsed in PBS, moved to methanol, and stored at -20°C for at least one night. Embryos were then sequentially rehydrated in 80% and 50% methanol in PBS, then 100% PBS, followed by one 5-minute wash in PBS, and one 15-minute wash in PBT (1x PBS, 2mg/ml BSA, and 0.1% triton x-100). Next, non-specific protein binding sites were blocked using 0.5 ml of antibody buffer (PBT, 10% heat-inactivated lamb serum) for one hour at room temperature. Afterward, the embryos were incubated overnight in primary antibody diluted to 0.5 ml in antibody buffer (1:500 Monoclonal Anti-Acetylated Tubulin antibody Sigma-Aldrich, T6793). After primary antibody incubation, the embryos were washed 5-6 times for 30-60 minutes per washing step in PBT. Then, the embryos were incubated overnight in AP-conjugated secondary antibody (Shp x Mouse Fab IGg Alk Phos, Chemicon 1:1000).

The next day, embryos were washed 5-6 times for one hour each wash in PBT, then for 20 minutes in alkaline phosphatase (AP) buffer (100 mM Tris pH 9.5, 50 mM $MgCl_2$, 100 mM NaCl, 0.1% Tween20, 2.55 mg/ml Levamisole). Next, the alkaline phosphatase colour reaction was performed. Embryos were moved to staining solution (4.5 µl of 75 mg/ml NBT + 3.5 µl of 5% BCIP per ml AP buffer) and monitored until AP staining was visible, at which point the reaction was stopped by washing in PBS. The embryos were then incubated overnight in methanol to reduce background staining and fixed for a second time in MEMFA. They were then dehydrated in 70% ethanol in PBS and pigment was removed by incubating for 2-3 hours in bleaching solution (0.5% SSC, 5% formamide, 1% H_2O_2).

Whole mount immunocytochemistry for confocal microscopy

Tailbud stage (NF28) *Xenopus laevis* embryos were fixed at room temperature for one hour in MEMFA, then briefly washed with PBS. The alcohol wash step was omitted to preserve the fluorescence from the injected hyls1-GFP (Table 2.5). The embryos then were washed in PBS

with 2% Triton for 20 minutes to permeabilize the cell membranes, followed by a 15 minute wash with PBT. Next, the embryos were incubated for 1 hour in antibody buffer, and then with the primary antibody (1:200 Monoclonal Anti-Acetylated Tubulin antibody Sigma-Aldrich, T6793) for 2 hours at room temperature. Following this, the embryos were washed overnight at 4°C or for 2 hours at room temperature. The samples were then incubated with a fluorescent secondary antibody (goat anti-mouse 1:1000, Chemicon) for two hours at room temperature. From this step on, the embryos were kept in the dark. They were washed for 2 hours at room temperature in PBS, stained with DAPI (1:50 in PBS, Sigma) for 15 minutes, and then further washed five times briefly with PBS. Phalloidin staining was then performed by incubating the embryos in 5% Alexa Fluor 555 Phalloidin (Cell Signalling) in PBS for 1.5 hours to stain the cell borders, followed by a rinse with PBS.

The embryos were then mounted between two glass coverslips (High Precision Cover Glasses 24x60 mm, Roth) separated by 0.35 mm thick double-sided adhesive tape. Adhesive tape was stuck to one glass coverslip and wells were cut into the tape using a scalpel, then filled with a modified Dabco mounting solution (85.43% Glycerol, 10% 10x PBS + 2% Dabco, 4.57% H_2O). Embryos were rinsed in mounting solution and then placed carefully so that they lay flat within the wells. A second glass cover was placed on top. Samples were visualized on an inverted confocal microscope (Leica TCS SP8X).

2.2.7 Mass spectrometry sample preparation and analysis

Nuclear histone extraction, sample preparation, and mass spectrometry analysis were performed by Daniil Pokrovsky as in [122]. In short, 50 *Xenopus laevis* embryos were collected and washed with 110 mM KCL, 40 mM Tris/HCl (pH 7.4), 5 mM $MgCl_2$, 0.1 mM spermine, 0.1 mM EDTA, 2 mM DTT, 0.4 mM PMSF, and 10 mM Na-butyrate. The embryos were homogenized in a 5 ml glass-glass douncer (Braun, Melsungen) and centrifuged at 2600 g for 10 minutes. The nuclear pellets were resuspended in 1 ml of 0.1 M acetic acid with 1 mM DTT and then vacuum-dried.

The pellet was then dissolved in Laemmli buffer to a dilution of 1.37e6 nuclei/µl. Histone bands were visualized by loading 15 µl onto an 18% - 16% gradient SDS-PAGE gel (SERVA) and

stained with Coomassie Blue. Bands were excised and propionylated to block the cleavage of endogenously unmodified and monomethylated lysine residues. The gel samples were mixed with trypsin and Arginine10-labeled forms of the histone PTMs (500 fmols/peptide, JPT Peptide Technologies, Berlin, Germany), desalted, and resuspended in 15 µl of 0.1% formic acid.

The relative abundance of histone PTMs was analyzed using LC-MS. To control for differences in ionization between samples and peptides, isotopically labeled R10 peptides were mixed into the samples at equimolar ratios. The abundance of histone PTMs was measured using a parallel reaction monitoring (PRM) method (as in [149]). Analysis of the peptide mixtures was performed using an Ultimate 3000 nano chromatography system (Thermo Fisher Scientific) coupled to a QExactive HF mass spectrometer (Thermo Fisher Scientific). A volume of 5 µl of sample was injected into a C-18 separating column through 0.1% formic acid at a flow rate of 300 nl/min and separated over 90 minutes by a gradient of 3% to 40% ACN. Fragment ions of N-terminal peptides were identified and quantified using a QExactive HF operating in a scheduled PRM mode. This allows the mass spectrometer to switch automatically between one survey scan and 9 MS/MS acquisitions of m/z values. Acquisition of full scan MS spectra had a resolution of 60 000 at m/z 400, and PRM spectra were acquired with a resolution of 30 000 to target value of 2×10^5, maximum IT 60 ms, and isolation window 0.7 m/z and fragmented at 27% or 30% normalized collision energy. The MS conditions included a spray voltage of 1.5 kC, no sheath and auxiliary gas flow, and a heated capillary temperature of 250°C. Data analysis was performed using Skyline version 3.7.

2.2.8 Statistical analysis

ICC results from knockdown experiments were analyzed using a two-tailed t-test. Results from rescue experiments were analyzed using one-way ANOVA with post-hoc Tukey test. For mass spectrometry, in the case of multiple testing, the Benjamini–Hochberg FDR procedure was performed.

2.2.9 Data availability

RNA high-throughput sequencing data has been deposited in the NCBI GEO under the accession numbers GSE161251 and GSE274392. ATAC-seq data as been deposited in the NCBI GEO under the accession number GSE274391.

3

RESULTS

3.1 Suv4-20h1/2 KD embryos lack cilia

We leverage the *Xenopus* fate map to generate mosaic embryos that are partially wild-type (wt) and partially affected[150]. In general, we use two different injection schemes for microscopy experiments. For wholemount immunocytochemistry, we inject one of two blastomeres at the two-cell stage with our constructs of interest and Alexa Fluor 488, which acts as a lineage tracer. Tight junctions between cells in the early *Xenopus* embryo keep the cells' contents separate, so injected material is contained within the injected cell and its progeny. This results in an embryo that is wt on one side and affected on the other (Figure 3.1 A). For confocal experiments analyzing multiciliated cells (MCCs), we inject one of two ventroanimal blastomeres with our constructs of interest and hyls1-GFP, a centriolar protein, to visualize basal bodies and determine which MCCs are wt and which have been affected by injection. This injection scheme results in a mosaic effect in which affected and wt embryos are visible within the same field of view and can act as an in-embryo control (Figure 3.1 B).

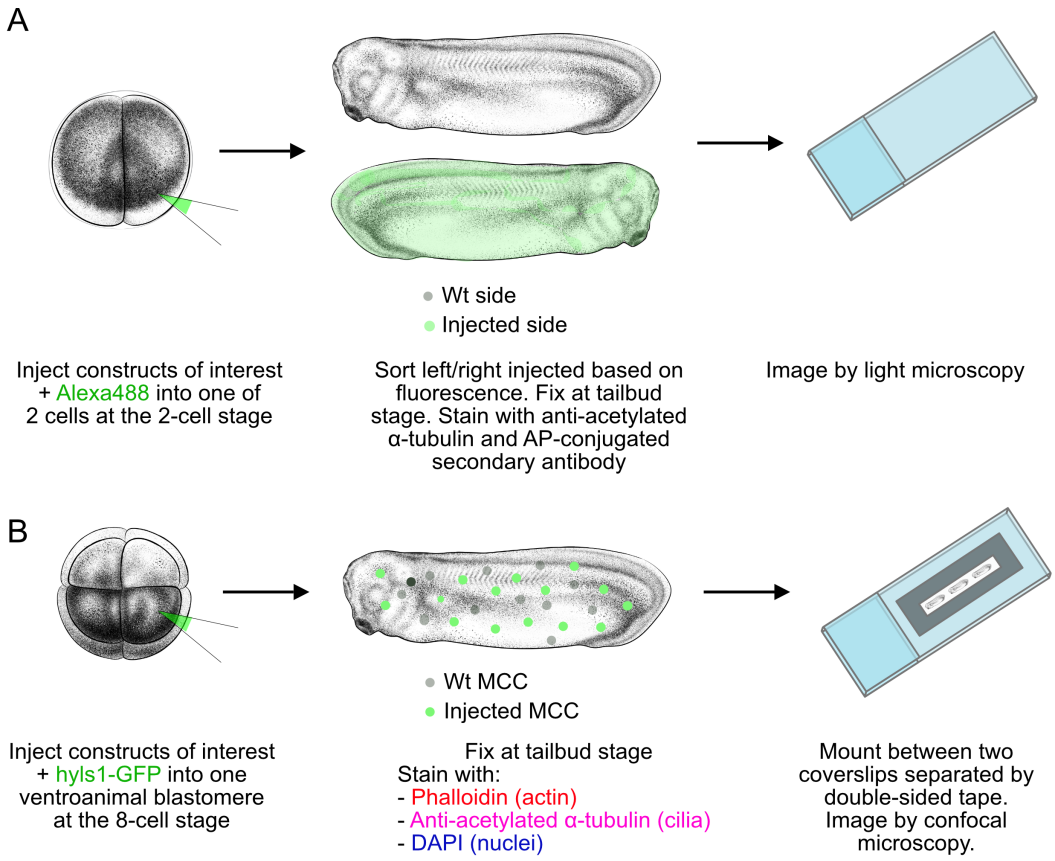

Figure 3.1: Targeted microinjection schemes to generate mosaic embryos. We take advantage of the *Xenopus* fate map to visualize injected multiciliated cells (MCCs) in the same embryo and field of view as wild-type MCCs. A) For wholemount immunocytochemistry with alkaline phosphatase (AP) staining, we inject one cell of a two-cell stage embryo with our constructs of interest and Alexa Fluor 488 (a lineage tracer). This gives rise to an embryo that is wild-type on one side and affected on the other side. We fix at the tailbud stage (NF28), and stain cilia with an antibody against acetylated α-tubulin and an AP-conjugated secondary antibody. B) To perform fluorescent confocal microscopy, we inject constructs of interest alongside hyls1-GFP mRNA into the ventroanimal blastomere of an 8-cell stage embryo. Hyls1 is a centriolar protein that allows us to visualize basal bodies while also acting as a lineage tracer to determine which cells are injected and which are wild-type. Once the embryos reach tailbud stage and the MCCs have emerged into the surface layer of the epidermis, we fix the embryos and perform fluorescent immunocytochemistry, staining filamentous actin with phalloidin, cilia with an antibody against acetylated α-tubulin, and DNA with DAPI. We mount the embryos between two coverslips separated with double-sided tape, and image using confocal microscopy. This strategy is used for all of the confocal microscopy in the thesis. Xenopus illustrations © Natalya Zahn (2022)[80].

Our lab previously used translation-blocking suv4-20h1/2 morpholinos (H1H2Mos). This results in severe MCC defects and a concerted misregulation of ciliogenic genes. This phenotype was characterized on the cellular level by microscopy, which showed that the apical actin

network, as well as cilia number and length are all severely impaired in suv4-20h1/2 knockdown MCCs. We were consistently able to replicate these results across multiple experiments by whole-mount immunocytochemistry and confocal microscopy and found that the cilia and the apical actin meshwork are impaired. Thus, the link between H4K20 methylating enzymes and MCCs is confirmed in this thesis. The cilia and actin phenotypes are visualized in Figure 3.2 A.

Additionally, we performed Gene Ontology (GO) enrichment analysis for cellular components on previously generated RNA-seq data from our lab on H1H2Mo injected animal caps[151]. GO enrichment analysis assesses a gene set, in this case, all up- or downregulated genes, and unveils which annotated GO terms are over-represented within this gene set. In the upregulated gene set, we find gene categories related to chromatin organization and remodeling, gene expression, metabolic processes, and cell cycle (Figure 3.2 B). However, in the downregulated gene set, we see many GO terms related to ciliogenesis and cytoskeleton, including cilium movement, axoneme assembly, and plasma membrane bounded cell projection. This confirms analysis found in Angerilli, Tait, *et al.*[151] and demonstrates that ciliogenic genes in H1H2Mo injected animal caps are strongly downregulated, giving a transcriptional basis for the ciliogenic phenotype (Figure 3.2 C).

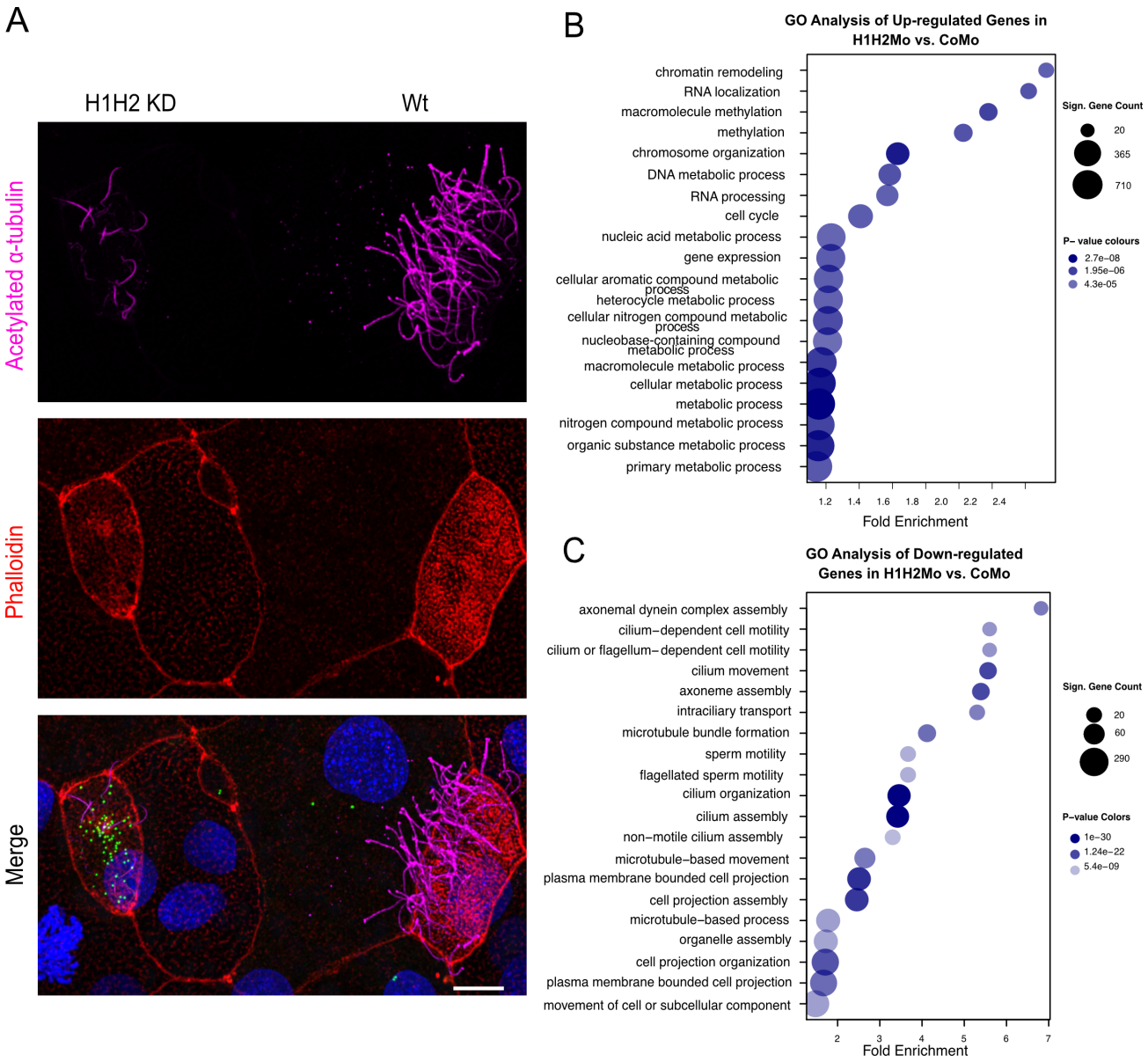

Figure 3.2: Suv4-20h1/2 knockdown leads to severe ciliary defects. A) Representative confocal images detailing the loss of cilia and actin cap upon suv4-20h1/2 morpholino injection (H1H2Mo). The basal bodies are green (hyls1-GFP), the cilia are magenta (acetylated α -tubulin), the apical actin meshwork is red (phalloidin), and the nuclei are blue (DAPI). The embryos are injected in one of two ventroanimal blastomeres, resulting in a mosaic effect allowing wt and knockdown cells to be present in the same field of view, where knockdown cells can be visualized by green basal bodies (wt = wild-type, * = knockdown). Scale bar = 10 µm. B,C) GO analysis for biological processes. The top 20 B) upregulated and C) downregulated GO terms are shown. Adapted and reprinted with permission from Life Science Alliance (Angerilli, Tait, *et al.*[151]).

3.2 Suv4-20h1/2 knockdown shifts H4K20 abundance from H4K20me2 to H4K20me1

We also aimed to understand how knocking down H4K20 methylating enzymes influences the abundance of different H4K20 methylation states. To quantify these changes, we conducted mass spectrometry on neurula-stage *Xenopus laevis* embryos injected with suv4-20h1 morpholino (H1Mo), suv4-20h2 morpholino (H2Mo), or H1H2Mo (Figure 3.3 A). The samples were propionylated, trypsin-digested, and the resulting tryptic peptides were quantified as described in [122]. Our analysis revealed minimal impact on unmethylated H4K20, with only the H1Mo injected embryos showing a small but significant decrease. The double knockdown had the most pronounced effect on H4K20me1, increasing its abundance from approximately 20% in the wt and control morpholino (CoMo) conditions to over 60% in the double knockdown. H1Mo and H2Mo individually raised H4K20me1 levels to about 45%. Conversely, H4K20me2 levels significantly decreased, with H1H2Mo reducing K20me2 from 60% to around 25%, and each single knockdown lowering it to approximately 45%. H4K20me3, the least abundant methylation state, decreased significantly from about 0.3% in the wt to 0.03% in the double knockdown. While H1Mo had a minor, non-significant effect on K20me3, H2Mo decreased H4K20me3 to a level similar to that observed with H1H2Mo (Figure 3.3 A'). H1H2Mo exerted the strongest effects on H4K20me1 and H4K20me2, whereas the single knockdowns had intermediate, potentially additive effects. Overall, our findings indicate a shift from predominantly dimethylated chromatin to primarily monomethylated chromatin. Both enzymes contribute similarly to the dimethyl mark, but only suv4-20h2 appears responsible for the trimethyl mark.

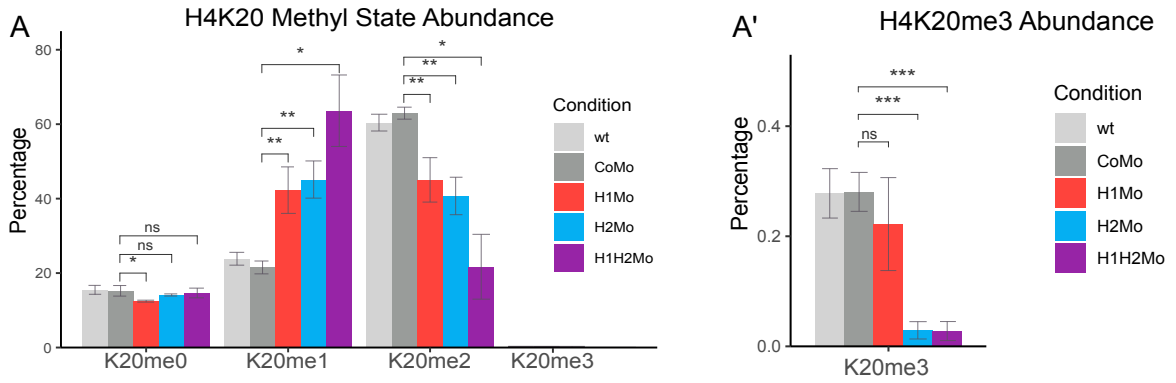

Figure 3.3: Analysis of H4K20 methyl landscape by mass spectrometry. Relative abundance of (A) unmethylated H4K20, H4K20me1, H4K20me2, and (A') H4K20me3 in wt, control morpholino (CoMo), suv4-20h1 single knockdown (H1Mo), suv4-20h2 single knockdown (H2Mo) or double knockdown (H1H2Mo) in neurula stage *Xenopus laevis* embryos. Raw data was spike-tide normalized and quantified as in Pokrovsky *et al.* [122]. Significance is indicated by asterisks; * = padj < 0.05, ** = padj < 0.01, *** = padj < 0.001 according to Benjamini-Hochberg procedure. Adapted and reprinted with permission from Life Science Alliance (Angerilli, Tait, *et al.*[151]).

To ensure that the effect of suv4-20h1/2 knockdown was specific to H4K20 methylation, we profiled several other histone modification sites. This includes methylation or acetylation of H3K9, K4, K14, K27, K36, and K37 (Figure 3.4). In this protocol, unmodified lysine residues become propionylated, and are marked "p". To visualize changes in abundance, we generated a heatmap with colour corresponding to the ratio between control morpholino and each condition, and the relative abundance represented as a percentage (Figure 3.4 A). None of the other marks were significantly affected except for H3K27ac, a mark of active enhancers and promoters, which decreased from 0.52% in the control condition to 0.28% in H1Mo, and 0.32% in H1H2Mo injected embryos. Suv4-20h1 has not been previously shown to affect H3K27ac. It is unclear whether this is of functional significance. This small loss of H3K27ac could lead to reduced enhancer chromatin, and correlate with reduced transcription. However, H3K27ac is a lowly abundant mark, and this could represent a non-specific effect at sites where H3K27ac colocalizes with H4K20me2.

In summary, both suv4-20h1 and suv4-20h2 contribute similarly to the writing of H4K20me2, with the double knockdown showing the most pronounced impact on H4K20me1 and H4K20me2 levels. In contrast, suv4-20h1 does not affect H4K20me3, while the suv4-20h2

knockdown alone has a similar impact on H4K20me3 as the double knockdown.

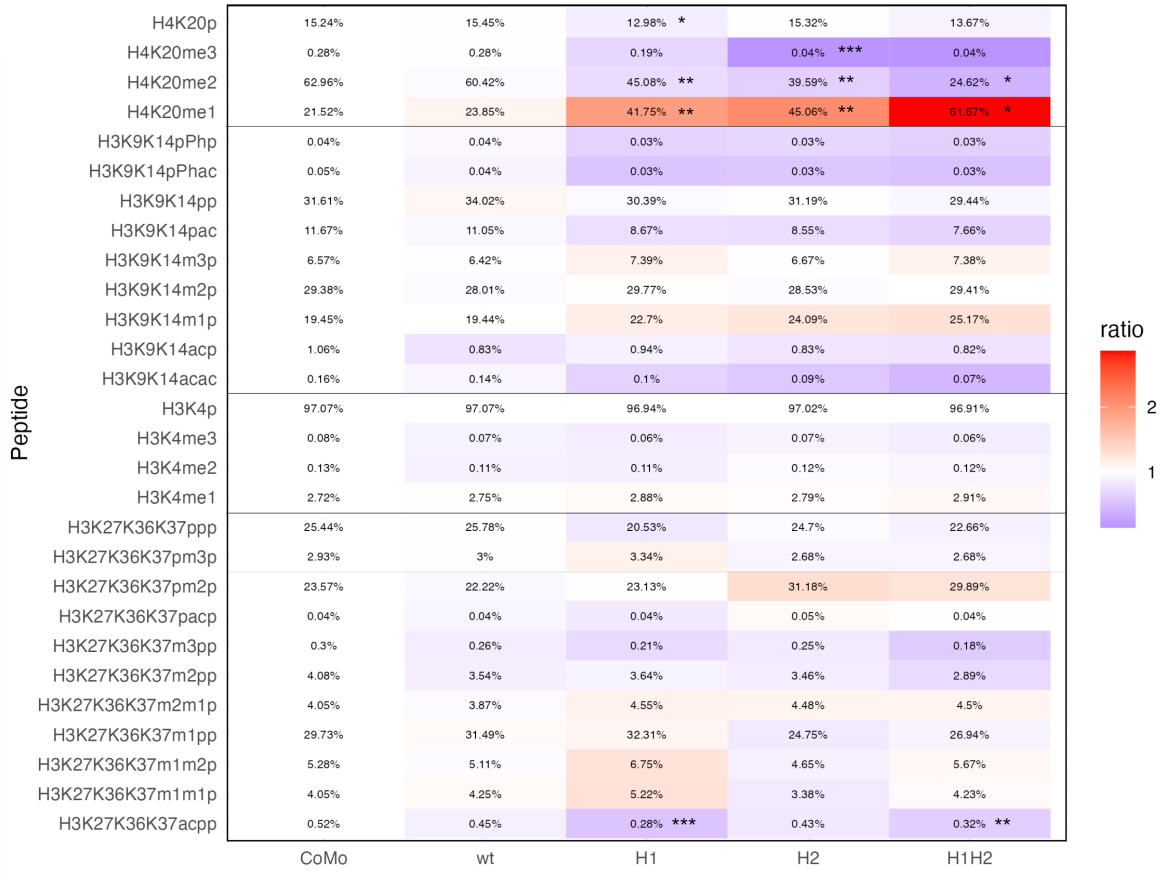

Figure 3.4: Effect of suv4-20h1/2 KD on histone modification abundancies. Mass spectrometry results showing the relative change in abundance of histone modifications in response to injection of morpholinos against suv4-20h1 (H1), suv4-20h2 (H2), both (H1H2) or a control morpholino (CoMo) in neurula stage *Xenopus laevis* embryos. Heatmap detailing the relative abundances (numbers in each cell), and ratio between each condition and CoMo (colour). Percentages are calculated within each tryptic peptide. Raw data was spike-tide normalized and quantified as in Pokrovsky *et al.* [122]. Significance is indicated by asterisks; * = padj < 0.05, ** = padj < 0.01, *** = padj < 0.001 according to Benjamini-Hochberg procedure. 'p' stands for propionylated and indicates naturally unmodified lysine residues.

3.3 Rescue of MCCs with an H4K20me1 demethylase

3.3.1 PHF8 partially rescues multiciliogenic defect

We hypothesized that the increase in H4K20me1 generated by suv4-20h1/2 depletion was responsible for the ciliogenic defect and decided to test this orthogonally by rescuing the phenotype with PHF8, an H4K20me1 demethylase. PHF8 is a JmjC domain-containing protein that is mainly targeted to promoters by its PHD domain which binds to histone H3K4me2/me3. Its substrates include H3K9me1/2, H3K27me2, and H4K20me1. Knockdown of PHF8 has been shown to negatively correlate with gene expression, and lead to increased H4K20me1 at coding regions[129,130]. Additionally, PHF8 knockdown has been shown to impact cytoskeletal organization and neurite outgrowth[152]. PHF8 is of interest to us based on its function as an H4K20me1 demethylase, and its involvement in cellular processes related to our observations (namely regulation of cytoskeleton and cellular projections). We decided to test whether PHF8 could rescue the ciliogenic phenotype, potentially by removing H4K20me1 marks near transcription start sites that arise from the knockdown of suv4-20h enzymes.

We co-injected 900pg of a commercially available full-length human clone of PHF8 with H1H2Mo into one of two blastomeres of a 2-cell stage embryo (see Figure 3.1). We also included CoMo, and a rescue mRNA control by co-injecting morpholino and Lacz mRNA, which has no effect on ciliogenesis. This was to ensure that the rescue effects were specific to PHF8 instead of non-specific effects of increasing the cellular mRNA level. Injection of PHF8 significantly restored cilia staining in H1H2Mo embryos, while the LacZ control did not (Figure 3.5 A). Embryos showing a ciliogenic defect decreased from 90% in H1H2Mo embryos to 25% in the rescue condition (H1H2Mo + PHF8) (Figure 3.2 B).

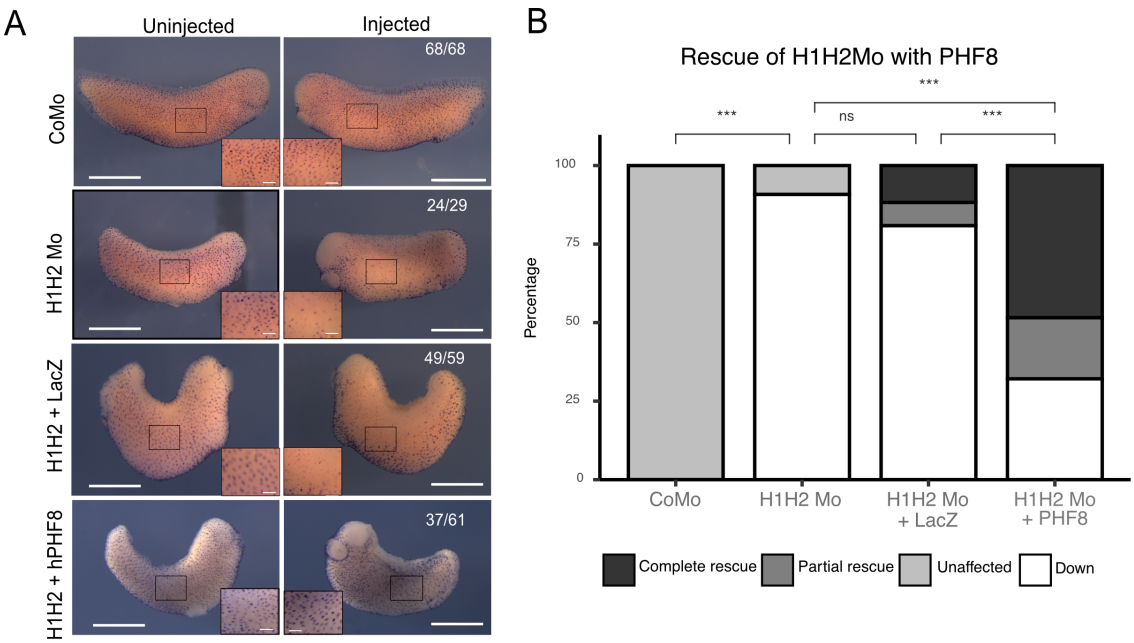

Figure 3.5: Rescue of suv4-20h1/h2 double knockdown phenotype with PHF8. A) Representative immunocytochemistry images of tailbud stage embryos stained for cilia (acetylated α -tubulin). Embryos are injected in one cell at the two-cell stage, resulting in laterally affected embryos. The uninjected side is depicted on the left and the injected side is depicted on the right. N = 3 biol. replicates. Scale bars = 1 mm (whole embryo) and 200 µm (inserts). B) Percentage of embryos either affected by morpholino injections (CoMo, H1H2Mo), or rescued by PHF8 injection. PHF8 rescues significantly, while LacZ shows no significant difference when compared to H1Mo. Significance is indicated by asterisks; * = $p < 0.05$, ** = $p < 0.01$, *** = $p < 0.001$, ns = not significant. Adapted and reprinted with permission from Life Science Alliance (Angerilli, Tait, *et al.*[151]).

To better visualize the subcellular structures of the MCCs, we used confocal microscopy following the injection scheme detailed in Figure 3.1 to generate mosaic embryos (Figure 3.6 A). We found that approximately 75% of H1H2Mo injected embryos showed cilia and actin cap defects (Figure 3.6 B, C). PHF8 significantly restored cilia assembly and apical actin meshwork density in 85% of MCCs. The mRNA control, LacZ, did not significantly rescue either structure.

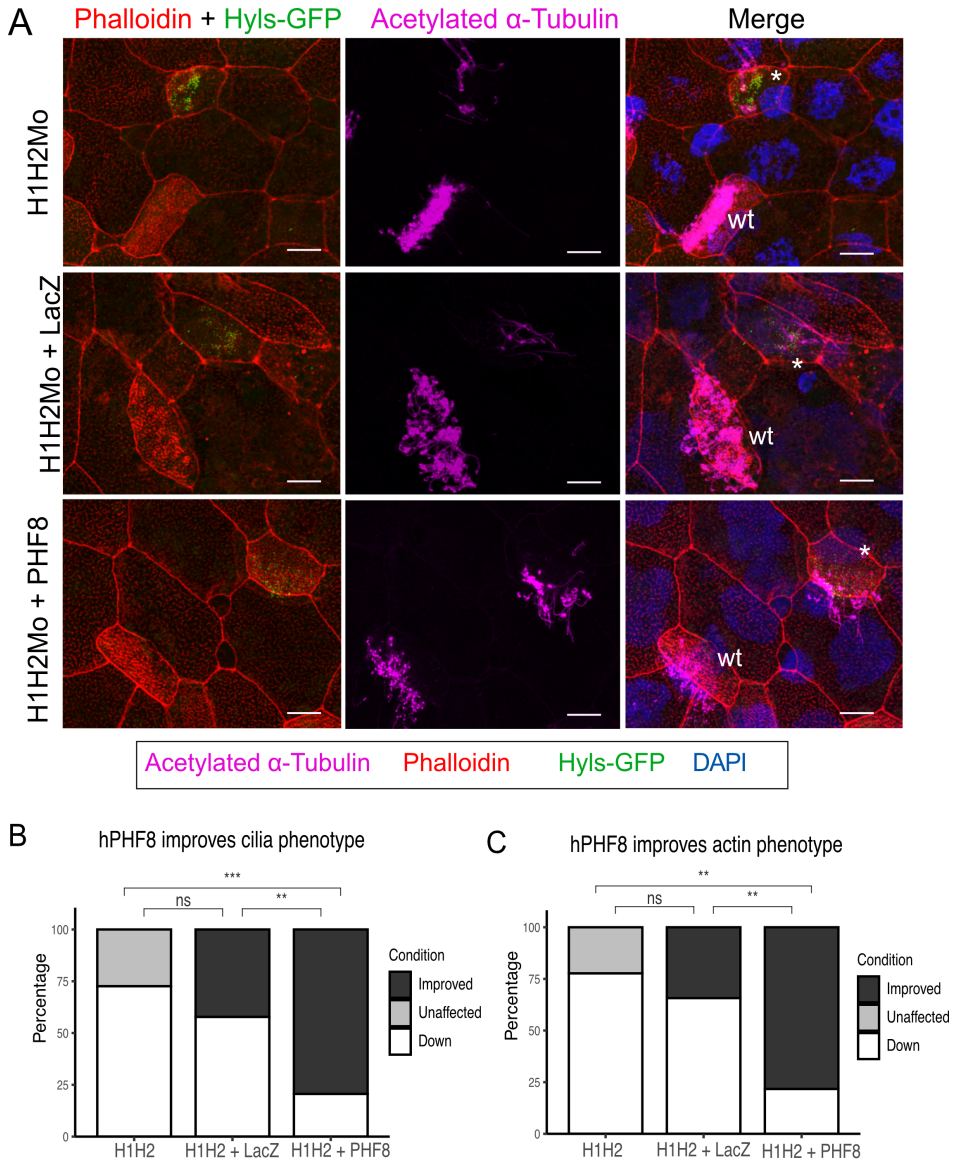

Figure 3.6: Rescue of cellular structures by PHF8 overexpression. Representative confocal images of multiciliated cells on the epidermis of tailbud stage embryos upon knockdown of suv4-20h1/h2 (H1H2Mo) and rescue with either LacZ (mRNA control) or hPHF8 mRNA. The basal bodies are green (hyls1-GFP), cilia is magenta (acetylated α -tubulin), the apical actin meshwork is red (phalloidin), and the nuclei are blue (DAPI). The embryos are injected in one of two ventroanimal blastomeres, resulting in a mosaic effect allowing wt and knockdown cells to be present in the same field of view, where knockdown cells can be visualized by green basal bodies (wt = wild-type, * = knockdown). Scale bars = 10 µm, n = 3 biological replicates. B) Quantification of cilia structures. C) Quantification of actin cap. Significance is indicated by asterisks; * = padj < 0.05, ** = padj < 0.01, *** = padj < 0.001. Adapted and reprinted with permission from Life Science Alliance (Angerilli, Tait, *et al.*[151]).

3.3.2 PHF8 partially rescues the expression of multiciliogenic genes

Once we established the rescue effect of PHF8 on the phenotypic level, we decided to determine the effect on gene expression by performing RNA-seq. We injected *Xenopus tropicalis* embryos on both sides at the 2-cell stage. For conditions see Table 3.1. Since we were primarily interested in MCCs and the epidermis, we analyzed animal caps.

Table 3.1: RNA-seq experimental conditions.

Group	Morpholino	mRNA
1	CoMo	n/a
1	H1H2Mo	n/a
2	CoMo	n/a
2	na	LacZ
2	na	PHF8
2	H1H2Mo	PHF8 (Rescue)

Animal caps are organoids cut from the blastocoel roof of blastula stage embryos (NF9), and they differentiate by default into epidermis. This results in a cleaner tissue type consisting only of the 5 cell types of the epidermis (see subsection 1.3.1) instead of the many cell types of a whole embryo. We harvested the animal caps at the neurula stage (NF16), at which time the multiciliogenic gene program is well underway. Including a control morpholino condition allowed us to harmonize and analyse the data with the previous experiment from the lab which included H1H2Mo injected animal caps[146]. Group 1 represents conditions from Angerilli [146] and Group 2 indicates new conditions (Table 3.1). However, because the two experiments were performed at separate times and sequenced on different sequencing platforms, a batch correction was required. After batch correction, the control conditions clustered together well in a principle component analysis. H1H2Mo and the rescue condition could be best resolved on the second principal component (Figure 3.7).

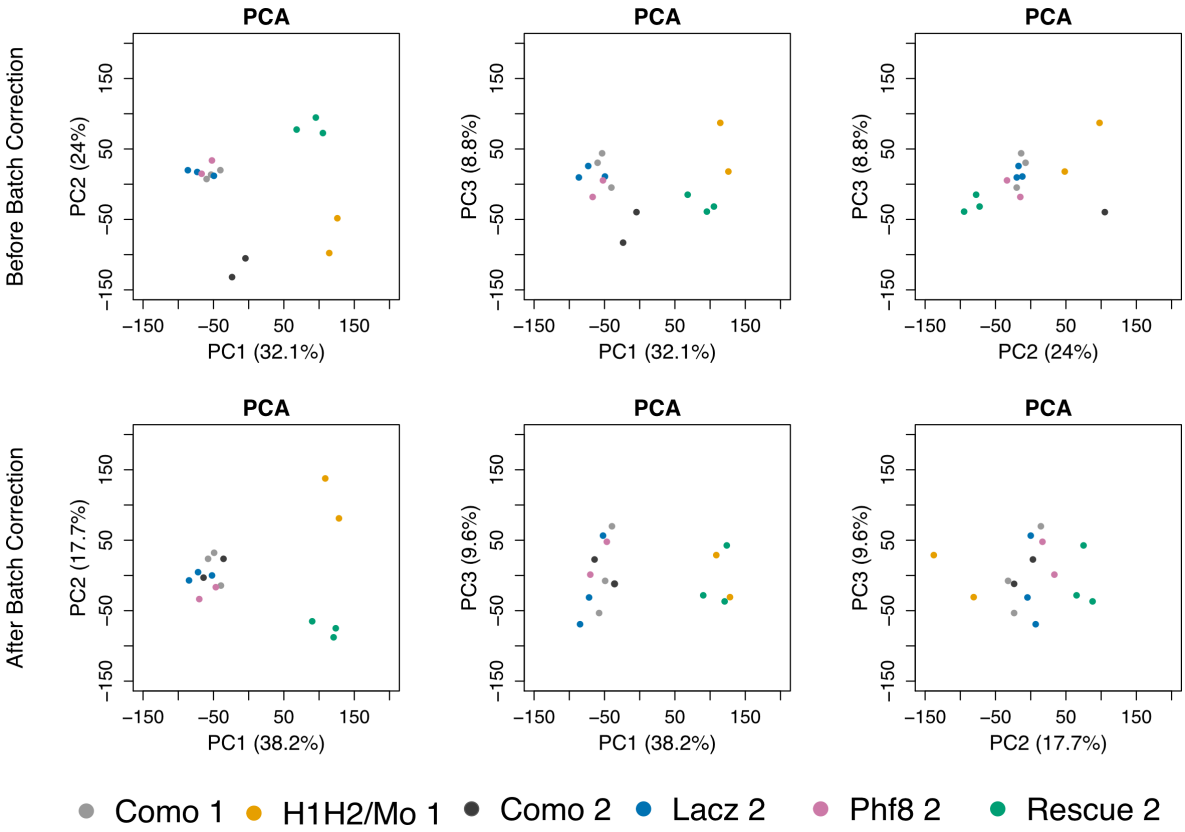

Figure 3.7: Condtions cluster on the second principal component after batch correction. Principal component analysis for RNA seq analysis of knockdown and rescue conditions before (A), and after (B) batch correction. The X and Y axes represent the components that are responsible for the maximum variance.

We checked the effect of LacZ on expression against CoMo and saw no significantly misregulated genes (Figure 3.8 A, B). PHF8 overexpression alone also did not have a significant effect on gene expression, however the expression was not as tightly correlated to CoMo gene expression as LacZ (Figure 3.8 C, D). In the PHF8 rescue condition (H1H2Mo + PHF8) we found 4551 misregulated genes; 2384 upregulated and 2167 downregulated (Figure 3.9). We normalized gene expression in the rescue condition to expression in the PHF8 overexpression condition in order to isolate for the rescuing effect and remove the effect of PHF8 alone. Because of the small but not significant effect of PHF8 mRNA injection on gene expression, we normalized to PHF8 alone in order to to interrogate the effect of PHF8 in the context of suv4-20h1/2 depletion (Figure 3.8).

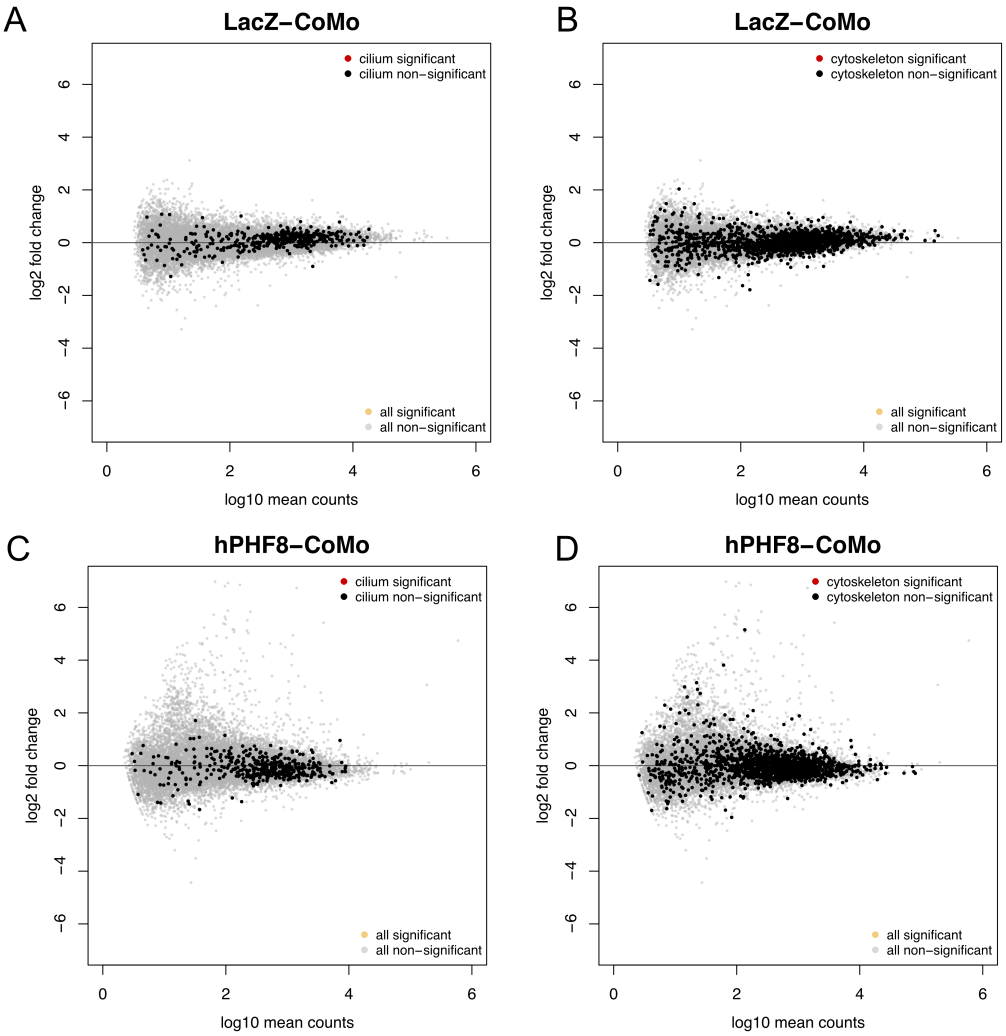

Figure 3.8: PHF8 and LacZ overexpression do not affect gene expression. MA plots showing gene expression changes in PHF8 (A, B), or LacZ (C, D) overexpressing animal caps normalized to control morpholino injected caps. Genes are represented by light grey dots, and cilium (A, C) or cytoskeletal (B, D) genes in black. There are no misregulated genes in these conditions (padj < 0.05). Adapted and reprinted with permission from Life Science Alliance (Angerilli, Tait, *et al.*[151]).

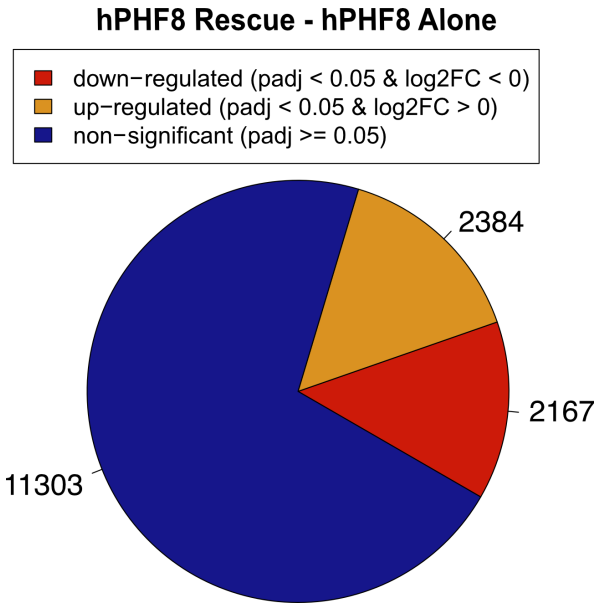

Figure 3.9: Rescue with PHF8 alters gene expression. The number of misregulated genes in PHF8 rescued animal caps vs. PHF8 alone. Downregulated genes are represented in red, upregulated genes are represented in yellow. Adapted and reprinted with permission from Life Science Alliance (Angerilli, Tait, *et al.*[151]).

To determine the rescuing effect of PHF8, we wanted to focus our analysis on genes that were downregulated in the suv4-20h1/2 knockdown. This cohort contains 2052 total genes. In the context of the PHF8 rescue we find 1663 of these genes have improved in their expression, meaning that they are returning to a level closer to that of their expression in the CoMo condition while 389 genes were further downregulated. In total 81% of genes improved their expression while 18% went further down upon PHF8 rescue (Figure 3.10).

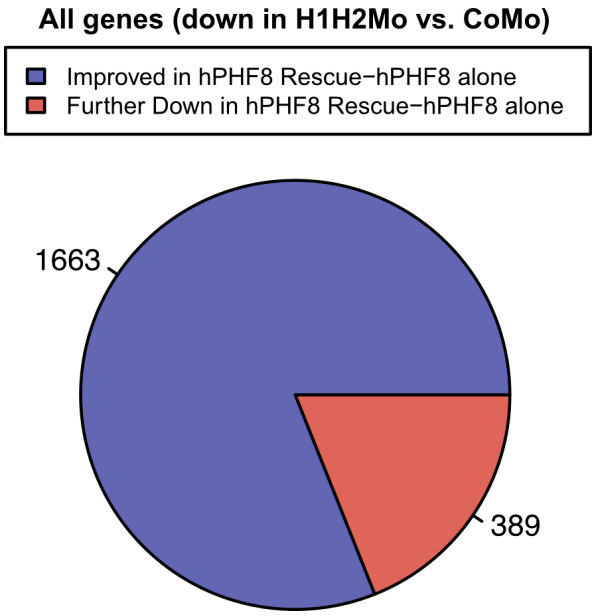

Figure 3.10: PHF8 improves gene expression in suv4-20h1/2 knockdown embryos. To investigate whether genes that are sensitive to suv4-20h1/2 knockdown (H1H2Mo) can be rescued by hPHF8, we focus on genes that were downregulated in H1H2Mo vs. CoMo. This pie chart shows the number of genes that were improved in their expression by returning towards control expression levels (blue) vs. genes that were further downregulated (red). Of all the misregulated genes, 76.6 % had improved expression. Adapted and reprinted with permission from Life Science Alliance (Angerilli, Tait, *et al.*[151]).

We were particularly interested in how cilium and cytoskeleton genes would respond to PHF8 rescue. When we looked closer at cilium genes that were downregulated in the knockdown experiment, we found that 140/181 (77%) are improved in their expression, while 43 are further down. In the log2fold change plot, genes of interest are highlighted in magenta (Figure 3.11 A, B). Genes above the diagonal line are returning back towards their normal expression level, while genes below the diagonal line are becoming further misregulated. In the rescue 290/363 cytoskeleton genes that were downregulated in the KD improved (80%), and 73/363 (20%) were further downregulated (Figure 3.11 C, D). While we do not see a perfect rescue of ciliogenic and cytoskeletal genes, there is an overall improvement in their expression. This reflects what we see on the phenotypic level and indicates that PHF8 partially alleviates the multiciliogenic defect.

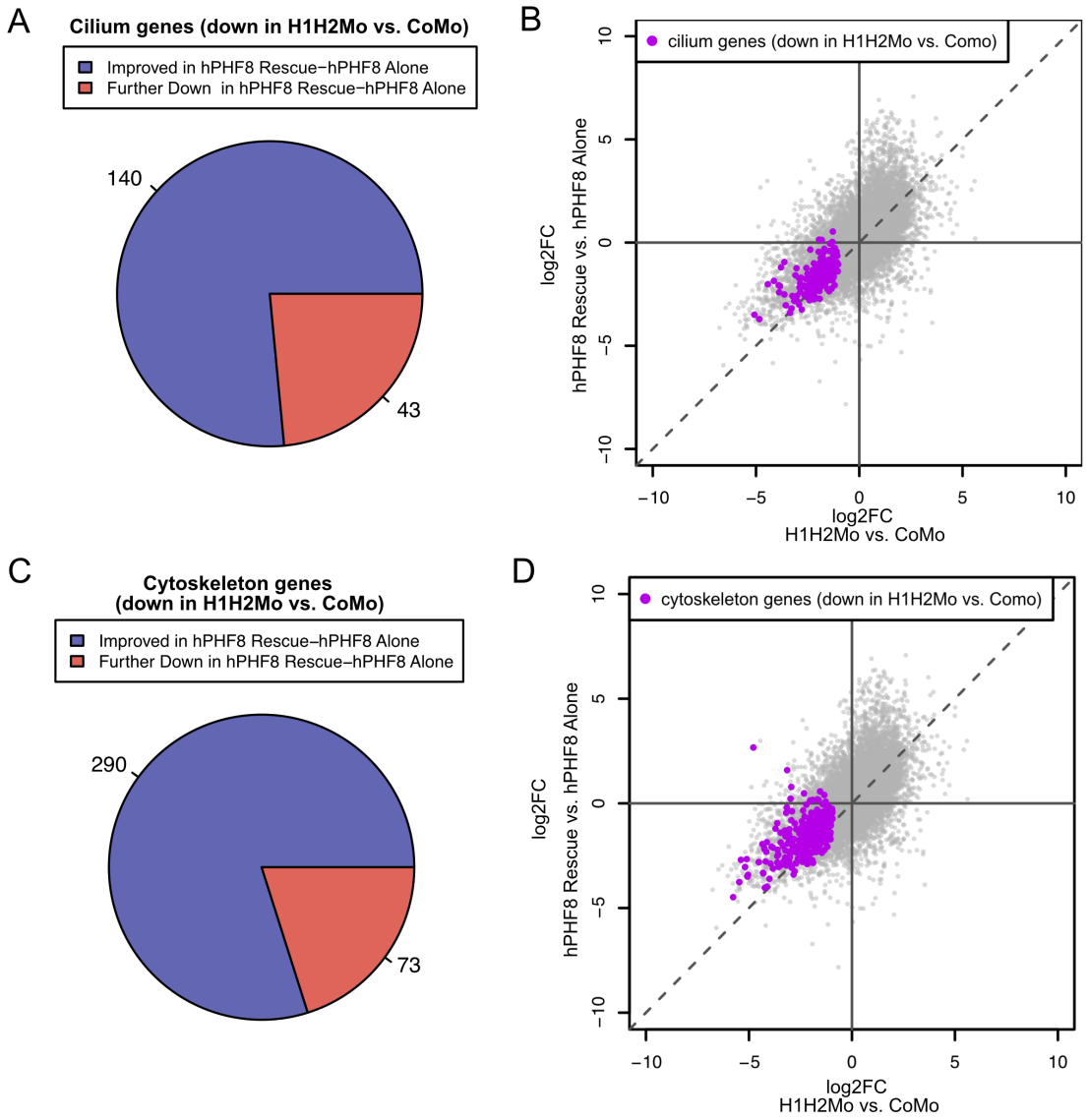

Figure 3.11: PHF8 improves gene expression of cilium and cytoskeleton genes. A, C) Number of cilium (A) or cytoskeleton (C) genes that were down in H1H2Mo vs. CoMo that have either improved in expression or were further downregulated upon rescue with hPHF8. B, D) Log2FC of cilium genes (B) or cytoskeleton genes (D) that were downregulated in H1H2Mo vs. CoMo (knockdown) compared to hPHF8 rescue vs. hPHF8 alone animal caps. Dashed line indicates no difference in expression between the knockdown and the rescue. Genes above the dashed line have improved expression and genes below the dashed line are further down. N = 3 biological replicates. Adapted and reprinted with permission from Life Science Alliance (Angerilli, Tait, *et al.*[151]).

3.3.3 PHF8 does not have an effect on global H4K20me1 levels

To quantify the effect of PHF8 overexpression and rescue on the H4K20 methyl landscape, we performed mass spectrometry. We did not detect significant changes in H4K20 methyl abundances (Figure 3.12). We also noted no significant differences in H3K9 and H3K27 methylation (data not shown). The lack of effect on H4K20 methylation could be due to the fact that SET8 writes H4K20me1 indiscriminately throughout the genome, while PHF8 is targeted to promoters by its PHD finger which binds to H3K4me2/me3. We would expect the changes in H4K20me1 generated by suv4-20h1 knockdown to be widespread, while PHF8 has a smaller and more specific set of targets, so the effect may be too small to be detected in bulk chromatin.

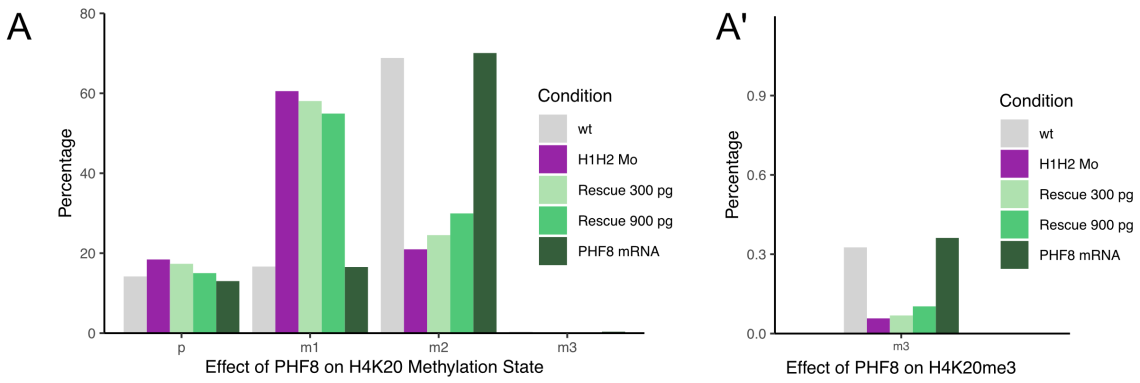

Figure 3.12: PHF8 does not affect H4K20 methyl levels. Relative abundance of (A) unmethylated H4K20, H4K20me1, H4K20me2, and (A') H4K20me3 in neurula-stage *Xenopus laevis* detected by mass spectrometry. Embryos were injected with H1H2Mo, H1H2Mo + 300 pg of PHF8 mRNA (Rescue 300 pg) or H1H2Mo + 900 pg of PHF8 mRNA (Rescue 900 pg), or PHF8 mRNA alone. Wt embryos were also included as a control. No significant changes were detected. N = 3 biological replicates.

3.3.4 Cilium and cytoskeleton are distinct but overlapping GO terms

We noticed that cilium and cytoskeleton are closely related GO terms, most likely containing overlapping genes, so we decided to quantify the overlap between them. We find 1640 cytoskeletal genes and 449 ciliogenic genes. 296 of these genes are shared by both GO terms (65% of cilium genes and 22% of cytoskeleton genes). In the downregulated genes, we find 186 cilium genes and 372 cytoskeleton genes, with 144 genes shared between the two terms (77%

of cilium genes and 38% of cytoskeleton genes) (Figure 3.13 A, B). Building multiciliated cells involves repurposing many of the proteins required for other cellular processes like mitosis (e.g., tubulins and centriolar proteins) and the formation of other cellular structures like neurite outgrowths. For this reason, it is not surprising that these two gene categories contain so many overlapping genes. Nevertheless, it is important to note that these are distinct but related GO terms that are preferentially affected by the downregulation of suv4-20h enzyme levels.

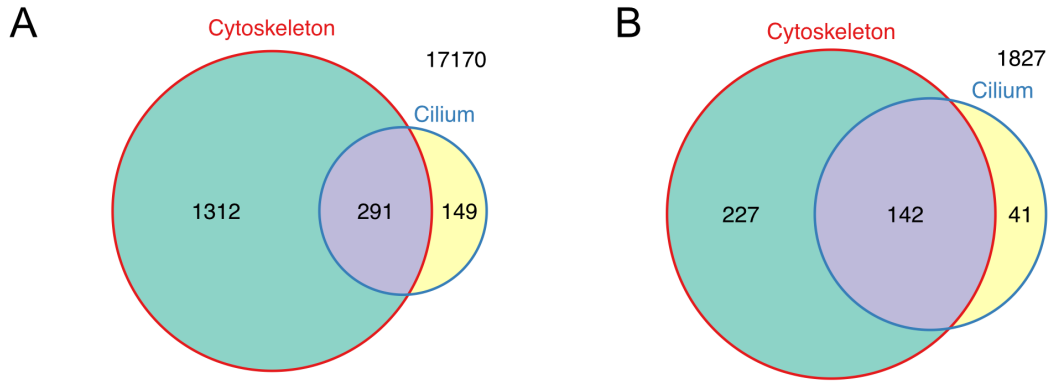

Figure 3.13: Cilium and Cytoskeleton are overlapping but distinct GO terms. Venn diagram depicting the number of genes that fall into the category of "cilium" or "cytoskeleton" in the suv4-20h1/h2 double knockdown RNA seq experiment. A) shows all detected genes. B) shows only significantly downregulated genes. Adapted and reprinted with permission from Life Science Alliance (Angerilli, Tait, *et al.*[151]).

3.4 Single knockdown of suv4-20h1

3.4.1 Suv4-20h1 knockdown is sufficient for the multiciliogenic phenotype in *Xenopus laevis*

It was previously observed by our lab that the knockdown of suv4-20h1 alone is sufficient to produce the ciliogenic defect in *Xenopus tropicalis*[146]. However, the relationship between the transcriptome signatures of suv4-20h single and double morphants remained unknown. To clarify this point, we investigated the consequences of a single suv4-20h1 or suv4-20h2 knockdown in *Xenopus laevis* embryos. First, we performed confocal microscopy on tailbud

stage embryos (NF27) injected in one of two cells with H1Mo or H2Mo alone. We found that H1Mo alone also has a strong effect on the cilia and actin cap of MCCs, while H2Mo had no effect on MCCs (Figure 3.14).

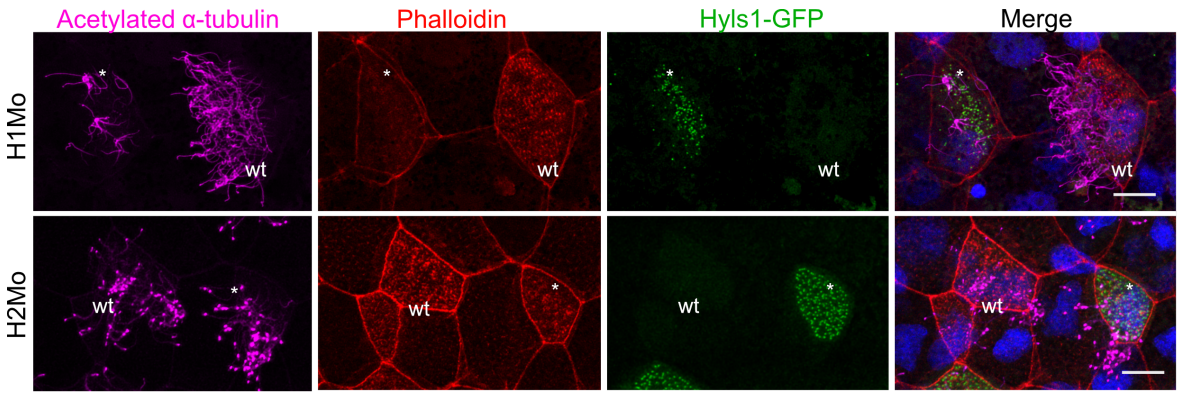

Figure 3.14: Ciliogenesis defects are only caused by suv4-20h1. A) 4-channel confocal images depicting single knockdowns of suv4-20h1 (H1Mo) and suv4-20h2 (H2Mo) in tailbud-stage *Xenopus laevis* embryos. The basal bodies are green (hyls1-GFP), cilia is magenta (acetylated α -tubulin), the apical actin meshwork is red (phalloidin), and the nuclei are blue (DAPI). The embryos are injected in one of two ventroanimal blastomeres, resulting in a mosaic effect allowing wt and knockdown cells to be present in the same field of view, where knockdown cells can be visualized by green basal bodies (wt = wild-type, * = knockdown). Scale bars = 10 µm.

We were also interested in whether the suv4-20h1 knockdown phenotype could be alleviated by PHF8 overexpression in a similar manner to suv4-20h1/2 double knockdown. Again, we performed a rescue experiment and found that PHF8 improves the condition of cilia tufts in approximately 60% of embryos (Figure 3.15 A, B). At the confocal level, we saw that PHF8 is able to improve the condition of cilia in approximately 80% of injected MCCs (Figure 3.16 B) and the actin cap in approximately 70% of injected MCCs (Figure 3.16 C). Overall, we found no difference in the strength or prevalence of the phenotype between the single knockdown of suv4-20h1 and the double knockdown. This is further suggests that suv4-20h1 alone is required for ciliogenesis.

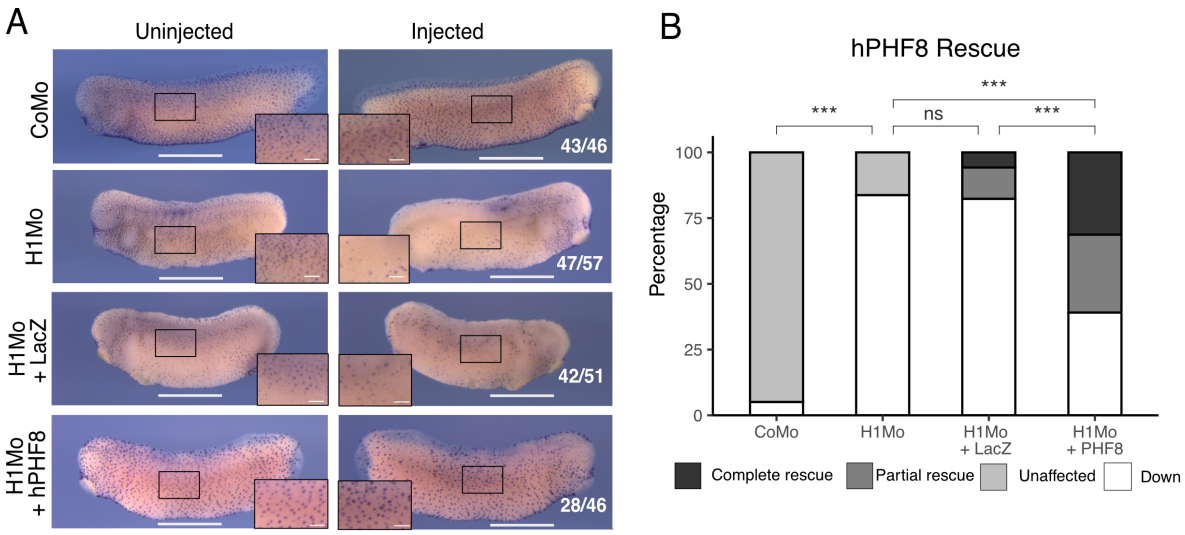

Figure 3.15: Rescue of suv4-20h1 single knockdown phenotype with PHF8. A) Representative immunocytochemistry images of tailbud stage embryos with cilia tuft staining (acetylated α-tubulin). Embryos are injected in one cell at the two-cell stage, resulting in laterally effected embryos. The uninjected side is depicted on the left and the injected side is depicted on the right. N = 3 biol. replicates. Scale bars = 1 mm (whole embryo) and 200 µm (inserts). B) Percentage of embryos either affected by morpholino injections (CoMo, H1Mo), or rescued by PHF8 injection. PHF8 rescues significantly, while LacZ shows no significant difference when compared to H1Mo. Significance is indicated by asterisks; *** = $p < 0.001$, ns = not significant. Adapted and reprinted with permission from Life Science Alliance (Angerilli, Tait, *et al.*[151]).

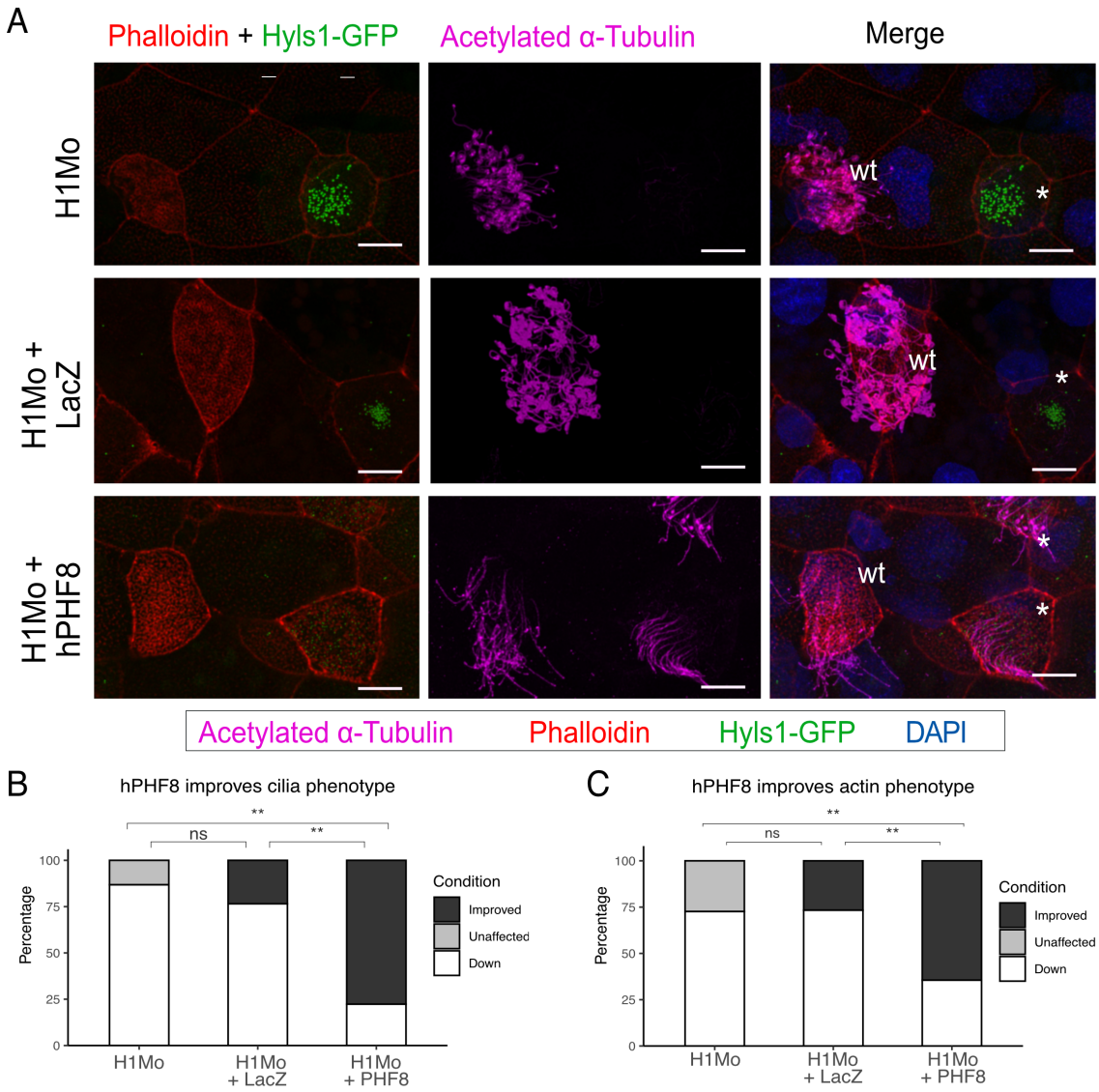

Figure 3.16: Confocal analysis of PHF8 rescue. A) Representative confocal images of multiciliated cells on the epidermis of tailbud stage embryos upon knockdown of suv4-20h1 (H1Mo) and rescue with either LacZ (mRNA control) or hPHF8 mRNA. The basal bodies are green (hyls1-GFP), cilia is magenta (acetylated α -tubulin), the apical actin meshwork is red (phalloidin), and the nuclei are blue (DAPI). The embryos are injected in one of two ventroanimal blastomeres, resulting in a mosaic effect allowing wt and knockdown cells to be present in the same field of view, where knockdown cells can be visualized by green basal bodies (wt = wild-type, * = knockdown). Scale bars = 10 µm, n = 3 biological replicates. B, C) Quantification of A). Percentage of multiciliated cells showing improved cilia (B) or actin cap (C) upon mRNA rescue. PHF8 rescues significantly, while LacZ shows no significant difference when compared to H1Mo. Significance is indicated by asterisks; ** = $p < 0.01$, ns = not significant. Adapted and reprinted with permission from Life Science Alliance (Angerilli, Tait, *et al.*[151]).

Since we hypothesized that the ciliogenic phenotype was caused by the global shift towards

H4K20me1, we decided to test whether catalytic activity of suv4-20h1 is required for ciliogenesis. So, we introduced two mutations (N248A and Y283A) into the SET domain of a suv4-20h1 *Xenopus tropicalis* cDNA by point mutagenesis (Figure 3.17 A). These mutations are predicted to be necessary for suv4-20h1 catalytic activity. Based on structural data, these residues are highly conserved across several SET domain-containing proteins and are required for S-adenosylmethionine binding[153,154]. This cDNA also contains silent mutations in the region targeted by the morpholino, rendering it insensitive to translation blocking without altering the coding capacity of the mRNA. Mouse cDNAs bearing the same mutations have been previously shown by our lab to abolish the catalytic activity of suv4-20h1[144]. We then performed rescue experiments with both the wt and catalytically inactive (c.i.) mRNA by co-injecting with H1Mo (Figure 3.17 B - B”’) .

We found that MCC condition was improved in 75% of embryos injected with wt mRNA. On the other hand, c.i. suv-20h1 was not able to rescue significantly at either the 300 pg or 900 pg dose. This indicates that catalytic activity is required to support axoneme formation (Figure 3.17 C).

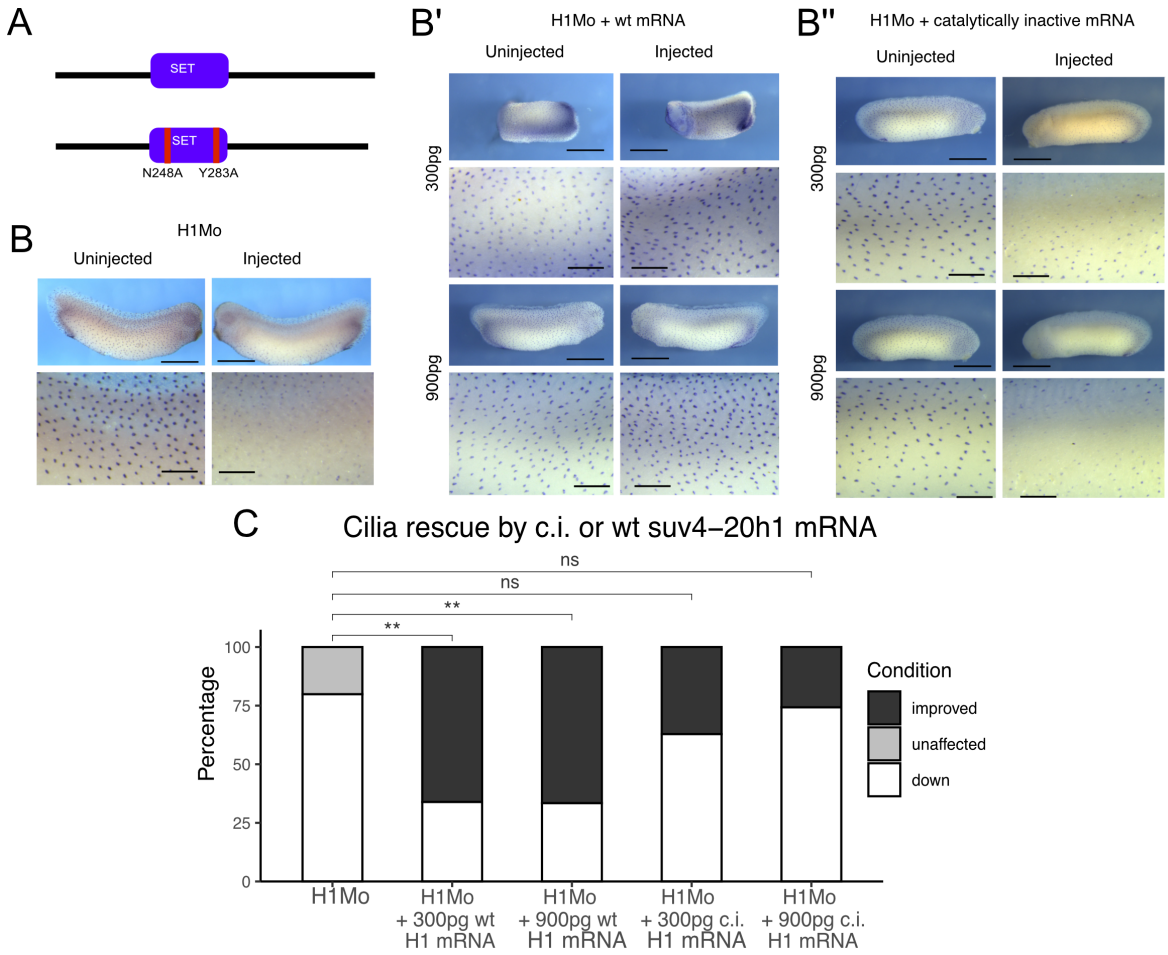

Figure 3.17: Only catalytically active suv4-20h1 mRNA rescues the ciliogenic phenotype. A) Schematic of deletions in the SET domain of suv4-20h1. Two key residues of the SET domain, N248A and Y283A, were mutated to abolish catalytic activity of suv4-20h1. B, B', B") Representative immunocytochemistry images from tailbud stage embryos injected with suv4-20h1 morpholino (H1Mo) (B), H1Mo + wild-type suv4-20h1 mRNA (B'), or H1Mo + catalytically inactive suv4-20h1 mRNA (B"). Scale bars = 1 mm (whole embryo), or 200 µm (inserts) and n = 3 biological replicates. C) Quantification of B-B") Percentage of embryos either affected by morpholino injections (H1Mo, CoMo) or rescued by suv4-20h1 mRNA injection. Wt suv4-20h1 mRNA rescues significantly, while catalytically inactive suv4-20h1 mRNA shows no significant difference when compared to H1Mo. Significance is indicated by asterisks; ** = $p < 0.01$, ns = not significant. Adapted and reprinted with permission from Life Science Alliance (Angerilli, Tait, *et al.*[151]).

Similarly, we aimed to determine whether the catalytic activity of PHF8 is necessary for the rescue of cilia tufts. To investigate this, we utilized two human PHF8 clones from [155], both of which are truncated to include amino acids 1-489 along with a nuclear localization signal. We used one wt cDNA (489 Wt) and one catalytically inactive cDNA (489 c.i). This truncation results in a gain-of-function variant, as the C-terminus inhibits catalytic activity

of the enzyme[155]. We injected either 489 Wt, 489 c.i., or luciferase as an mRNA control in conjunction with either CoMo or H1Mo. We also injected lacZ mRNA to act as a lineage tracer. We fixed embryos at the tadpole stage and performed wholemount immunocytochemistry along with β-Galactosidase staining, which stains LacZ injected regions blue, to see the localization of mRNA injection (Figure 3.18 A).

We find that only the 489 Wt can significantly rescue cilia tuft formation. In total 96.5% of H1Mo + Luciferase injected embryos and 86.8% of H1Mo + 489 c.i. embryos show cilia tuft defects, while only 36% of H1Mo + 489 wt show cilia tuft defects. This is an indication that the catalytical activity of PHF8 is required to rescue ciliogenic defects. In addition, the truncated PHF8 clones have activity in the absence of suv4-20h1 knockdown. A total of 81% of 489 Wt and 65% of 489 c.i. embryos co-injected with CoMo show an increase in cilia tuft density (Figure 3.18 B).

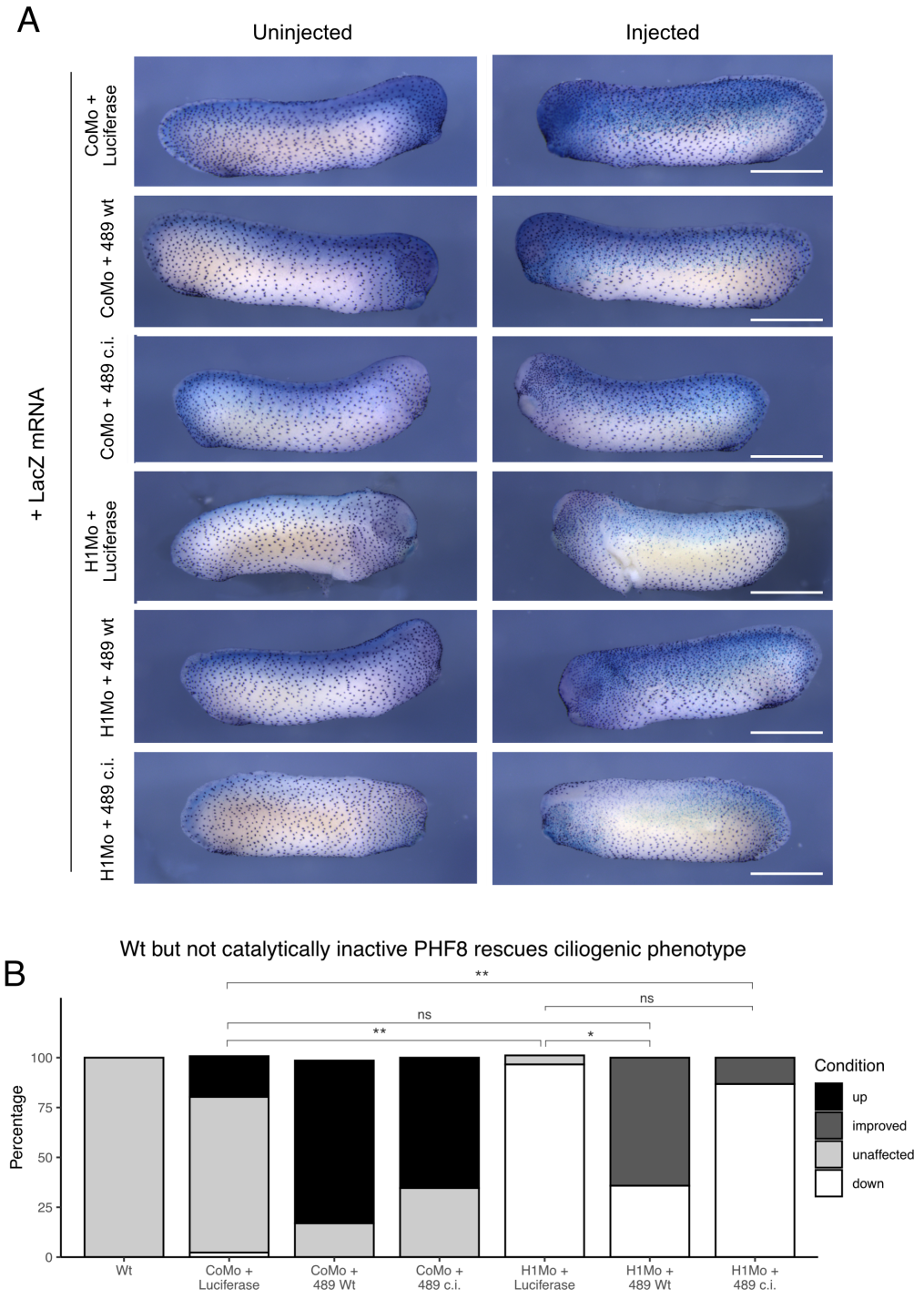

Figure 3.18: Only catalytically active PHF8 mRNA rescues the ciliogenic phenotype. A) Representative immunocytochemistry images from tailbud stage embryos injected with H1Mo or CoMo and mRNA. Scale bars = 1 mm (whole embryo), or 200 µm (inserts) and n = 3 biological replicates. B) Quantification of A). Percentage of embryos either affected by morpholino injections (H1Mo) or rescued by PHF8 mRNA injection. Wt PHF8 mRNA (489 Wt) rescues significantly, while catalytically inactive PHF8 mRNA (489 c.i.) shows no significant difference when compared to H1Mo. Significance is indicated by asterisks; * = $p < 0.05$, ** = $p < 0.01$, ns = not significant. N=4 biological replicates

3.4.2 Suv4-20h1 is responsible for transcriptional changes

Once we determined that the phenotype is caused by suv4-20h1 KD alone and dependent on catalytic activity of the enzyme, we wanted to better understand what was happening to the transcriptome of suv4-20h1 and 2 single morphants. Once again, we performed RNA-seq in NF16 animal caps, this time in *Xenopus laevis*. It is important to note that *Xenopus laevis* is allotetraploid, and has two distinct subgenomes, termed the L and S homeolog[156]. *Xenopus laevis* gene names end in .L or .S to indicate their subgenomic origin.

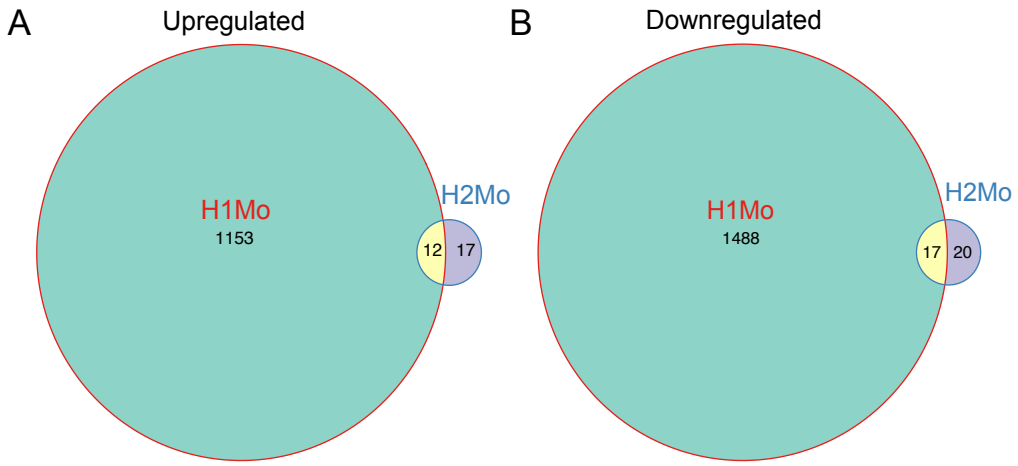

Figure 3.19: Suv4-20h1 is responsible for transcriptional changes. A, B) Venn diagrams comparing the number of upregulated (A) or downregulated (B) genes between suv4-20h1 knockdown (H1Mo) and suv4-20h2 knockdown (H2Mo) by RNA-seq. Suv4-20h1 knockdown leads to misregulation of many more genes than suv4-20h2 knockdown.

Our first and most striking observation is that, while more than 2000 genes are misregulated in H1Mo animal caps, only 83 genes are misregulated in the H2Mo injected animal caps (Figure 3.19, Figure 3.20 A, B). We attempted to perform GO analysis on H2Mo but since the cohort of misregulated genes is so small, we ended up with only 3 enriched terms; “regulation of transcription by RNA polymerase II”, “circadian rhythm”, and “circadian rhythm of gene expression”. One gene that stands out as being particularly significantly misregulated by suv4-20h2 knockdown is the S homeolog of gsx1, a homeobox gene that is part of a family of transcription factors that has been shown to promote neural differentiation in *Xenopus*[157].

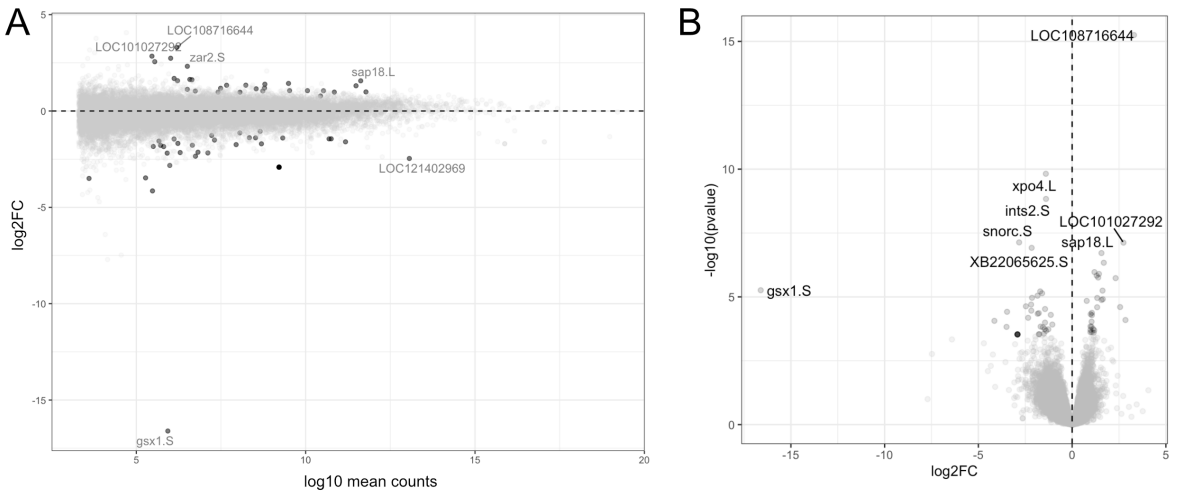

Figure 3.20: Suv4-20h2 has very little effect on transcription. A) MA plot showing Log2 fold change (y axis) and log 10 mean counts (y-axis) of genes comparing suv4-20h2 knockdown (H2Mo) against control knockdown (CoMo). B) Volcano plot showing -log10(pvalue) (yaxis) and log2 fold change of genes comparing H2Mo against CoMo. Only 83 genes are significantly misregulated upon suv4-20h2 knockdown. Significantly misregulated genes are shown in dark grey (padj < 0.1).

The story is quite different with H1Mo-injected animal caps. With around 1000 misregulated genes in either direction, the transcriptome is significantly altered (Figure 3.21 A, B). We were able to perform GO analysis for H1Mo and we found that the link to ciliogenesis is retained in the downregulated genes. Immediately, the top misregulated genes showed a ciliogenic connotation. For example, cntln is a centriolar linker protein that also binds microtubules[158], IFT88 is an intraflagellar transport protein that plays a role in anteretrograde transport of ciliogenic components[159], and dnal4 is a dyenein protein associated with motile cilia[160]. With this in mind, it is not surprising that all of the top 20 most downregulated GO terms relate to cilia or cytoskeleton, including “cilium movement”, “cilium organization”, and “cell projection assembly” (Figure 3.22 A).

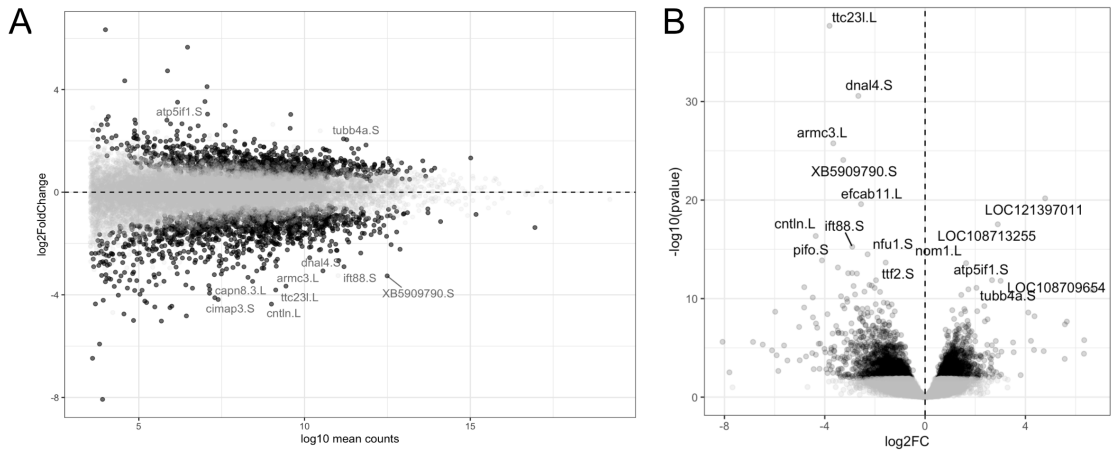

Figure 3.21: Suv4-20h1 has a strong effect on transcription. A) MA plot showing log2 fold change (x-axis) and log 10 mean counts (y-axis) of genes comparing suv4-20h1 knockdown (H1Mo) against control knockdown (CoMo). B) Volcano plot showing -log10(value) (y-axis) and log2 fold change of genes comparing H1Mo against CoMo. 2670 genes are significantly misregulated upon suv4-20h1 knockdown. Significantly misregulated genes are shown in dark grey (padj < 0.1).

The upregulated genes have some enriched terms that overlap with the previous double morphant RNA seq results, including mRNA processing and macromolecule localization (Figure 3.22 B). However, we were also interested to see a number of terms related to mitosis and the cell cycle, including the terms “mitotic cell cycle,” “mitotic cell cycle process,” “microtubule cell cytoskeleton organization involved in mitosis,” and “cell division.” Surprisingly, we also find a tubulin protein, tubb4a, among the top most upregulated genes. Tubb4a is one of two β-tubulins, alongside tubb4b, that contain a C-terminal motif required to associate with cilia[161]. However, while tubb4b depletion leads to striking cilia defects in the MCCs of the mouse airway and oviduct, loss of tubb4a does not affect cilia[162]. Tubb4b is also mildly downregulated upon suv4-20h1 knockdown. Tubb4a has also been shown to be a tumorigenic protein, suggesting that it plays a role in promoting proliferation[163]. Together the changes in gene expression seem to favor proliferation at the expense of forming cilia.

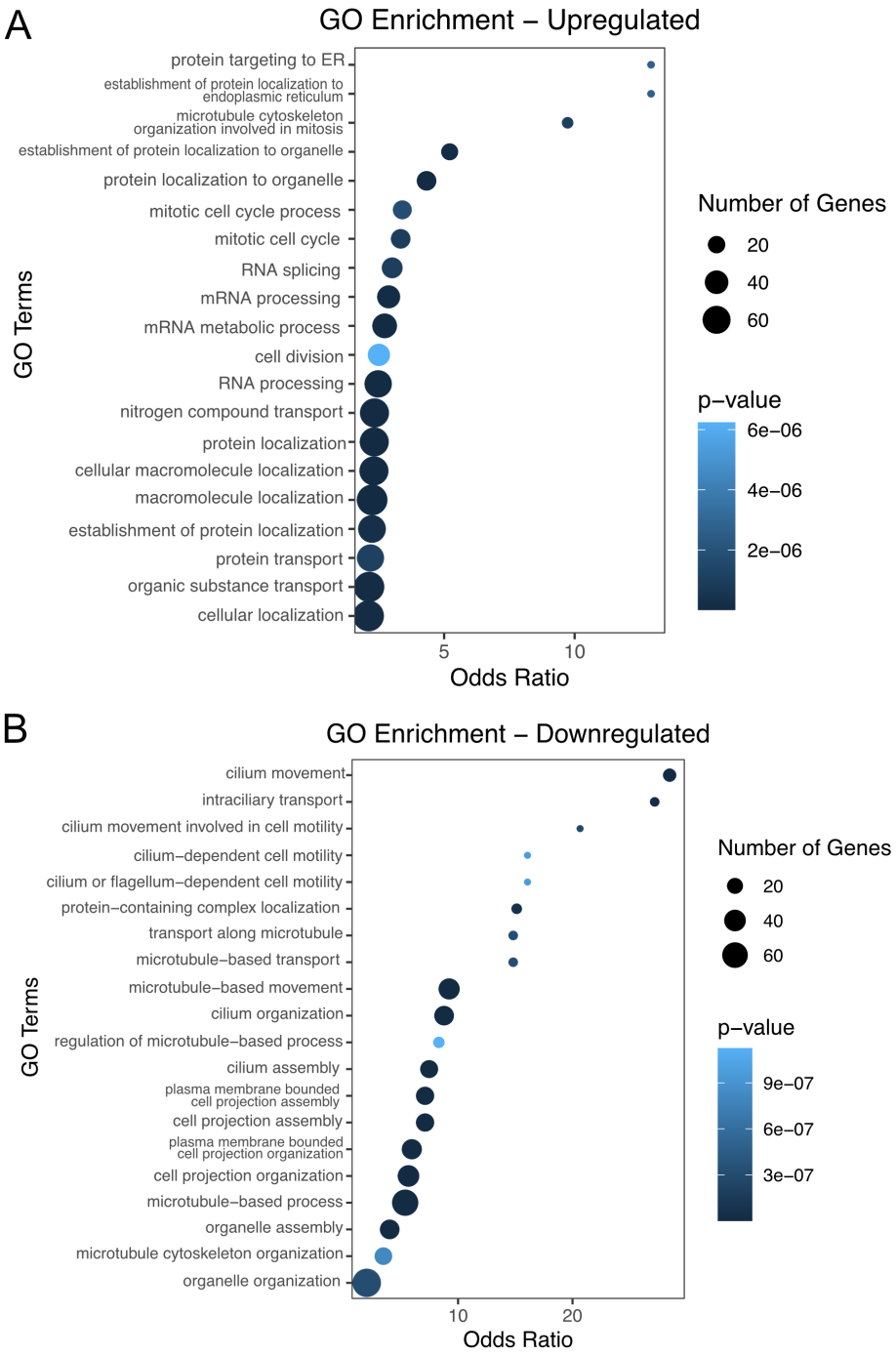

Figure 3.22: Suv4-20h1 knockdown has ciliogenic connotations in the downregulated genes. A, B) GO analysis for upregulated (A) and downregulated (B) genes in suv4-20h1 knockdown (H1Mo) animal caps. Bubble size represents the number of significantly misregulated genes per GO term, and bubble colour represents p-value. Upregulated GO terms are related to cell cycle and protein localization, while downregulated GO terms are related to cilium motility and assembly, microtubule-based processes, and cytoskeleton.

3.4.3 Expression of ciliogenic transcription factors is not affected by suv4-20h1 knockdown

Is this change in gene expression reflective of an overall change in H4K20me1 abundance? Or is a key ciliogenic regulator simply being misregulated and consequently causing this striking downregulation of ciliogenic genes? To address these questions, we looked at the fold change of the known ciliogenic transcription factors. Successful multiciliogenesis requires the execution of a delicate cascade of transcription factors (Figure 3.23 A), beginning with gemc1 and multicilin (mci), two coiled-coil domain-containing proteins related to geminin, a protein that regulates cell cycle progression[111,164]. Both gemc1 and mci are so-called master regulators of multiciliogenesis, and also have additional roles in DNA replication and origin licensing in S-phase respectively. In our dataset, neither gemc1, nor mci are misregulated when suv4-20h1 is depleted (Figure 3.23 B).

Downstream of gemc1 and mci, rfx2 and foxj1 promote cilia formation. Foxj1 was the first identified multiciliogenic transcription factor[165], and is responsible for coordinating the expression of genes related to many aspects of motile cilia formation. This includes genes involved intraflagellar transport, cilia assembly, basal body docking, axoneme outgrowth and motility itself[166–168]. Foxj1 preferentially binds to enhancers and is stabilized at ciliogenic promoters by rfx2, which acts as transcriptional coactivator of foxj1[116]. Suv4-20h1 knockdown does not significantly affect foxj1 or rfx2 expression.

In parallel to the cilia gene expression program, basal body biogenesis is largely orchestrated by c-myb and ccno[102]. C-myb is a key regulator of basal body genes, and depletion leads to a loss or delay of basal body amplification in *Xenopus*, zebrafish and mice[169,170]. Surprisingly, outside of its role in basal body biogenesis, c-myb promotes entry into S-phase and in general supports proliferation[171]. CCNO, a cyclin-like protein is expressed in MCCs and controls centriole amplification by regulating the formation of the deuterosome[172]. We find that neither of these key basal body genes are misregulated upon suv4-20h1 knockdown (Figure 3.23 B).

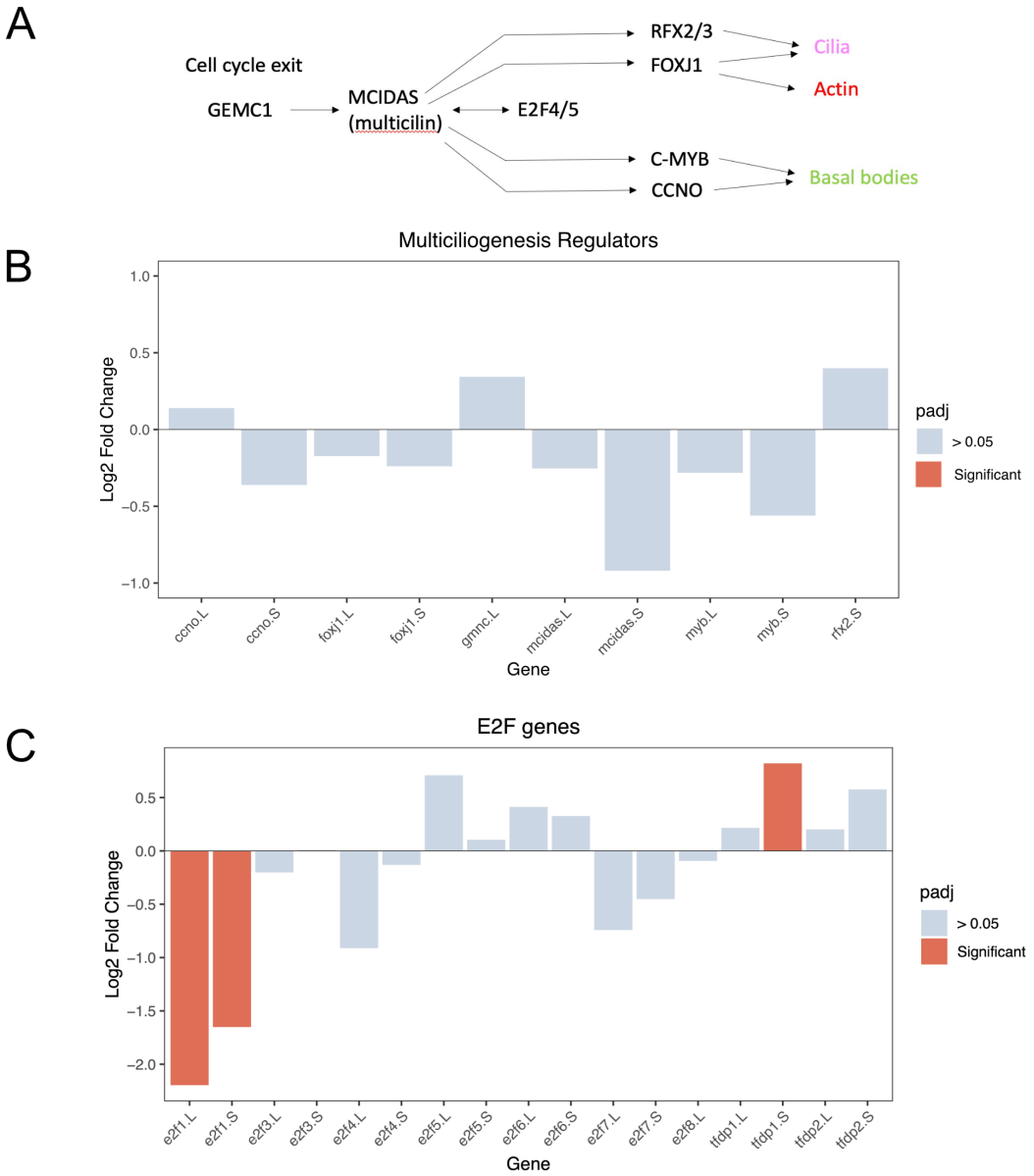

Figure 3.23: Effect of suv4-20h1 knockdown on the master regulators of ciliogenesis and E2F transcription factors. A) Schematic of the multiciliogenesis gene program (adapted from [102]). Expression of B) key multiciliogenic transcription factors and C) E2F genes based on RNA-seq data from H1Mo injected animal caps.

Another set of transcription factors that play key roles in multiciliogenesis are E2F proteins. Despite the fact that E2F family members have high sequence homology, they have a diverse array of functions, including cell cycle regulation, DNA replication, and differentiation, and can sometimes have antagonistic effects on these cellular processes. In general, E2F proteins

can be split into the cell cycle activating E2Fs, including E2F1,2, and 3, and the cell cycle-repressing E2Fs, including E2F4, 5, 6, 7, and 8[173]. E2F6 and 7 have additional functions in transcriptional repression[174]. Cell cycle-repressive E2Fs have also been shown to regulate the transcription of multiciliogenic genes. As mci lacks a DNA binding domain, it binds directly to E2F4/5, both of which repress the cell cycle. This binding is required for basal body biogenesis, as expression of a dominant negative E2F4 in *Xenopus* skin interferes with basal body production and multiciliation[173]. Recently, a key role for E2F7 in multciliogenesis has been identified in which E2F7 attenuates the levels of DNA replication machinery expression to promote MCC differentiation over cell proliferation[175].

We looked at the change in expression of E2F family proteins and their binding partners, the tfdp proteins, to see if they were affected by suv4-20h1 knockdown. Only E2F1 was significantly misregulated by 2-fold. E2F1 is primarily involved in cell-cycle regulation and has not been shown to be involved in multiciliogenesis. Additionally, tfdp1 was significantly upregulated, with a log2 fold change of 0.82. Tfdp1 is a transcription factor binding partner of E2F1, E2F2, and E2F3. Neither E2F4, 5 or 7 were significantly misregulated (Figure 3.23 C). Indeed, investigation of gemc1 and mci, the master regulators of multiciliogenesis, foxj1 and rfx2, the coordinators of motile ciliation, and c-myb and ccno, the directors of basal body biogenesis, as well as the supporting cast of E2F transcription factors, revealed that suv4-20h1 does not affect the regulators of the cannonical multiciliogenesis program.

3.5 Multicilin overexpression

3.5.1 Phenotypic effects of multicilin overexpression

One of the limitations of the previous analysis is that MCCs are only one of five cell types in the Xenopus epidermis. The rest of the epidermis includes goblet cells, ionocytes, small secretory cells, and basal stem cells[176]. So, despite the fact that profiling animal caps provides a marked improvement over whole embryo sequencing, we wanted to reduce the complexity of the tissue even further to get a more representative transcriptomic profile of MCCs. Overexpression of mci can induce other epidermal cell types to take on a multiciliogenic

identity by generating multiple basal bodies and forming ectopic cilia[177]. We reasoned that we could induce more cells of the animal cap to adopt a multiciliated fate by overexpressing multicilin in our explants. We used a previously validated glucocorticoid receptor-containing mci construct (MCI-hGR)[116]. We injected 60 pg of MCI-hGR into 8-cell stage embryos and induced them with 10 µm dexamethasone at early gastrula-stage (NF10), before the onset of multiciliogenesis. We then allowed the embryos to develop until the tailbud stage (NF27), fixed them, and performed whole-mount immunocytochemistry against acetylated alpha-tubulin.

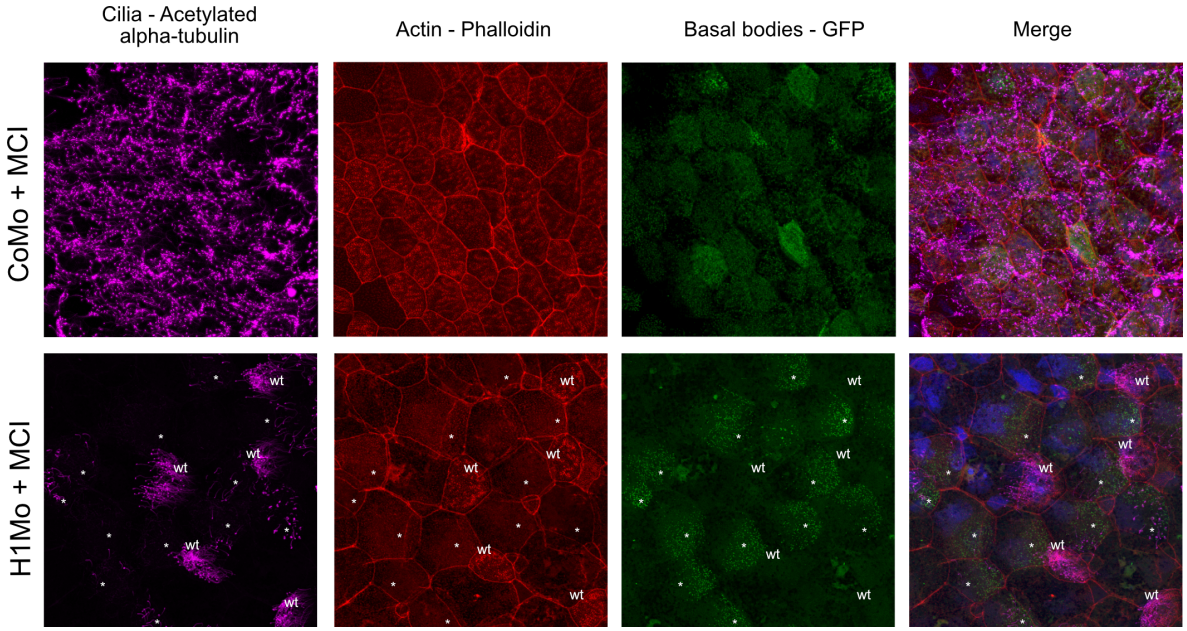

Figure 3.24: Phenotypic Effect of MCI overexpression. Representative images of confocal microscopy showing the surface of MCI-hGR overexpressing embryos. Cilia is in magenta, Actin, staining the cell borders and apical actin meshwok, is in red, basal bodies are green, and DAPI staining is shown in blue. A mosaic injection scheme is used allowing KD and wild-type cells to be seen in the same field of view (wt = wild-type, * = injected). MCI-overexpressing control embryos show most of the surface epidermis cells converted to multiciliated cells. Suv4-20h1 knockdown + MCI overexpression embryos also have an increased number of multiciliated cells (many green basal bodies), but these cells lack cilia.

Similar to what our lab has found in double-morphant embryos[145], MCI-hGR is not able to rescue the multiciliogenic phenotype in H1Mo embryos. We found that despite the fact that MCI-hGR can induce non-MCC fated cells to amplify their centrioles, it does not rescue the formation of cilia in injected cells (Figure 3.24). Due to this finding, we hypothesize that this is truly a ciliogenic phenotype and not a cell-specification phenotype. These cells are still able to emerge at the apex of goblet cells and amplify their centrioles, but something goes

wrong between centriole amplification and cilia formation.

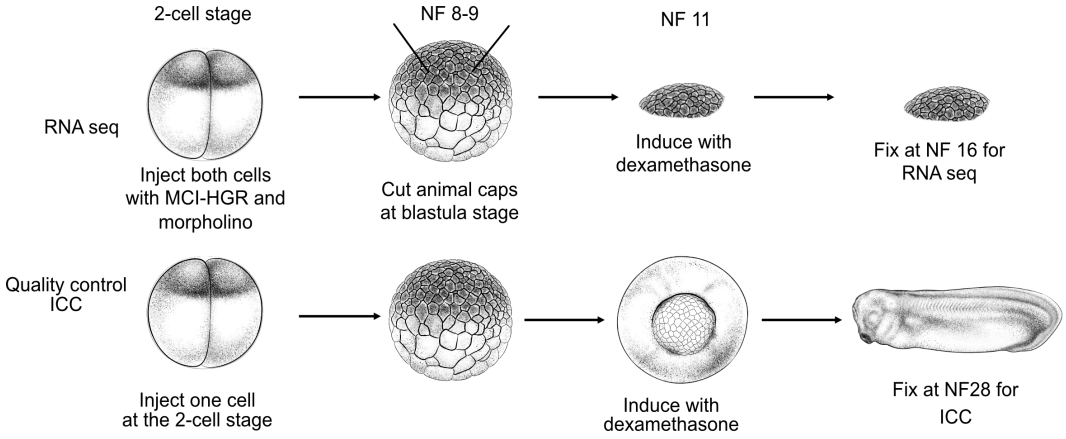

Figure 3.25: Protocol for MCC programming. Schematic of the protocol for MCI-hGR overexpression for RNA seq and quality control ICC. For RNA seq, embryos are injected radially at the 2-cell stage. Animal caps are cut from blastula-stage embryos (NF 8-9). MCI-hGR is induced with 10 μM dexamethasone at NF 11, and embryos are collected for RNA seq at NF 16. For ICC, embryos are injected in one of two cells at the two-cell stage, induced with dexamethasone, and fixed with MEMFA at tailbud stage (NF27). Xenopus illustrations © Natalya Zahn (2022)[80]

Next, we sought to determine the effect of MCI on transcription, both with and without suv4-20h1 knockdown. Our experimental approach is outlined in (Figure 3.25). We began by injecting 2-cell stage embryos with MCI-hGR and the morpholino of interest. The embryos were allowed to develop until the blastula stage (NF9), at which point we excised the animal caps. At NF11, we induced the animal caps using dexamethasone at a concentration of 10 μM, and the embryos were further developed until the neurula stage (NF16), when multiciliogenesis is well underway. At this stage, we snap-froze the animal caps and performed RNA sequencing. Given the multiple simultaneous manipulations, we added an extra quality control step. Alongside preparing animal caps for RNA sequencing, we injected embryos with morpholino and MCI-hGR for immunocytochemistry. We included conditions for CoMo + MCI, H1Mo, and H1Mo + MCI, followed by ICC. This allowed us to confirm the presence of the original suv4-20h1 knockdown phenotype and verify that the MCI-hGR injection and induction were successful (data not shown). RNA sequencing was only performed on replicates that passed all these quality control criteria.

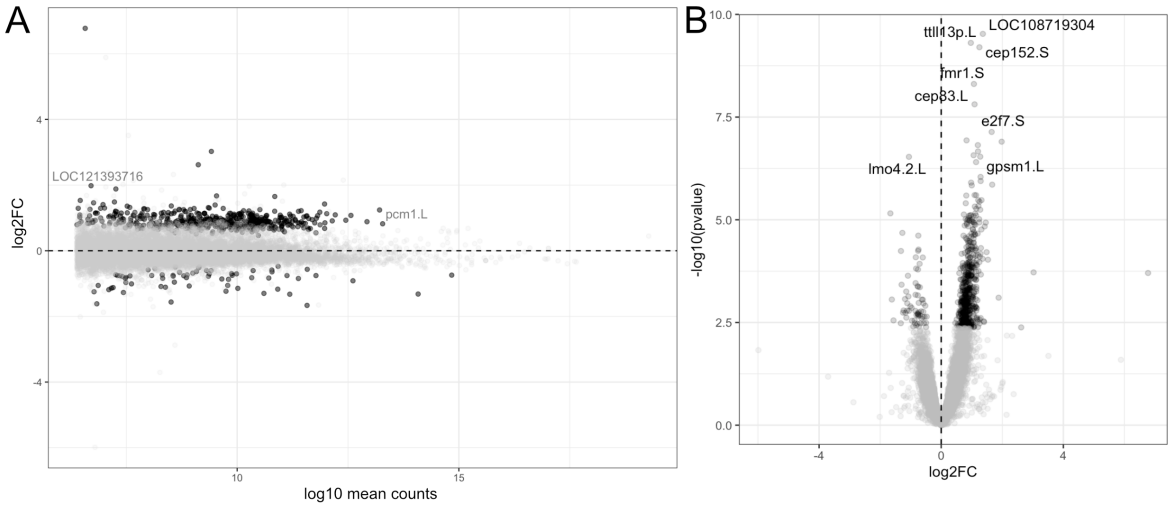

Figure 3.26: Effect of MCI overexpression on transcription. RNA seq data on control morpholino (CoMo) injected animal caps with co-injection of A) MA plot and B) volcano plot showing gene expression changes in CoMo + MCI injected animal caps. Genes are represented by light gray dots, with darker grey dots representing significantly misregulated genes (padj < 0.1). N = 3 biological replicates.

The RNA-seq experiment consists of four conditions: CoMo, CoMo + dexamethasone, CoMo + MCI + dexamethasone, and H1Mo + MCI + dexamethasone. In the CoMo + MCI condition, 591 genes were misregulated, with 525 genes upregulated and only 66 genes downregulated (Figure 3.26 A,B). As expected, GO analysis of CoMo + MCI animal caps shows that the up-regulated genes are enriched for categories related to MCCs (Figure 3.27 A). This includes terms related to the centriole cycle, cilium assembly, and microtubule organizing center organization. On the other hand, the downregulated genes show enrichment for categories related to the cell cycle, such as DNA replication initiation and regulation, and to other developmental lineages, including neuron differentiation and mesoderm development (Figure 3.27 B). This is consistent with our expectations because MCCs are post-mitotic and terminally differentiated, so processes related to DNA replication should be restricted. Additionally, we select for a very specific cell type within an explant of non-neural ectodermal origin, so we would not expect to see neuronal or mesoderm-related genes in the animal caps.

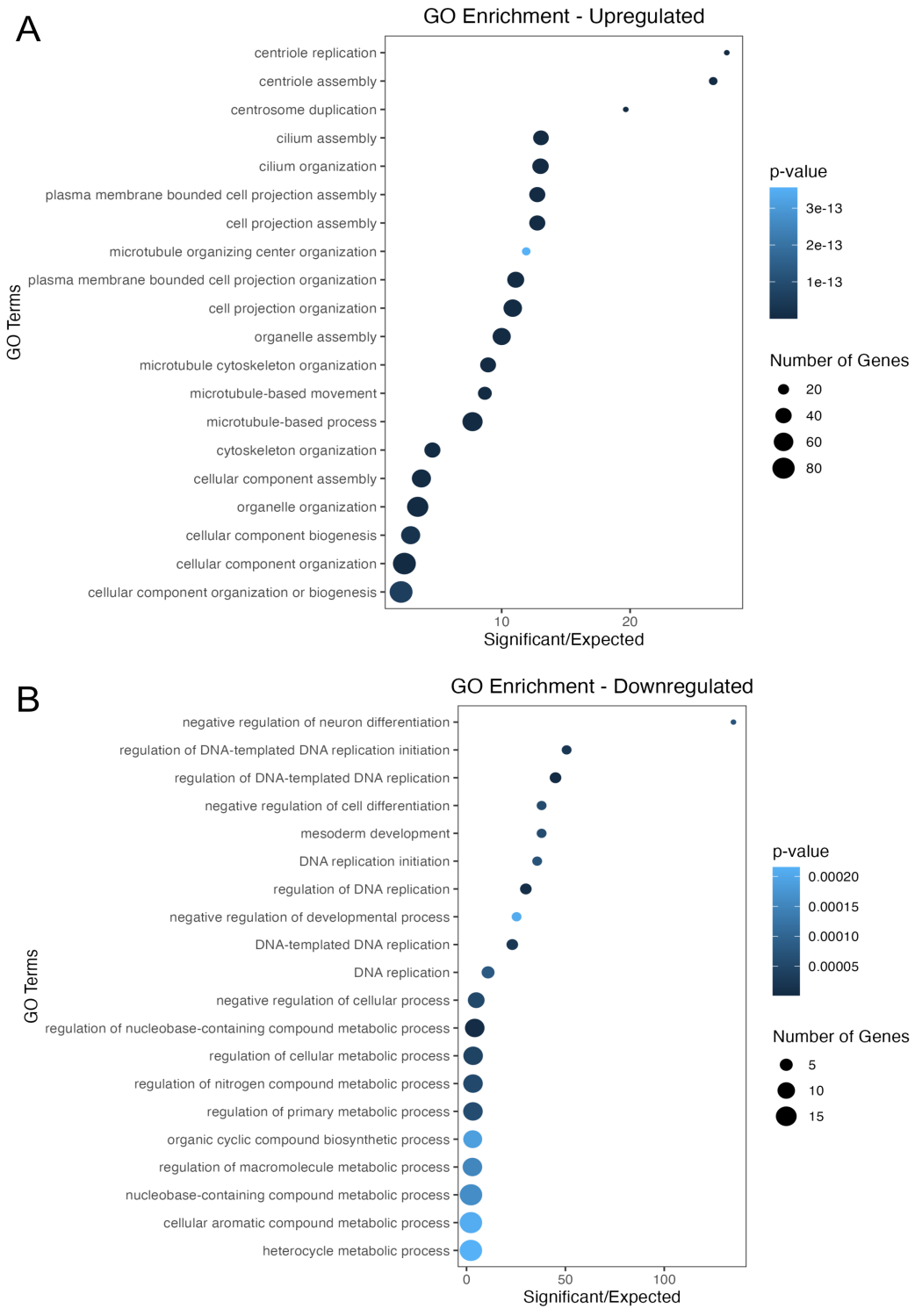

Figure 3.27: MCI overexpression leads to upregulation of cilia genes and downregulation of cell cycle genes. A, B) GO analysis for upregulated (A) and downregulated (B) genes in control morpholino (CoMo) + MCI-hGR injected animal caps. Bubble size represents the number of significantly misregulated genes per GO term and bubble colour represents p-value. Upregulated GO terms are related to centriole replication and cilium, while downregulated GO terms are related to DNA replication, differentiation, and metabolic processes.

3.5.2 Suv4-20h1 knockdown drives transcriptional changes in MCI overexpressing animal caps

Knockdown of suv4-20h1 represses ciliogenic genes, while MCI enhances their expression. Therefore, concurrent knockdown of suv4-20h1 and overexpression of MCI may have competing effects on ciliogenic gene expression. We wanted to better understand how these two regulators affect ciliogenic gene expression, so we performed a combined analysis of two RNA-seq experiments which will be referred to as Group A and Group B (see Table 3.2). We performed a batch correction on the two experiments, followed by a cluster analysis of the top responding genes across all replicates.

Table 3.2: RNA-seq experimental conditions and groups.

Group	Morpholino	mRNA
A	CoMo	n/a
A	H1Mo	n/a
A	H2Mo	n/a
B	CoMo	n/a
B	CoMo	MCI-hGR + dexamethasone
B	CoMo	no mRNA + dexamethasone
B	H1Mo	MCI-hGR + dexamethasone

The gene set could be separated into two major clusters, one that is defined by genes that are upregulated in H1Mo and H1Mo + MCI, and one that is defined by genes that are downregulated in H1Mo and H1Mo + MCI. This demonstrates that most of the transcriptional changes in H1Mo + MCI-hGR are driven by suv4-20h1 knockdown instead of MCI over-expression (Figure 3.28 A).

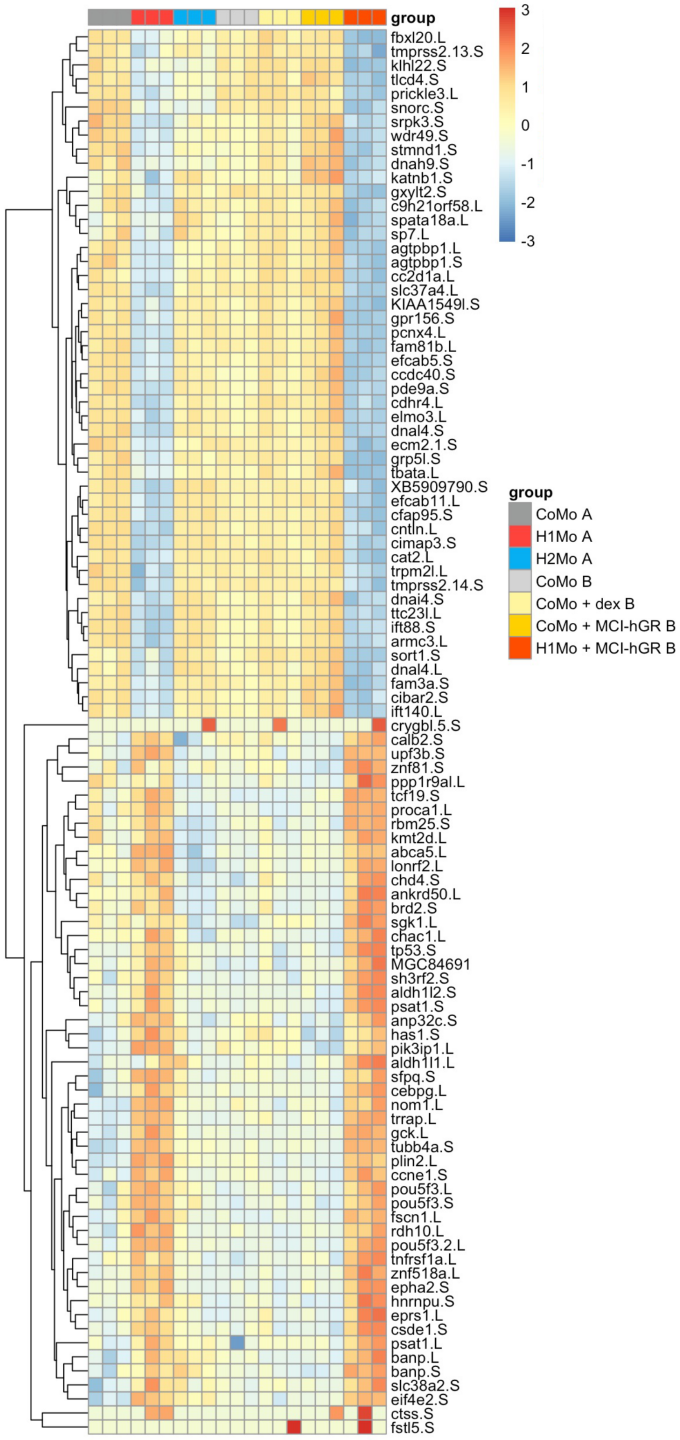

Figure 3.28: H1 knockdown drives transcriptional changes in MCI overexpressing animal caps. Combined analysis of RNA seq experiments in *Xenopus laevis* animal caps. Cluster analysis heatmap of top responding genes across all conditions. Genes group into two main clusters: genes downregulated or upregulated upon suv4-20h1 knockdown (in the absence or presence of MCI-hGR). Group A includes replicates from the single knockdown RNA seq experiment, and group B includes replicates from the MCI-hGR containing RNA seq experiment, and samples are batch corrected between experiments.

Additionally, we performed GO analysis on H1Mo + MCI-hGR injected animal caps. The upregulated genes contain categories related to mRNA processing and splicing and various metabolic processes (Figure 3.29 A). Once again, we see that ciliogenic categories dominate the downregulated GO terms in H1Mo + MCI injected animal caps (Figure 3.29 B). This is despite the fact that MCI overexpression leads to an upregulation of ciliogenic genes in CoMo injected animal caps, and that MCI-hGR increases the number of cells adopting a multiciliogenic fate. This, coupled with the phenotypic analysis, suggests that suv4-20h1 regulates multiciliogenesis either downstream of or through an alternative pathway to the typical MCI-initiated transcription factor cascade.

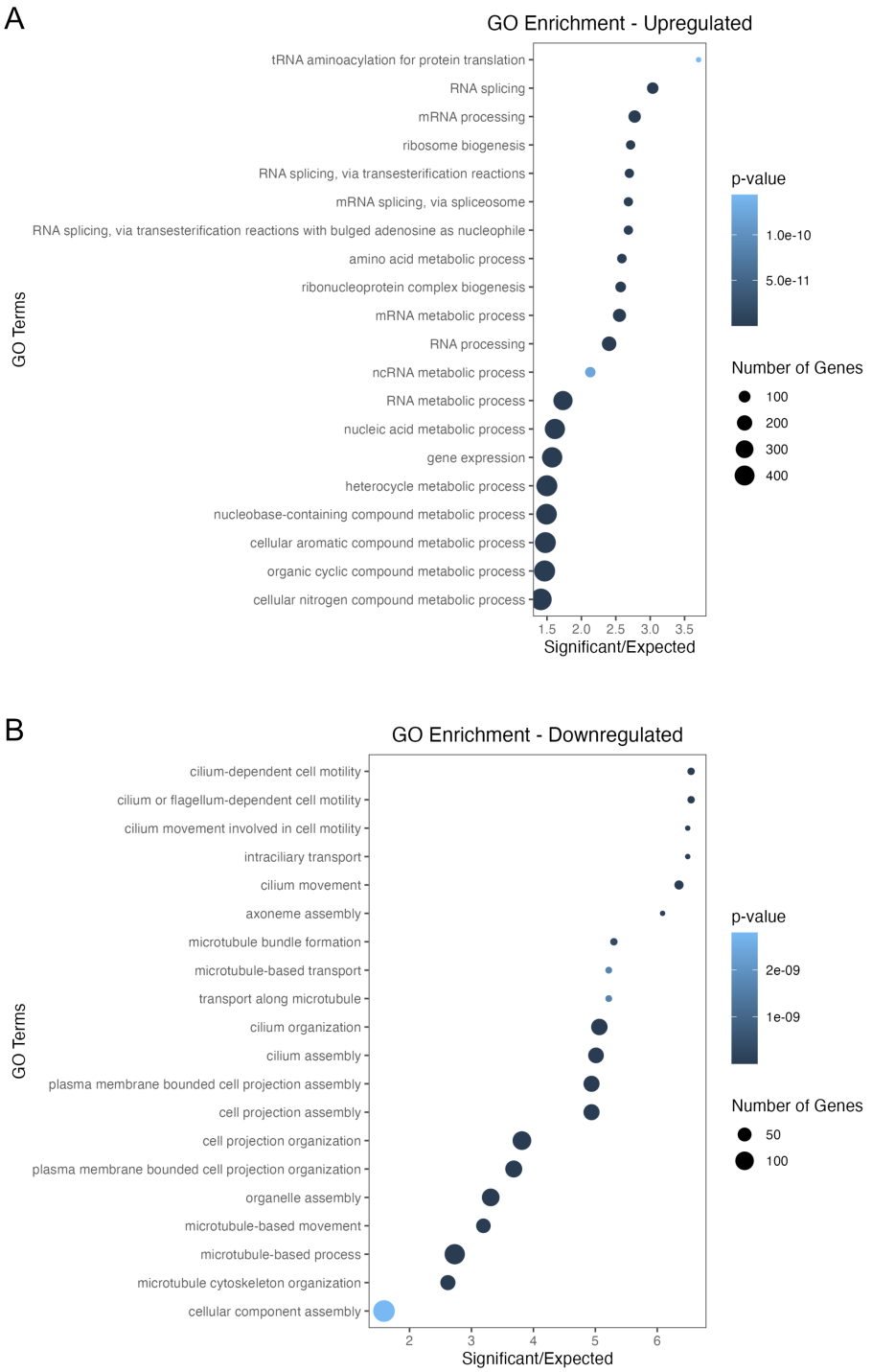

Figure 3.29: H1Mo + MCI-hGR injection still results in the downregulation of cilium-related GO terms. A, B) GO analysis for upregulated (A) and downregulated (B) genes in suv4-20h1 morpholino (H1Mo) + MCI-hGR injected animal caps compared to CoMo + MCI-hGR. Bubble size represents the number of significantly misregulated genes per GO term and bubble colous represents p-value. Upregulated GO terms are related to RNA processing and ribosome biogenesis, while downregulated GO terms are related to cilia and cell projection.

3.6 Mapping H4K20me1 by ChIP-seq

We were interested in determining whether the transcriptional effects of suv4-20h1 were due to an increase in H4K20me1 directly at cilia genes. In order to determine where novel H4K20me1 arose upon knockdown of suv4-20h1, we attempted to perform Chromatin Immunoprecipitation with sequencing (ChIP-seq) in *Xenopus laevis* animal caps. The planned experiment included 7 conditions (see Table 3.3) and would allow us to assess H4K20me1 localization in suv4-20h1/2 single and double knockdown animal caps, with MCI-hGR overexpression. As in the RNA-seq, for each replicate, we injected sibling embryos and performed ICC against acetylated alpha-tubulin to verify that both an MCI-hGR phenotype and a knockdown phenotype were present in the majority of embryos. In parallel, we optimized the ChIP-seq protocol, testing two previously published protocols[178,179] as published in [180], with and without nuclei extraction. Shearing was performed using a Bioruptor Pico (Diagenode) and optimized to generate fragment sizes of 250 bp. This resulted in a fixation time of 20 minutes in 1% PFA, followed by shearing for 10 cycles of 30 seconds on and 30 seconds off (Figure 3.30 A).

Table 3.3: ChIP-seq experimental conditions.

Morpholino	mRNA	Antibody
Wild-type	n/a	H3K27ac
Wild-type (200 animal caps)	n/a	H4K20me1
CoMo	n/a	H4K20me1
CoMo	MCI-hGR + dexamethasone	H4K20me1
H1Mo	MCI-hGR + dexamethasone	H4K20me1
H2Mo	MCI-hGR + dexamethasone	H4K20me1
H1H2Mo	MCI-hGR + dexamethasone	H4K20me1

We tested a ChIP-grade commercial antibody against H4K20me1 (ab9051, Abcam) and against H3K27ac (8173, Cell Signalling Technology) which have been successfully used for *Xenopus* ChIP before[179,180]. We observed a strong enrichment of target genes by ChIP-qPCR (Figure 3.30

B).

Despite these efforts, no enrichment was observed in the sequenced ChIP libraries over input (Figure 3.31). Sample collection for this experiment took over a year, and unfortunately, given the time required to generate, dissect, and phenotypically validate more than 600 animal caps per replicate, we decided not to continue with this experiment after receiving these negative results. ChIP-seq may have been unsuccessful in our hands for a number of reasons. We made two modifications to the protocol as seen in [180] (originally from[178]), the first was using a different library preparation kit (NEBNext Ultra II DNA library Prep Kit for Illumina (New England Biolabs) vs. TruSeq Library Prep Kit (Illumina)), as the original kit was discontinued. This could have led to a variable result. However, final TapeStation runs from the libraries prior to sequencing showed good yield and the expected size distributions. Additionally, we were able to map reads to the genome, indicating that the library preparation worked.

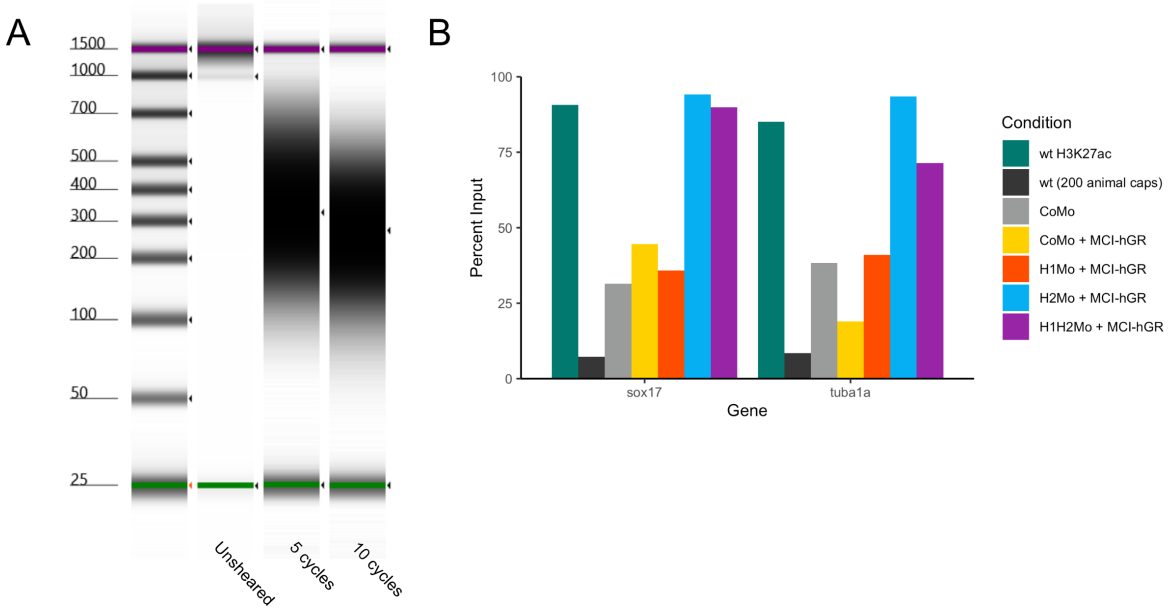

Figure 3.30: Optimization of ChIP-seq protocol A) Test of shearing conditions. We tested either 0, 5, or 10 cycles on a bioruptor (company). We aimed for an optimal fragment length of 250 bp. This was achieved with 10 cycles and a fixation time of xx in 1% PFA. Samples were run on a TapeStation (Agilent). Black triangles indicate peak sizes. B) ChIP-qPCR results showing percent input of H3K27ac and H4K20me1 at sox17 and tubba1a.

An additional possibility is that the antibody was not able to pull down any DNA. The antibody against H4K20me1 has not been validated for ChIP in *Xenopus*, but this H3K27ac antibody has

reliably been used before[59,60,180], so the antibody is unlikely to be the source of error. The protocol from [178] includes many wash steps. It is possible that the washing was too stringent, leading to loss of target DNA from the Dynabeads and the observed lack of enrichment. Enrichment of ChIP qPCR samples of target sequences could represent non-specific antibody binding or background, unbound DNA. Additionally, due to the technical constraints of working with microinjected and dissected animal caps, the amount of starting material was limited. We used 100 animal caps per replicate, while other ChIP protocols have recommended as many as 300 animal caps[181], which would not have been feasible given our experimental design. We did include a sample comprised of 200 animal caps in both the ChIP-qPCR and ChIP-seq, but the enrichment was not improved by the higher amount of starting material. Indeed, while ChIP-seq protocols for *Xenopus* animal caps have been published, this technique is not routine or widely performed in our model system. We cannot be certain why we were unable to observe enrichment after all of the standard controls and optimization steps appeared successful, but any or all of the problems mentioned above could have contributed. Recently, CUT&RUN protocols have been established for *Xenopus*, which would be worth attempting in the future to map H4K20me1 in suv4-20h1 knockdown animal caps[182].

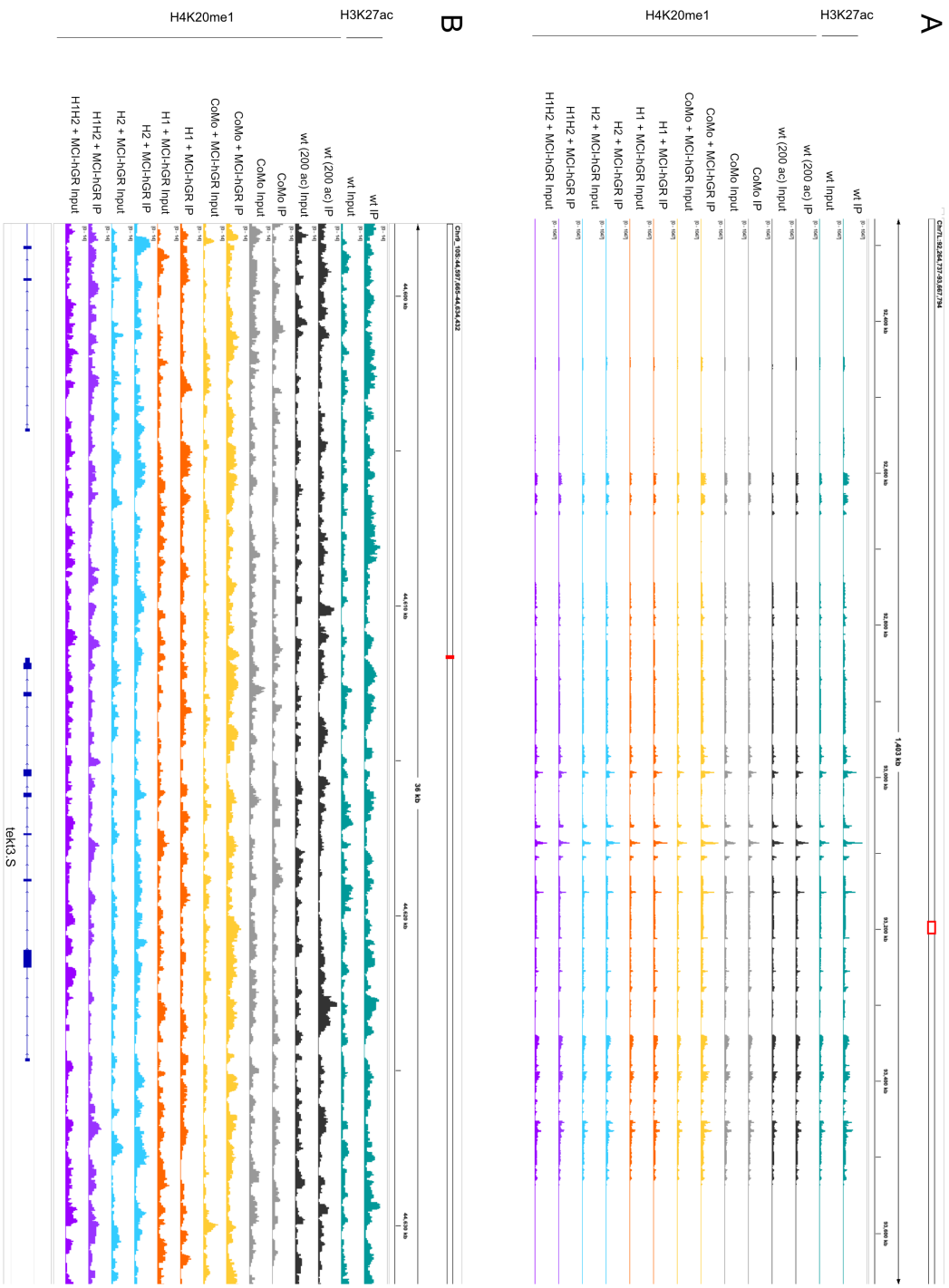

Figure 3.31: No enrichment of IP samples over input was observed. Browser profiles from H3K27ac and H4K20me1 ChIP seq. A) Overview of a 1045 kb segment of chromosome 7L shows highly similar profiles between both antibodies and all 7 conditions. There is little observable difference between input and ChIP samples. B) Browser profiles for a 36 kb genomic region encompassing tekt3.S, one of the most highly downregulated cilium genes from the H1 knockdown RNA-seq experiment. Again, little enrichment over input is observed.

3.7 Effect of suv4-20h1 knockdown on chromatin accessibility

Our results so far indicate that knockdown of suv4-20h1 results in dampened transcription, rather than silencing, of active genes, potentially through abberent conversion of H4K20me2 into H4K20me1. H4K20me1 function is thought to involve recruitment of reader proteins and/or compaction of chromatin[128,132]. The function of H4K20me1 in compaction may be carried out through its reader protein, L3MBTL1[135,136], or directly through interactions with the C terminus of H2A on neighboring histone tails[183]. Could the concentrated downregulation of ciliogenic genes and, as a consequence, the MCC phenotype be caused by a loss of chromatin accessibility at target genes? We decided to use ATAC-seq to address this question. ATAC-seq (Assay for Transposase-Accessible Chromatin using sequencing) is a technique that is used to profile chromatin accessibility. In this approach, a hyperactive Tn5 transposase cuts at accessible chromatin and binds adaptors to the cut sites, a process known as "tagmentation". Due to steric hindrance, the Tn5 only cuts in accessible regions, while less accessible regions are left intact. From there, tagged sequences can be mapped and accessibility can be assessed (Figure 3.32 A).

3.7.1 Optimization of Tn5 concentration

While ATAC-seq has previously been used in *Xenopus*[148], we still had to perform some optimization steps. Due to the high amount of yolk present in *Xenopus* embryos, the technique is limited to two animal caps per 50µl reaction. Before sequencing can be performed, it is necessary to verify that samples show a good nucleosomal banding pattern. However, using the previously established Tn5 concentration consistently led to samples being overtagmented. Because we were unable to increase the number of cells in our reaction, we decided to test different concentrations of transposase in order to optimize the transposase reaction and achieve the required nucleosomal banding pattern. The concentration of Illumina TDE1 enzyme is proprietary, so cannot be provided, but we performed a titration of TDE1 using 2.5 µl (100%), 1.9 µl (75%), 1.25 µl (50%), and 0.62 µl (25%) TDE1 in duplicate. Again, we saw that 100% TDE1 resulted in over-tagmented DNA, visible based on a large peak in the low size

range. On the other hand, 50 or 25% resulted in under-tagmented DNA (not shown). Using 75% TDE1 consistently resulted in an ideal nucleosomal banding pattern, and this was used for all downstream analyses (Figure 3.32 B, C).

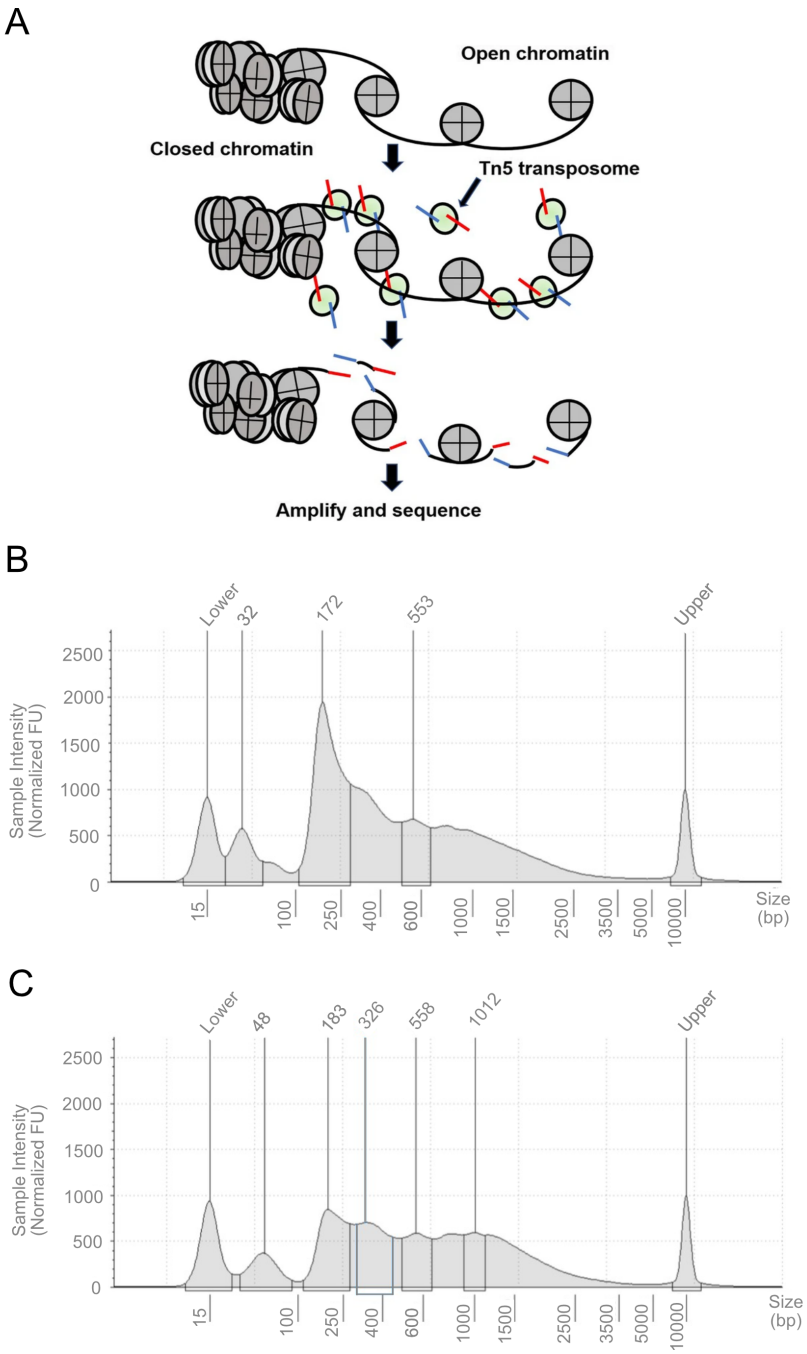

Figure 3.32: Optimization of ATAC seq protocol. A) Overview of ATAC seq protocol. Sample DNA is cut at accessible regions using Tn5 transposase, which inserts adapter sequences at these regions. DNA is amplified and sequenced to map chromatin accessibility. Adapted from [184] B, C) Tapestation traces depicting fragment size and sample intensity of ATAC seq libraries prior to bead-based size selection. Transposase amount was titrated to an optimal concentration for two *Xenopus laevis* animal caps B) 100% of recommended Tn5 transposase concentration (2.5 µl of Illumina Tagment DNA TDE1 Enzyme) leads to overtagmented DNA, which is evident from the large peak in the 100-200 bp range. C) 75% of recommended Tn5 transposase concentration (1.88 µl of Illumina Tagment DNA TDE1 Enzyme) consistently resulted in an ideal nucleosomal banding pattern, an indicator of high-quality libraries.

3.7.2 Suv4-20h1 increases chromatin accessibility

To determine the effect of suv4-20h1 knockdown on chromatin accessibility, we performed ATAC-seq in H1Mo and CoMo injected animal caps. We used 2 animal caps per condition in triplicate across three replicates, staged to NF16 according to sibling embryos. We identified 118 809 total peaks, comparable to other ATAC-seq results in *Xenopus*[148]. In total, 24604 (20.7%) are found at promoters, 1648 (1.4%) immediately downstream of the TSS, 1512 (1.3%) at the 5' UTRs, 996 (0.8%) at the 3' UTRs, 4489 (3.8%) in the exons, 42188 (36%) in the introns, and 43372 (36%) in the intergenic regions. Of these peaks, 556 are differentially accessible (Figure 3.33 A). Contrary to our expectations, most of the peaks increased in accessibility, while only 17 peaks became less accessible. Of the differentially accessible peaks, 44 (8%) at promoters, 6 (1.1%) immediately downstream of the TSS, 5 (0.9%) at the 5' UTRs, 2 (0.35%) at the 3' UTRs, 13 (2.3%) in the exons, 220 (39.5%) in the introns, and 265 (47.7%) in the intergenic regions (Figure 3.33 B). Overall, the effect is mild, with only approximately 0.5% of peaks changing in accessibility. This does not support the hypothesis that decreased accessibility due to an increase in H4K20me1 is the mechanism responsible for the ciliogenic phenotype.

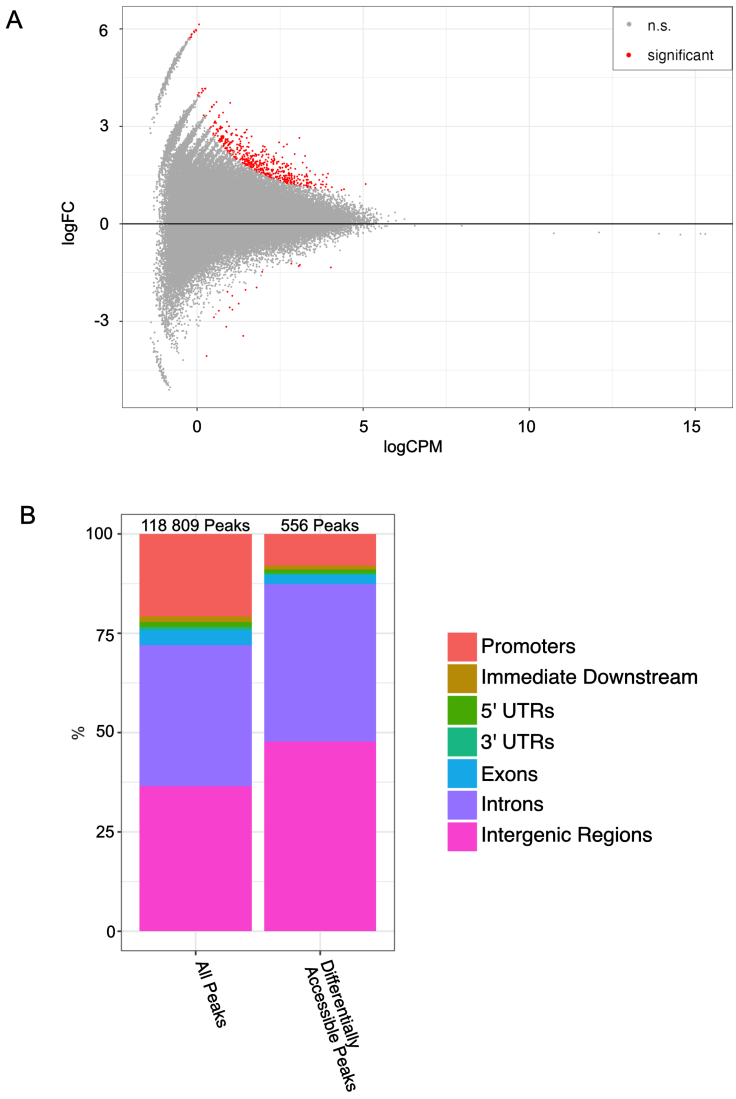

Figure 3.33: H1 knockdown leads to increased chromatin accessibility. A) MA plot showing differentially expressed peaks in H1 knockdown animal caps. Significantly changing peaks are shown in red ($p<0.05$). The majority of peaks are increasing rather than decreasing. This indicates a mild chromatin opening effect of H1 knockdown in *Xenopus laevis* animal caps. B) Distribution of peaks across genomic features. N = 3 biol. replicates.

4

DISCUSSION

In this thesis, we show that a single histone-modifying enzyme, suv4-20h1, is responsible for regulating multiciliogenesis. Multiciliated cells (MCCs) represent a terminally differentiated and highly specialized cell type and a key component of mucociliary epithelia. Making an MCC requires deploying a complex gene regulatory network and intricate cellular processes[102]. Over the years, our lab has detailed an unexpected link between this unique cell type and suv4-20h1, the enzyme that writes the monomethyl mark on histone 4 lysine 20. By extending this knowledge through the work presented in this thesis, I contribute five key novel insights:

1. Suv4-20h1 and suv4-20h2 independently influence H4K20 methylation state in *Xenopus*.
2. Suv4-20h1 knockdown alone is responsible for ciliogenic defects on the phenotypic and transcriptional level, and this relies on the enzyme's catalytic activity.
3. Catalytic activity of PHF8, an H4K20me1 demethylase, can rescue ciliogenic defects caused by suv4-20h1 knockdown.
4. Downregulation of ciliogenic genes is not caused by the repression of a ciliogenic regulator and cannot be rescued by overexpression of multicilin, the master regulator of multiciliogenesis.
5. Despite concerted downregulation of ciliogenic genes, suv4-20h1 knockdown leads to a mild increase in chromatin accessibility in *Xenopus* animal caps.

Our findings reveal an intriguing and specific interdependence between the epigenetic landscape and epidermal differentiation, but the exact mechanism remains undetermined. In the following discussion, I will present our current hypotheses regarding the regulatory role of suv4-20h1 in MCCs. These hypotheses draw on evidence linking both H4K20 methylation and multiciliogenesis to the cell cycle. We also take into account the possibility of histone-modifying enzymes targeting non-histone substrates. Additionally, we consider the distinct

chromatin states observed in post-mitotic cells and the involvement of H4K20 methylating enzymes in these processes, particularly in the context of development and disease.

4.1 Specificity of the phenotype

We demonstrate that this phenotype is specific through several orthologous methods. The ciliogenic phenotype can be generated by two non-overlapping antisense morpholinos[144]. This indicates that the ciliogenic defects are most likely not due to off-target effects of the morpholino but a genuine consequence of suv4-20h1 depletion. We show here that ciliogenesis can also be rescued by wild-type but not catalytically inactive suv4-20h1, indicating that the phenotype depends on the catalytic activity of suv4-20h1. This suggests that the methylation of some substrate, most likely conversion of H4K20me1 to H4K20me2, is required for cilia tuft assembly.

The double knockdown of the suv4-20h enzymes results in the loss of both H4K20 di- and trimethyl marks in the developing *Xenopus* embryo, which led us to propose two potential mechanisms for the observed ciliogenic phenotype. The first hypothesis is that the loss of the heterochromatic H4K20me3 mark could have caused the deregulation of a repressor of ciliogenesis, potentially suppressing the entire ciliogenic genetic program. Alternatively, given the substantial increase in H4K20me1 levels, we hypothesized that if H4K20me1 were responsible for the ciliogenic phenotype, we would expect cilia-related genes among those downregulated. Indeed, our analysis of the suv4-20h1/2 double knockdown dataset reveals that ciliogenic genes are downregulated in a coordinated manner.

Additionally, we show by mass spectrometry that while the phenotype relies on catalytic activity by suv4-20h1, this enzyme does not write the trimethyl mark in our system, ruling out the involvement of H4K20me3 in ciliogenesis. Although H4K20me3 has previously been shown to cause developmental phenotypes in the *Xenopus* embryo, including the derepression of oct-25, which causes neurodifferentiation defects through double knockdown of suv4-20h1/2[144], this does not appear to be the same mechanism regulating ciliogenesis. Taken together, this data supports the hypothesis that the substantial increase in H4K20me1 may be the primary

cause of the observed defects.

4.2 Demethylation of H4K20me1 partially alleviates the ciliogenic defects

To test this hypothesis further, we performed rescue experiments with the H4K20me1 demethylase, PHF8. PHF8 (PHD Finger-containing protein 8) is a Jumonji C Domain (JmjC)-Containing histone demethylase that is targeted to promoters by its PHD finger, which binds H3K4me3 and allows the JmjC domain to execute its catalytic function[129,130]. In zebrafish, PHF8 knockdown is required for proper craniofacial development and neurite outgrowth[130]. It is also involved in regulating cell cycle progression[129]. The combination of PHF8 as a cell cycle regulator, involved in developing ectodermal and cytoskeletal elements like the jaw and the neurons, makes it an intriguing candidate to have a function in ciliogenesis. We hypothesized that if the ciliogenic phenotype were caused by the increase in H4K20me1, removing some of the methyl marks with PHF8 would rescue the phenotype.

We observed that PHF8 improves cilia condition in the majority of knockdown MCCs. In addition, PHF8 can restore the actin cap, while injection of a control mRNA did not rescue. On the transcriptomic level, downregulated genes are not perfectly rescued, but most of the genes move back toward normal expression levels, so we consider their expression to be improved. Overall, PHF8 ameliorates the ciliogenic defect on the phenotypic and transcriptional levels. However, we also looked at the effect of PHF8 on H4K20 methylation levels and did not see a change in methylation state abundance in bulk chromatin for H4K20me1 or its additional targets, H3K9me1/2. SET8 writes H4K20me1 indiscriminately across the genome, while PHF8 only demethylates a smaller set of promoters. This may indicate a local change to H4K20me1 that is not detectable on bulk chromatin, in line with a previous study in zebrafish that showed only a small decrease in H4K20me1 at PHF8 target loci upon depletion[130].

4.3 Only suv4-20h1 is required for ciliogenesis

One of our most striking findings is that suv4-20h1 alone is responsible for the transcriptional changes underlying the ciliogenic phenotype. Knockdown of suv4-20h1 leads to the misregulation of hundreds of genes, with a concerted downregulation of ciliogenic genes, while suv4-20h2 barely affects transcription, and the misregulated genes do not show a ciliogenic connotation. On the phenotypic level, dramatic ciliogenic defects are caused by suv4-20h1 knockdown, while suv4-20h2 alone apparently does not affect MCCs.

Double knockdown of suv4-20h1/2 leads to a global shift of the H4K20 methyl landscape towards H4K20me1. Over 60% of all H4K20 becomes monomethylated, from an initial level of approximately 20% in wild-type embryos. From the literature, we expected that suv4-20h1 was responsible for writing the dimethyl mark, while suv4-20h2 was responsible for writing the trimethyl mark, as in MEFs[127]. However, mass spectrometry revealed that suv4-20h1 and suv4-20h2 contribute similarly to writing the dimethyl mark. So, we have two enzymes that are similar in structure and substrate specificity, converting H4K20me1 into H4K20me2. However, one of these enzymes strongly affects transcription and multiciliogenesis, and the other does not.

We asked ourselves how we might see such an apparently specific effect on cilia when the impact on H4K20me1 is so broad and appears to be similar between suv4-20h1 and suv4-20h2. Could a major multiciliogenic regulator be misregulated by suv4-20h1, causing the downstream effects on ciliogenesis and transcription? We checked the changes in transcription of known ciliogenic regulators upon suv4-20h1 knockdown, including MCI and foxj1, the master regulators of multiciliogenesis. None of the known critical ciliogenic regulators were significantly downregulated in our suv4-20h1 knockdown dataset. E2F proteins, some of which have been shown to play roles in regulating ciliogenesis[116], are also not significantly affected by suv4-20h1 knockdown, except E2F1, which has not been shown to have a specific role in ciliogenesis. Thus, our ciliogenic phenotype is not likely due to repression of a ciliogenic regulator. What additional differences between these two enzymes could account for the divergence of function we observe in MCCs?

4.3.1 Structural differences between suv4-20h1 and suv4-20h2

Suv4-20h1 and suv4-20h2 are structurally similar enzymes. They have similar domain architecture, with an N-terminal helical domain and a post-SET domain[141]. Their catalytic domains also share high sequence homology. However, suv4-20h2 is stably associated with pericentric heterochromatin through its interactions with HP1, while suv4-20h1 does not share the same association[185]. It could be that stable interaction with HP1 sequesters suv4-20h2 to heterochromatic portions of the genome, where it would catalyze the conversion of SET8-dependent H4K20me1 to both H4K20me2 and H4K20me3 states. While this mechanism would not hinder suv4-20h1 from reaching heterochromatin, it may be primarily active in euchromatic regions due to its higher structural accessibility. Thus, suv4-20h1 and suv4-20h2 functions would be segregated between eu- and heterochromatin, respectively, which could explain their strikingly different impact on gene transcription. This hypothesis would be worth exploring further, ideally using antibodies or knock-in strategies to tag the two enzymes. Additionally, mapping of novel H4K20me1 peaks by CUT&RUN would inform whether partitioning of genomic regions between the two enzymes plays a role in this phenotype.

4.3.2 Functional differences between suv4-20h1 and suv4-20h2

Multiciliogenesis is not the only process in which functional differences between suv4-20h1 and suv4-20h2 have been reported. In mice, suv4-20h1 knockdown causes perinatal lethality, while suv4-20h2 knockdown mice develop normally[127]. This could be due to the overall lower expression of suv4-20h2 in mouse embryos compared to the widespread expression of suv4-20h1. Suv4-20h1 also has an independent function in neurogenic disorders. It is a key Autism spectrum disorder risk gene, with certain *de novo* patient mutations leading to neurodevelopmental disorders[186]. On the other hand, the same study found that *de novo* mutations to suv4-20h2 were not associated with disease phenotypes. Similarly, *de novo* mutations to suv4-20h1 have been identified to play a role in congenital heart disease[187]. Suv4-20h1 also plays a unique role in regulating muscle satellite cell differentiation, likely through the maintenance of heterochromatic H4K20me3. In this system, suv4-20h1 and suv4-20h2 seem to have opposing roles with regard to proliferation, with suv4-20h1 depletion leading to an

increase in proliferating satellite cells, and suv4-20h2 leading to a decrease in proliferation[188]. Here, we report an additional unique function for suv4-20h1 in multiciliogenesis. Suv4-20h1, but not suv4-20h2 depletion, leads to defects in the cilia and apical actin meshwork of affected MCCS and significant downregulation of ciliogenic genes.

4.3.3 Non-histone substrates of H4K20 methylating enzymes

Recently, additional substrates for histone methylating enzymes have been identified, and we asked whether this could explain our phenotype. For example, CTNNBL1 was shown to be methylated by PRDM9[189], and SET8 has been shown to methylate α-tubulin[190]. Even suv4-20h1 has been shown to methylate non-histone substrates, including CASZ, a zinc finger transcription factor, and OSBPL1A, a protein that transports oxidized sterols[191]. It has also recently been shown that suv4-20h1 is found in the nucleus in interphase cells but relocates to the mitotic spindle in metaphase of mitotic cells[192]. Our lab has previously imaged flag-tagged suv4-20h1 in the *Xenopus* epidermis and found that it localizes to the nucleus but not to the cilia, so we do not expect that suv4-20h1 is directly methylating tubulin[145]. Additionally, wild-type but not catalytically inactive suv4-20h1 can rescue these phenotypes. Our phenotype is dependent, at least in part, on the catalytic activity of suv4-20h1. Nevertheless, we cannot exclude the possibility that suv4-20h1 exerts its function in ciliogenesis through methylation of a nuclear non-histone substrate.

Additionally, several factors could influence suv4-20h1 localization. Facioscapulohumeral muscular dystrophy gene, FRG1, is a binding partner of suv4-20h1 and is ubiquitously expressed, including in the MCCs of the mammalian bronchi. Direct binding by FRG1 leads to mislocalization of suv4-20h1 and a subsequent derepression of Eid3, a muscle differentiation gene[193]. FRG1 is also critical for *Xenopus* muscular development[194,195]. This example demonstrates a mechanism by which binding proteins may disrupt suv4-20h1 localization, withdrawing it from its epigenetic targets.

4.4 H4K20 methylation and the cell cycle

H4K20 methylation is highly connected to the cell cycle. The mark is written in a cell cycle-dependent manner, meaning that H4K20 methylation levels fluctuate with the cell cycle phase (see Figure 1.9). In cycling cells, H4K20me1 is written by SET8 from late S-phase, through mitosis until late in G1-phase when SET8 is degraded[121]. Then, the suv4-20h1/2 can write the higher methylated states[128]. PHF8 is phosphorylated by mitotic kinases, causing release from chromatin, which probably contributes to the increase in H4K20me1 levels during mitosis[129]. Could this cell cycle connection provide insight into the molecular basis of the ciliogenic phenotype?

4.4.1 Cellular machinery is shared by cilia and the cell cycle

The cellular machinery required to make cilia comprises proteins like tubulins, actin, and centriolar proteins. Basal bodies themselves are modified centrioles. These proteins are critical for cell cycle progression. Because of this, MCCs are not compatible with mitosis. Structures that make up MCCs, such as cilia and multiple centrioles, would be harmful to the formation of the mitotic spindle, and mitosis would be unlikely to progress normally. We postulate that H4K20me1 safeguards the process of mitosis by repressing ciliogenic and cytoskeletal genes *en masse*.

Ciliogenesis and the cell cycle are closely interconnected. Primary cilia formation is believed to be a key regulator of cell cycle progression and timing. Primary cilia may regulate the cell cycle through various mechanisms, such as controlling the duration of the G1-phase based on cilia length after cell cycle re-entry or acting as a brake to cell cycle progression. Forced ciliogenesis, for instance, arrests the cell cycle at the G1/S transition[159,196]. One of the most mis-regulated genes in our dataset upon suv4-20h1 knockdown is IFT88, an intraflagellar transport protein involved in transporting materials from the base to the tip of the cilia[197–199]. It plays roles not only in ciliogenesis but also in the cell cycle, having been shown to regulate the G1/S transition in non-ciliated cells[200]. Knockdown of IFT88 leads to shorter cilia, but it can also rescue defects in ciliogenesis and the cell cycle caused by the depletion of NDE1, a negative

regulator of ciliary length—Knockout of NDE1 results in abnormally long cilia and delayed cell cycle re-entry. However, further knockout of IFT88 restores the length of NDE1-depleted cilia to normal, likely by shifting transport equilibrium from growth-favouring anteretrograde transport towards disassembly-favouring retrograde transport. IFT88 knockdown also reverses the delays in cell cycle re-entry caused by NDE1 knockout[159]. IFT88 represents an interesting candidate gene for further study due to its strong downregulation in our dataset and its roles in ciliogenesis and the G1/S transition.

We also see connotations related to the cell cycle in the upregulated gene category of our suv4-20h1 knockdown RNA-seq, including GO terms such as "mitotic cell cycle", "microtubule cytoskeleton involved in mitosis", and "cell division". Here, we see cells sitting in the G0-phase but with the H4K20 methylation levels of a cell preparing for mitosis. Even the pathway that controls the differentiation of MCCs is regulated by the mitotic oscillator[105]. Cdk1, APC/C, and PlK1 control entry and exit into mitosis, and at an attenuated level, they are also responsible for regulating the entry and exit of the growth phase of basal body duplication during multiciliogenesis. As a reminder, centriole duplication occurs in three distinct phases. The first is the amplification phase, in which the centrioles are duplicated through the centriole-dependent and independent pathways, either from the mother centriole or the deuterosome. Next, the centrioles leave the amplification phase and enter the growth phase, increasing in size. Lastly, they enter the disengagement phase, where they are released from the deuterosome and migrate towards the apical surface of the cell[102]. When cdk1 or plk1 are inhibited, too many centrioles are formed. When cdk1 is hyperactivated, too few centrioles are formed, and when APC/C is inhibited, the basal bodies fail to disengage and dock to the apical surface[105]. Centriole disengagement and cilia formation are perturbed in our MCCs, and this could be due to the involvement of the mitotic oscillator.

4.4.2 H4K20 methylation and quiescence

The connection between H4K20 methylation and the cell cycle is clear, but H4K20 methylation levels in post-mitotic cells differ from those in proliferating cells. H4K20me1 levels fluctuate the most throughout the cell cycle of any H4K20 methylation state[128]. Peak H4K20me1 levels

are reached at the G1/S transition just before SET8 becomes degraded. In quiescent cells, H4K20me1 is very low. This prompted the idea that our MCCs may represent a compromised state of quiescence. The differentiated and post-mitotic state of MCCs is similar to a state of cellular quiescence, so we might expect H4K20me1 levels to be similar to those of quiescent cells. This also parallels findings from our lab based on mathematical modeling in cell cycle-arrested embryos[201]. Embryos treated with the S-phase inhibitor hydroxyurea (HUA) hyper-accumulate H4K20 di- and trimethyl marks. In a cycling embryo, higher methylation levels are kept in check by S-phase dilution. In the absence of the cell cycle, demethylation is required to maintain normal H4K20 methylation kinetics. Interestingly, mathematical modeling predicts that embryos with a blocked cell cycle require active demethylation to explain the measured H4K20me2 and me3 levels, while S-phase dilution is sufficient to maintain the ratio of the H4K20 methylation states in normal proliferating embryos without a cell cycle block. When MCC precursors become post-mitotic, these proposed mechanisms would ensure a chromatin landscape in which the H4K20me1 levels are compatible with cilia tuft assembly. In suv4-20h1 morphant embryos, however, the abnormally high abundance of H4K20me1 seems to interfere with this process. This hypothesis is consistent with the rescue of the ciliogenic phenotype by coexpression of enzymatically active suv4-20h1 or PHF8, which either remove or convert H4K20me1 out of the chromatin landscape. Indeed, this study highlights the importance of demethylases like PHF8 in regulating the methylation landscape in the chromatin of differentiating, post-mitotic cells.

4.5 Regulation of post-mitotic cells by suv4-20h1

Here, we demonstrate how suv4-20h1 regulates MCCs, a post-mitotic cell type. The link between H4K20 methylation and MCCs would not have been possible to identify in a different model organism. *Xenopus* MCCs are located on the surface of the embryo, making them easy to observe and image. Many of the previous studies on H4K20 methylation have been performed in cycling cells[126,132,202]. Indeed, a complex and easily manipulable model system such as *Xenopus* embryos in their natural course of development provide the opportunity to observe such striking and possibly clinically relevant phenotypes. Simple systems such as

cell culture of immortalized cell lines are much more limited in their response repertoire. Systems like *Xenopus* draw attention to an underexplored field in epigenetics: the control of transcriptional circuitries in non-proliferating cells.

However, MCCs are not the only post-mitotic cell type regulated by suv4-20h1. Recently, suv4-20h1 has been shown to play a role in the apoptosis pathway in post-mitotic neurons of the amygdala and cerebellum through Rb1 binding[203]. The binding of suv4-20h1 by Rb1 leads to the activation of Caspase/Bcl2. Rb1 knockout or deficient patient mutations of Rb1 result in inappropriate apoptosis in hindbrain neurons, and these defects can be partially rescued by overexpression of suv4-20h1[203].

Many of the unique functions of suv4-20h1 highlighted in section 1.4.1 involve specialized post-mitotic cell types. As previously mentioned, suv4-20h1 is required to maintain quiescence in muscle satellite cells. Depletion of suv4-20h1 in satellite cells leads to an increase in proliferating cells, while suv4-20h2 depletion inhibits proliferation. Consistent with our data, this study finds that suv4-20h1 depletion decreases H4K20me2, with a concomitant increase in H4K20me1 and no difference in H4K20me3. This suggests the H4K20me1 promotes proliferation relative to H4K20me2/3 and demonstrates a unique function for suv4-20h1 in regulating the quiescence of satellite cells[188].

4.6 An alternative pathway for regulating multiciliogenesis?

Our lab previously demonstrated that the suv4-20h1/2 knockdown phenotype could not be rescued by multicilin (mci) overexpression[145]. Mci is the master regulator of ciliogenesis[116] and is sufficient to convert goblet cells to an MCC-like fate. Berges [145] observed that in “new” MCCs, even though cilia are not present, these cells still undergo basal body multiplication. This indicates that the cells are converted to an MCC-like fate but lack cilia. We wanted to harness this effect to drive more cells in the animal cap to become multiciliated and overcome the relatively low proportion of MCCs.

Overexpression of mci led to a higher proportion of cells becoming multiciliated and a

significant upregulation of ciliogenic genes. Even in suv4-20h1 knockdown embryos, it was evident, based on the multiplication of basal bodies, that most injected cells had adopted a multiciliogenic fate. However, injected cells lacked cilia in suv4-20h1 knockdown, mci overexpressing embryos, and ciliogenic genes were still significantly downregulated. These transcriptional changes were almost entirely driven by suv4-20h1 knockdown and not by mci overexpression, even though mci overexpression results in a dramatic remodeling of the *Xenopus* embryonic epidermis and downstream regulators of the ciliogenic pathway are not affected and cannot rescue the ciliogenic phenotype. This argues that suv4-20h1 regulates ciliogenesis through an alternative pathway to the canonical multiciliogenesis signal cascade.

4.7 Histone modifications and chromatin accessibility

Histone modifications have been broadly shown to affect chromatin architecture and accessibility. Acetyl marks, for example, directly influence chromatin accessibility by reducing the charge of the histone tail, changing its electrostatic interactions with DNA[32]. Lysine methylation can indirectly lead to changes in accessibility by recruitment of reader proteins. H4K20me1 has varying effects on chromatin accessibility. This modification has been shown to orchestrate transcriptional repression through one of its reader proteins, L3MBTL1, which directly contributes to chromatin compaction[135,136]. Due to this connection, we hypothesized that the expression of ciliogenic genes might be downregulated, at least partially, through transcriptional repression linked to changes in chromatin accessibility. On the other hand, H4K20me1 is also linked to chromatin openness by decorating the gene bodies of active genes, and it is correlated to transcription of highly transcribed housekeeping genes[132]. Once again, the function and connotation of H4K20me1 regarding chromatin accessibility remain ambiguous.

Still, it is clear that H4K20me1 is connected to changes in chromatin accessibility, which could be a contributing mechanism to the ciliogenic phenotype. ATAC-seq profiling of suv4-20h1 knockdown animal caps showed a mild opening effect on the chromatin, with few differentially accessible peaks, most of which were increasing in accessibility. This result is consistent with data linking H4K20me1 with chromatin openness[132]. However, most differentially ac-

cessible peaks are found in intergenic or intronic regions, and very few can be mapped to genes. If accessibility were playing a strong role in the ciliogenic phenotype, we would have expected a decrease in accessibility at the regulatory regions of ciliogenic genes. Instead, we see a mild opening of the chromatin. It could be that accessibility is increased at a gene with a negative impact on ciliogenesis. For example, one of the genes with increased accessibility is foxi1, a key transcription factor in ionocyte differentiation[204]. However, we do not see a change in the expression of foxi1 by RNA-seq or a decrease in multiciliated cell number, so this seems unlikely. Overall, the role of suv4-20h1 in multiciliogenesis does not seem to be operating through alterating chromatin accessibility.

4.8 A critical function for suv4-20h1 in multiciliogenesis

This study clearly demonstrates a function for suv4-20h1 in multiciliogenesis. We have shown that this phenotype is specific through rescue with wild-type and catalytically inactive suv4-20h1. We also show a sizeable underlying shift in H4K20 methyl abundance upon single knockdown of suv4-20h enzymes. Here, we propose a model to link suv4-20h1 and multiciliogenesis (Figure 4.1). In wild-type cells, suv4-20h1 is present and capable of writing H4K20me2, a transcriptionally neutral mark, allowing regular transcription of genes related to ciliogenesis and cytoskeleton. In turn, a normal multiciliated cell with full-length cilia, regularly spaced basal bodies, and an intact actin cap is formed. When we knock down suv4-20h1, H4K20me2 cannot be written. Concurrently, the suv4-20h1 depleted chromatin accumulates H4K20me1, potentially leading to a downregulation of cytoskeleton and cilia genes and ultimately to our multifaceted ciliogenic phenotype.

However, the precise mechanism by which suv4-20h1 regulates MCCs remains elusive. In this discussion, we have speculated on a few potential mechanisms that I will summarize here. Dimethylation of H4K20 by suv4-20h1 could be required directly at ciliogenic genes to allow ciliogenesis. This could be demonstrated through mapping of H4K20me1 in the presence or absence of suv4-20h1 by CUT&RUN. If novel H4K20me1 peaks appear at the regulatory regions of downregulated ciliogenic genes, we could demonstrate that H4K20me1 has a broad negative transcriptional effect on multiciliogenesis. Alternatively, even though none of the

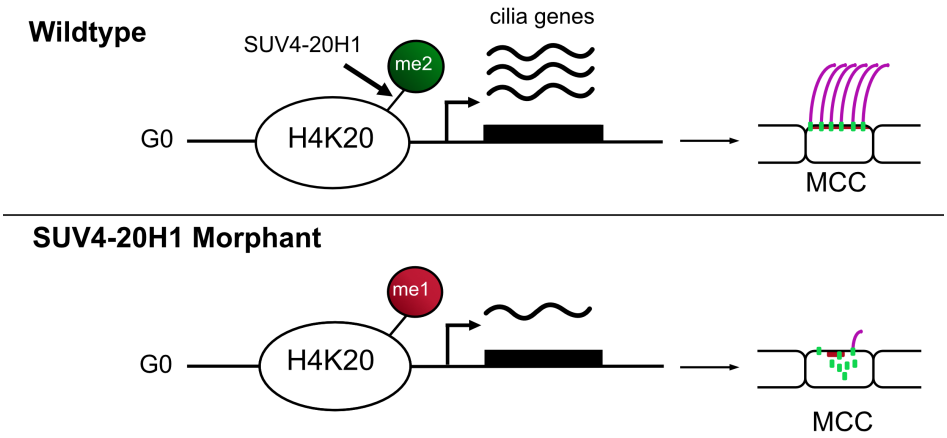

Figure 4.1: A model for the regulation of ciliogenesis by suv4-20h1. Adapted and reprinted with permission from Life Science Alliance (Angerilli, Tait, *et al.*[151]).

known ciliogenic regulators were misregulated in our RNA-seq dataset, it could be that a yet undiscovered ciliogenic transcription factor is misregulated, leading to a downstream mass misregulation of ciliogenic genes and the multiciliogenesis program. Along these lines, it could be that a repressor of ciliogenesis became derepressed by suv4-20h1, potentially through increased chromatin accessibility, and that this repressor is executing the transcriptional regulation. However, we have not identified potential candidates in the RNA-seq or ATAC-seq datasets. Very recent work has shown that in *Drosophila* H4K20 reader and writer proteins, L3MBTL1 and SET8 execute their transcriptional functions independent of H4K20 methylation[205]. This could also hold true for suv4-20h1 and PHF8. We have shown that the catalytic activity of these enzymes is required for ciliogenesis, but they could be regulating multiciliogenesis through the methylation of a different, unknown target.

This raises the additional question of whether it is possible to fully decode the significance of a histone modification by functional analysis of its writers and erasers. Historically, much of the knowledge we have gained on the functions of histone modifications has come from either knocking out its modifying enzymes or, in amenable species, by mutating the histone residues themselves[206,207]. While these strategies have been highly informative, they are complicated by several factors. Many histone-modifying enzymes have non-histone substrates and non-catalytic functions, making it difficult to ascribe a direct role to a modification in phenotypes caused by manipulating histone-modifying enzymes. Further, the roles of modifications

may be context- or location-dependent and may be due to the recruitment of other proteins to the modification site. Measures like catalytically inactive rescue experiments address the problem of non-catalytic functions of the enzyme, and recently engineered chromatin readers have emerged as a way to edit the epigenome in a targeted manner without the added complication of additional functions or recruitment of other proteins[208,209]. However, neither of these methods addresses the issue of non-histone substrates of histone-methylating enzymes. It will be interesting to see how these technical limitations are overcome in the future.

4.9 Implications for development and disease

Our findings have several implications for development and disease. Defective cilia and mucociliary epithelia are both linked to pathologies. Mucociliary epithelia are key components of the respiratory system. Failures in ciliogenesis, or other aspects of the formation of mucociliary epithelia, are implicated in respiratory illnesses, including primary ciliopathies. In our double knockdown RNA-seq dataset, all genes related to Bardet-Biedl syndrome, an autosomal recessive ciliopathy that affects multiple systems, are downregulated. This study could provide insight into the molecular mechanism underlying Bardet-Biedl syndrome.

As mentioned above, *de novo* mutations to suv4-20h1 have been linked to congenital heart disease, with a subset of these patients exhibiting heterotaxy[187]. Indeed, we find that CFAP45, a gene associated with heterotaxy and congenital heart disease, is significantly misregulated in suv4-20h1 knockdown animal caps. This gene has been shown to affect cilia stability in both monociliated cells and MCCs in *Xenopus*[210]. CFAP45-depleted MCCs show reduced cilia that resemble the phenotype we observe in suv4-20h1-depleted MCCs. This could represent a mechanism by which suv4-20h1 is implicated in congenital heart disease through its function in cilia, which our lab identified.

Additionally, our study may have implications for neurological disorders like autism spectrum disorder and X-linked intellectual disability. Suv4-20h1 has been identified in several studies as one of the critical autism risk genes. Loss of suv4-20h1 in the prefrontal cortex leads to some

of the core autism phenotypes[211]. Chromatin regulators are implicated in Autism spectrum disorder, potentially through generating synapse defects[192]. Additionally, mutations to PHF8 have been linked to X-linked intellectual disability[140]. Suv4-20h1 has a proposed role as a tumor suppressor, and mutations to suv4-20h1 are also linked to several types of cancer, including AML, glioblastoma multiforme, and breast cancer[141,212]. In the future, H4K20-methylating enzymes could represent exciting candidates for drug development.

4.10 Future directions

This data has prompted a number of intriguing questions that could be examined in subsequent studies. Mapping H4K20me1 by CUT&RUN could determine whether the misregulated genes are direct targets of suv4-20h1 and may elucidate whether *de novo* H4K20me1 is responsible for the observed transcriptional misregulation. H4K20 demethylases have also emerged as important regulators of the epigenetic landscape. It would be interesting to profile the role of PHF8 in multiciliogenesis and *Xenopus* development in-depth. Extensive phenotypic analysis of the other H4K20 demethylases, RSBN1 and hHR23b, could give us a more comprehensive picture of the role of H4K20 methylation in development and could provide a tunable "molecular toolbox" to modify H4K20 methylation levels through combinatorial overexpression and depletion of methylating and demethylating enzymes. Alternatively, to address the possibility of suv4-20h1 and PHF8 acting on non-histone substrates, future studies could focus on defining the interactome of these enzymes by performing ChIP-Mass Spectrometry in cell cycle-synchronized cells.

MCCs are highly visible and specialized, so it makes sense that we would readily detect this defect in this cell type. However, MCCs are not the only highly specialized, post-mitotic cell type with cytoskeletal outgrowths. It would be interesting to investigate whether other cell types are similarly affected by suv4-20h1 depletion during embryonic development. Of particular interest would be studying the effect on neurons. This would give us more information about whether this effect is specific to MCCs or may apply more globally to terminally differentiated cell types.

4.11 Conclusion

This work shows that a single histone modifying enzyme, suv4-20h1, regulates multiciliogenesis in *Xenopus* embryos. Knockdown of suv4-20h1 leads to a global shift in H4K20 methylation abundances, a striking ciliogenic phenotype, and the downregulation of hundreds of ciliogenic and cytoskeletal genes. This phenotype is specific and relies on the catalytic activity of suv4-20h1 and can be partially rescued by enzymatically active PHF8, an H4K20me1 demethylase. The ciliogenic phenotype may be linked to the cell cycle and represents a novel function for suv4-20h1 in post-mitotic cells. This work has substantial implications for the fields of epigenetics and cell biology. Furthermore, perturbation of either suv4-20h1 or MCCs can result in respiratory illness, neurodevelopmental disorders, and congenital heart disease. These results could shed light on the biological processes underpinning these prominent clinical phenotypes.

Bibliography

1. Berger, S. L., Kouzarides, T., Shiekhattar, R. & Shilatifard, A. An operational definition of epigenetics. *Genes & Development* **23,** 781–783 (2009).

2. Probst, A. V., Dunleavy, E. & Almouzni, G. Epigenetic inheritance during the cell cycle. *Nature Reviews Molecular Cell Biology* **10,** 192–206 (2009).

3. Scharf, A. N. & Imhof, A. Every methyl counts – Epigenetic calculus. *FEBS Letters* **585,** 2001–2007 (2011).

4. Ross, D. W. The human genome: information content and structure. *Hospital Practice (1995)* **34,** 49–54, 56–60, 65 (1999).

5. Kornberg, R. D. Chromatin structure: a repeating unit of histones and DNA. *Science* **184,** 868–871 (1974).

6. Luger, K., Mäder, A. W., Richmond, R. K., Sargent, D. F. & Richmond, T. J. Crystal structure of the nucleosome core particle at 2.8 Å resolution. *Nature* **389,** 251–260 (1997).

7. Bowman, G. D. & Poirier, M. G. Post-Translational Modifications of Histones That Influence Nucleosome Dynamics. *Chemical Reviews* **115,** 2274–2295 (2015).

8. Mishra, L. N., Thiriet, C. & Vasudevan, D. Editorial: Chromatin structure and function. *Frontiers in Genetics* **14** (2023).

9. Bednar, J., Horowitz, R. A., Grigoryev, S. A., Carruthers, L. M., Hansen, J. C., Koster, A. J., *et al.* Nucleosomes, linker DNA, and linker histone form a unique structural motif that directs the higher-order folding and compaction of chromatin. *Proceedings of the National Academy of Sciences of the United States of America* **95,** 14173–14178 (1998).

10. Li, G. & Reinberg, D. Chromatin higher-order structures and gene regulation. *Current Opinion in Genetics & Development* **21,** 175–186 (2011).

11. Becker, P. B. & Workman, J. L. Nucleosome Remodeling and Epigenetics. *Cold Spring Harbor Perspectives in Biology* **5,** a017905 (2013).

12. Jenuwein, T. & Allis, C. D. Translating the histone code. *Science* **293,** 1074–80 (2001).

13. Saksouk, N., Simboeck, E. & Déjardin, J. Constitutive heterochromatin formation and transcription in mammals. *Epigenetics & Chromatin* **8,** 3 (2015).

14. Olins, D. E. & Olins, A. L. Chromatin history: our view from the bridge. *Nature Reviews Molecular Cell Biology* **4,** 809–814 (2003).

15. Venkatesh, S., Smolle, M., Li, H., Gogol, M. M., Saint, M., Kumar, S., *et al.* Set2 methylation of histone H3 lysine 36 suppresses histone exchange on transcribed genes. *Nature* **489,** 452–455 (2012).

16. Venkatesh, S. & Workman, J. L. Histone exchange, chromatin structure and the regulation of transcription. *Nature Reviews. Molecular Cell Biology* **16,** 178–189 (2015).

17. Jin, C., Zang, C., Wei, G., Cui, K., Peng, W., Zhao, K., *et al.* H3.3/H2A.Z double variant-containing nucleosomes mark 'nucleosome-free regions' of active promoters and other regulatory regions. *Nature Genetics* **41,** 941–945 (2009).

18. Morrison, O. & Thakur, J. Molecular Complexes at Euchromatin, Heterochromatin and Centromeric Chromatin. *International Journal of Molecular Sciences* **22,** 6922 (2021).

19. Ramazi, S., Allahverdi, A. & Zahiri, J. Evaluation of post-translational modifications in histone proteins: A review on histone modification defects in developmental and neurological disorders. *J Biosci* **45** (2020).

20. Yang, Y., Zhang, M. & Wang, Y. The roles of histone modifications in tumorigenesis and associated inhibitors in cancer therapy. *Journal of the National Cancer Center* **2,** 277–290 (2022).

21. Allfrey, V. G., Faulkner, R. & Mirsky, A. E. Acetylation and methylation of histones and their possible role in the regulation of rna synthesis*. *Proceedings of the National Academy of Sciences* **51,** 786–794 (1964).

22. Felsenfeld, G. A brief history of epigenetics. *Cold Spring Harbor Perspectives in Biology* **6** (2014).

23. Brownell, J. E., Zhou, J., Ranalli, T., Kobayashi, R., Edmondson, D. G., Roth, S. Y., *et al.* Tetrahymena Histone Acetyltransferase A: A Homolog to Yeast Gcn5p Linking Histone Acetylation to Gene Activation. *Cell* **84,** 843–851 (1996).

24. Padeken, J., Methot, S. P. & Gasser, S. M. Establishment of H3K9-methylated heterochromatin and its functions in tissue differentiation and maintenance. *Nature Reviews Molecular Cell Biology* **23,** 623–640 (2022).

25. Tachibana, M., Sugimoto, K., Nozaki, M., Ueda, J., Ohta, T., Ohki, M., *et al.* G9a histone methyltransferase plays a dominant role in euchromatic histone H3 lysine 9 methylation and is essential for early embryogenesis. *Genes & Development* **16,** 1779–1791 (2002).

26. Creyghton, M. P., Cheng, A. W., Welstead, G. G., Kooistra, T., Carey, B. W., Steine, E. J., *et al.* Histone H3K27ac separates active from poised enhancers and predicts developmental state. *Proceedings of the National Academy of Sciences* **107,** 21931–21936 (2010).

27. Santos-Rosa, H., Schneider, R., Bannister, A. J., Sherriff, J., Bernstein, B. E., Emre, N. C. T., *et al.* Active genes are tri-methylated at K4 of histone H3. *Nature* **419,** 407–411 (2002).

28. Bernstein, B. E., Mikkelsen, T. S., Xie, X., Kamal, M., Huebert, D. J., Cuff, J., *et al.* A bivalent chromatin structure marks key developmental genes in embryonic stem cells. *Cell* **125,** 315–26 (2006).

29. Xu, J. & Kidder, B. L. H4K20me3 co-localizes with activating histone modifications at transcriptionally dynamic regions in embryonic stem cells. *BMC genomics* **19,** 514 (2018).

30. Herz, H.-M., Mohan, M., Garruss, A. S., Liang, K., Takahashi, Y.-H., Mickey, K., *et al.* Enhancer-associated H3K4 monomethylation by Trithorax-related, the Drosophila homolog of mammalian Mll3/Mll4. *Genes & Development* **26,** 2604–2620 (2012).

31. Bae, S. & Lesch, B. J. H3K4me1 Distribution Predicts Transcription State and Poising at Promoters. *Frontiers in Cell and Developmental Biology* **8** (2020).

32. Bannister, A. J. & Kouzarides, T. Regulation of chromatin by histone modifications. *Cell Research* **21,** 381–395 (2011).

33. Andrews, F. H., Strahl, B. D. & Kutateladze, T. G. Insights into newly discovered marks and readers of epigenetic information. *Nature Chemical Biology* **12,** 662–668 (2016).

34. Botuyan, M. V., Lee, J., Ward, I. M., Kim, J.-E., Thompson, J. R., Chen, J., *et al.* Structural basis for the methylation state-specific recognition of histone H4-K20 by 53BP1 and Crb2 in DNA repair. *Cell* **127,** 1361–1373 (2006).

35. Wang, B., Matsuoka, S., Carpenter, P. B. & Elledge, S. J. 53BP1, a mediator of the DNA damage checkpoint. *Science* **298,** 1435–1438 (2002).

36. Kuo, A. J., Song, J., Cheung, P., Ishibe-Murakami, S., Yamazoe, S., Chen, J. K., *et al.* ORC1 BAH domain links H4K20me2 to DNA replication licensing and Meier-Gorlin syndrome. *Nature* **484,** 115–119 (2012).

37. Beck, D. B., Burton, A., Oda, H., Ziegler-Birling, C., Torres-Padilla, M.-E. & Reinberg, D. The role of PR-Set7 in replication licensing depends on Suv4-20h. *Genes & Development* **26,** 2580–2589 (2012).

38. Jukam, D., Shariati, S. A. M. & Skotheim, J. M. Zygotic Genome Activation in Vertebrates. *Developmental Cell* **42,** 316–332 (2017).

39. Xue, L., Cai, J.-Y., Ma, J., Huang, Z., Guo, M.-X., Fu, L.-Z., *et al.* Global expression profiling reveals genetic programs underlying the developmental divergence between mouse and human embryogenesis. *BMC Genomics* **14,** 568 (2013).

40. Dobson, A. T., Raja, R., Abeyta, M. J., Taylor, T., Shen, S., Haqq, C., *et al.* The unique transcriptome through day 3 of human preimplantation development. *Human Molecular Genetics* **13,** 1461–1470 (2004).

41. Braude, P., Bolton, V. & Moore, S. Human gene expression first occurs between the four- and eight-cell stages of preimplantation development. *Nature* **332,** 459–461 (1988).

42. Braun, R. E. Packaging paternal chromosomes with protamine. *Nature Genetics* **28,** 10–12 (2001).

43. Hammoud, S. S., Nix, D. A., Hammoud, A. O., Gibson, M., Cairns, B. R. & Carrell, D. T. Genome-wide analysis identifies changes in histone retention and epigenetic modifications at developmental and imprinted gene loci in the sperm of infertile men. *Human Reproduction* **26,** 2558–2569 (2011).

44. Saitou, M. & Kurimoto, K. Paternal Nucleosomes: Are They Retained in Developmental Promoters or Gene Deserts? *Developmental Cell* **30,** 6–8 (2014).

45. Aoki, F., Worrad, D. M. & Schultz, R. M. Regulation of Transcriptional Activity during the First and Second Cell Cycles in the Preimplantation Mouse Embryo. *Developmental Biology* **181,** 296–307 (1997).

46. Smith, R., Susor, A., Ming, H., Tait, J., Conti, M., Jiang, Z., *et al.* The H3.3 chaperone Hira complex orchestrates oocyte developmental competence. *Development* **149,** dev200044 (2022).

47. Torres-Padilla, M.-E., Bannister, A. J., Hurd, P. J., Kouzarides, T. & Zernicka-Goetz, M. Dynamic distribution of the replacement histone variant H3.3 in the mouse oocyte and preimplantation embryos. *The International Journal of Developmental Biology* **50,** 455–461 (2006).

48. Lin, C.-J., Koh, F. M., Wong, P., Conti, M. & Ramalho-Santos, M. Hira-Mediated H3.3 Incorporation Is Required for DNA Replication and Ribosomal RNA Transcription in the Mouse Zygote. *Developmental Cell* **30,** 268–279 (2014).

49. Burton, A. & Torres-Padilla, M.-E. Chromatin dynamics in the regulation of cell fate allocation during early embryogenesis. *Nature Reviews Molecular Cell Biology* **15,** 723–735 (2014).

50. Dahl, J. A., Jung, I., Aanes, H., Greggains, G. D., Manaf, A., Lerdrup, M., *et al.* Broad histone H3K4me3 domains in mouse oocytes modulate maternal-to-zygotic transition. *Nature* **537,** 548–552 (2016).

51. Liu, X., Wang, C., Liu, W., Li, J., Li, C., Kou, X., *et al.* Distinct features of H3K4me3 and H3K27me3 chromatin domains in pre-implantation embryos. *Nature* **537,** 558–562 (2016).

52. Eid, A., Rodriguez-Terrones, D., Burton, A. & Torres-Padilla, M.-E. SUV4-20 activity in the preimplantation mouse embryo controls timely replication. *Genes & Development* **30,** 2513–2526 (2016).

53. Shen, L., Inoue, A., He, J., Liu, Y., Lu, F. & Zhang, Y. Tet3 and DNA Replication Mediate Demethylation of Both the Maternal and Paternal Genomes in Mouse Zygotes. *Cell Stem Cell* **15,** 459–471 (2014).

54. Du, Z., Zheng, H., Huang, B., Ma, R., Wu, J., Zhang, X., *et al.* Allelic reprogramming of 3D chromatin architecture during early mammalian development. *Nature* **547,** 232–235 (2017).

55. Zhou, J. J. & Cho, K. W. Y. Epigenomic dynamics of early Xenopus embryos. *Development, growth & differentiation* **64,** 508 (2022).

56. Hontelez, S., van Kruijsbergen, I., Georgiou, G., van Heeringen, S. J., Bogdanovic, O., Lister, R., *et al.* Embryonic transcription is controlled by maternally defined chromatin state. *Nature Communications* **6,** 10148 (2015).

57. Owens, N. D. L., Blitz, I. L., Lane, M. A., Patrushev, I., Overton, J. D., Gilchrist, M. J., *et al.* Measuring Absolute RNA Copy Numbers at High Temporal Resolution Reveals Transcriptome Kinetics In Development. *Cell Reports* **14,** 632–647 (2016).

58. Collart, C., Owens, N. D. L., Bhaw-Rosun, L., Cooper, B., De Domenico, E., Patrushev, I., *et al.* High-resolution analysis of gene activity during the Xenopus mid-blastula transition. *Development* **141,** 1927–1939 (2014).

59. Akkers, R. C., van Heeringen, S. J., Jacobi, U. G., Janssen-Megens, E. M., Françoijs, K.-J., Stunnenberg, H. G., *et al.* A hierarchy of H3K4me3 and H3K27me3 acquisition in spatial gene regulation in Xenopus embryos. *Developmental cell* **17,** 425–434 (2009).

60. Gupta, R., Wills, A., Ucar, D. & Baker, J. Developmental enhancers are marked independently of zygotic Nodal signals in Xenopus. *Developmental biology* **395,** 38–49 (2014).

61. Niu, L., Shen, W., Shi, Z., Tan, Y., He, N., Wan, J., *et al.* Three-dimensional folding dynamics of the Xenopus tropicalis genome. *Nature Genetics* **53,** 1075–1087 (2021).

62. Bogdanović, O., Long, S. W., Heeringen, S. J. v., Brinkman, A. B., Gómez-Skarmeta, J. L., Stunnenberg, H. G., *et al.* Temporal uncoupling of the DNA methylome and transcriptional repression during embryogenesis. *Genome Research* **21,** 1313–1327 (2011).

63. Veenstra, G. J. C. & Wolffe, A. P. Constitutive genomic methylation during embryonic development of *Xenopus*. *Biochimica et Biophysica Acta (BBA) - Gene Structure and Expression* **1521,** 39–44 (2001).

64. Weisman, A. I., Snyder, A. F. & Coates, C. W. The “frog” test (Xenopus laevis) as a rapid diagnostic test for pregnancy: Preliminary report. *American Journal of Obstetrics and Gynecology* **43,** 135–139 (1942).

65. Carotenuto, R., Pallotta, M. M., Tussellino, M. & Fogliano, C. Xenopus laevis (Daudin, 1802) as a Model Organism for Bioscience: A Historic Review and Perspective. *Biology* **12** (2023).

66. Cannatella, D. C. & Sa, R. O. D. XenopusLauevis as a Model Organism. *Systematic Biology* **42** (1993).

67. Blum, M. & Ott, T. Xenopus: An Undervalued Model Organism to Study and Model Human Genetic Disease. *Cells Tissues Organs* **205,** 303–313 (2018).

68. Sato, K.-i. & Tokmakov, A. A. Toward the understanding of biology of oocyte life cycle in Xenopus Laevis: No oocytes left behind. *Reproductive Medicine and Biology* **19,** 114–119 (2020).

69. Tokmakov, A. A., Stefanov, V. E., Iwasaki, T., Sato, K.-I. & Fukami, Y. Calcium Signaling and Meiotic Exit at Fertilization in Xenopus Egg. *International Journal of Molecular Sciences* **15,** 18659–18676 (2014).

70. Kline, D., Simoncini, L., Mandel, G., Maue, R. A., Kado, R. T. & Jaffe, L. A. Fertilization Events Induced by Neurotransmitters After Injection of mRNA in Xenopus Eggs. *Science* **241,** 464–467 (1988).

71. Dettlaff, T. & Rudneva, T. The clawed frog Xenopus laevis Daudin. *Objects of Developmental Biology,* 392–441 (1975).

72. Newport, J. W. & Kirschner, M. W. Regulation of the cell cycle during early Xenopus development. *Cell* **37,** 731–742 (1984).

73. Satoh, N. 'Metachronous' Cleavage and Initiation of Gastrulation in Amphibian Embryos. *Development, Growth & Differentiation* **19,** 111–117 (1977).

74. Jukam, D., Kapoor, R. R., Straight, A. F. & Skotheim, J. M. The DNA-to-cytoplasm ratio broadly activates zygotic gene expression in *Xenopus*. *Current Biology* **31,** 4269–4281.e8 (2021).

75. Anderson, J. A., Lewellyn, A. L. & Maller, J. L. Ionizing radiation induces apoptosis and elevates cyclin A1-Cdk2 activity before but not after the midblastula transition in Xenopus. *Molecular Biology of the Cell* **8,** 1195–1206 (1997).

76. Shook, D. R., Kasprowicz, E. M., Davidson, L. A. & Keller, R. Large, long range tensile forces drive convergence during Xenopus blastopore closure and body axis elongation. *eLife* **7** (ed McDevitt, T. C.) e26944 (2018).

77. Nowotschin, S., Hadjantonakis, A.-K. & Campbell, K. The endoderm: a divergent cell lineage with many commonalities. *Development* **146,** dev150920 (2019).

78. Ferretti, E. & Hadjantonakis, A.-K. Mesoderm specification and diversification: from single cells to emergent tissues. *Current Opinion in Cell Biology. Differentiation and disease* **61,** 110–116 (2019).

79. Li, L., Liu, C., Biechele, S., Zhu, Q., Song, L., Lanner, F., *et al.* Location of transient ectodermal progenitor potential in mouse development. *Development* **140,** 4533–4543 (2013).

80. Zahn, N., Levin, M. & Adams, D. S. The Zahn drawings: new illustrations of Xenopus embryo and tadpole stages for studies of craniofacial development. *Development* **144,** 2708–2713 (2017).

81. Walentek, P. Xenopus epidermal and endodermal epithelia as models for mucociliary epithelial evolution, disease, and metaplasia. *genesis* **59,** e23406 (2021).

82. Bustamante-Marin, X. M. & Ostrowski, L. E. Cilia and Mucociliary Clearance. *Cold Spring Harbor Perspectives in Biology* **9,** a028241 (2017).

83. Walentek, P. & Quigley, I. K. What we can learn from a tadpole about ciliopathies and airway diseases: Using systems biology in Xenopus to study cilia and mucociliary epithelia. *genesis* **55,** e23001 (2017).

84. Barker, A. R., Renzaglia, K. S., Fry, K. & Dawe, H. R. Bioinformatic analysis of ciliary transition zone proteins reveals insights into the evolution of ciliopathy networks. *BMC genomics* **15,** 531 (2014).

85. Livraghi, A. & Randell, S. H. Cystic Fibrosis and Other Respiratory Diseases of Impaired Mucus Clearance. *Toxicologic Pathology* **35,** 116–129 (2007).

86. Knowles, M. R., Zariwala, M. & Leigh, M. Primary Ciliary Dyskinesia. *Clinics in Chest Medicine* **37,** 449–61 (2016).

87. Stubbs, J. L., Davidson, L., Keller, R. & Kintner, C. Radial intercalation of ciliated cells during Xenopus skin development. *Development* **133,** 2507–2515 (2006).

88. Werner, M. & Mitchell, B. Understanding ciliated epithelia: The power of Xenopus. *genesis* **50,** 176–185 (2012).

89. Quigley, I. K., Stubbs, J. L. & Kintner, C. Specification of ion transport cells in the Xenopus larval skin. *Development* **138,** 705–714 (2011).

90. Goetz, S. C. & Anderson, K. V. The Primary Cilium: A Signaling Center During Vertebrate Development. *Nature reviews. Genetics* **11,** 331–344 (2010).

91. Brooks, E. R. & Wallingford, J. B. Multiciliated cells: a review. *Current biology : CB* **24,** R973–R982 (2014).

92. Patel, M. M. & Tsiokas, L. Insights into the Regulation of Ciliary Disassembly. *Cells* **10.** Number: 11 Publisher: Multidisciplinary Digital Publishing Institute, 2977 (2021).

93. Garcia, G., Raleigh, D. R. & Reiter, J. F. How the ciliary membrane is organized inside-out to communicate outside-in. *Current biology : CB* **28,** R421–R434 (2018).

94. Hu, Q., Milenkovic, L., Jin, H., Scott, M. P., Nachury, M. V., Spiliotis, E. T., *et al.* A septin diffusion barrier at the base of the primary cilium maintains ciliary membrane protein distribution. *Science* **329,** 436–439 (2010).

95. Wang, L., Wen, X., Wang, Z., Lin, Z., Li, C., Zhou, H., *et al.* Ciliary transition zone proteins coordinate ciliary protein composition and ectosome shedding. *Nature Communications* **13,** 3997 (2022).

96. Zhang, S. & Mitchell, B. J. Basal bodies in Xenopus. *Cilia* **5,** 2 (2016).

97. Park, T. J., Mitchell, B. J., Abitua, P. B., Kintner, C. & Wallingford, J. B. Dishevelled controls apical docking and planar polarization of basal bodies in ciliated epithelial cells. *Nature Genetics* **40,** 871–879 (2008).

98. Ioannou, A., Santama, N. & Skourides, P. A. *Xenopus laevis* nucleotide binding protein 1 (xNubp1) is important for convergent extension movements and controls ciliogenesis via regulation of the actin cytoskeleton. *Developmental Biology* **380,** 243–258 (2013).

99. Werner, M. E., Hwang, P., Huisman, F., Taborek, P., Yu, C. C. & Mitchell, B. J. Actin and microtubules drive differential aspects of planar cell polarity in multiciliated cells. *The Journal of Cell Biology* **195,** 19–26 (2011).

100. Boutin, C. & Kodjabachian, L. Biology of multiciliated cells. *Current Opinion in Genetics & Development* **56,** 1–7 (2019).

101. Wallingford, J. B. Planar cell polarity signaling, cilia and polarized ciliary beating. *Current Opinion in Cell Biology. Cell-to-cell contact and extracellular matrix* **22,** 597–604 (2010).

102. Meunier, A. & Azimzadeh, J. Multiciliated Cells in Animals. *Cold Spring Harbor Perspectives in Biology* **8** (2016).

103. Zhao, H., Zhu, L., Zhu, Y., Cao, J., Li, S., Huang, Q., *et al.* The Cep63 paralogue Deup1 enables massive de novo centriole biogenesis for vertebrate multiciliogenesis. *Nature Cell Biology* **15,** 1434–1444 (2013).

104. Tang, T. K. Centriole biogenesis in multiciliated cells. *Nature Cell Biology* **15,** 1400–1402 (2013).

105. Al Jord, A., Shihavuddin, A., Servignat d'Aout, R., Faucourt, M., Genovesio, A., Karaiskou, A., *et al.* Calibrated mitotic oscillator drives motile ciliogenesis. *Science* **358,** 803–806 (2017).

106. Mercey, O., Levine, M. S., LoMastro, G. M., Rostaing, P., Brotslaw, E., Gomez, V., *et al.* Massive centriole production can occur in the absence of deuterosomes in multiciliated cells. *Nature Cell Biology* **21,** 1544–1552 (2019).

107. Rayamajhi, D. & Roy, S. Multiciliated Cells: Rise and Fall of the Deuterosomes. *Trends in Cell Biology* **30,** 259–262 (2020).

108. Leroux, M. R. Taking Vesicular Transport to the Cilium. *Cell* **129,** 1041–1043 (2007).

109. Wang, S., Luo, Y., Wilson, P. D., Witman, G. B. & Zhou, J. The Autosomal Recessive Polycystic Kidney Disease Protein Is Localized to Primary Cilia, with Concentration in the Basal Body Area. *Journal of the American Society of Nephrology* **15,** 592 (2004).

110. Chien, A., Shih, S. M., Bower, R., Tritschler, D., Porter, M. E. & Yildiz, A. Dynamics of the IFT machinery at the ciliary tip. *eLife* **6,** e28606.

111. Stubbs, J. L., Vladar, E. K., Axelrod, J. D. & Kintner, C. Multicilin promotes centriole assembly and ciliogenesis during multiciliate cell differentiation. *Nature Cell Biology* **14,** 140–7 (2012).

112. Ma, L., Quigley, I., Omran, H. & Kintner, C. Multicilin drives centriole biogenesis via E2f proteins. *Genes & Development* **28,** 1461–1471 (2014).

113. Chevalier, B., Adamiok, A., Mercey, O., Revinski, D. R., Zaragosi, L.-E., Pasini, A., *et al.* miR-34/449 control apical actin network formation during multiciliogenesis through small GTPase pathways. *Nature Communications* **6,** 8386 (2015).

114. Wallmeier, J., Al-Mutairi, D. A., Chen, C.-T., Loges, N. T., Pennekamp, P., Menchen, T., *et al.* Mutations in CCNO result in congenital mucociliary clearance disorder with reduced generation of multiple motile cilia. *Nature Genetics* **46,** 646–651 (2014).

115. Stubbs, J. L., Oishi, I., Izpisúa Belmonte, J. C. & Kintner, C. The forkhead protein Foxj1 specifies node-like cilia in Xenopus and zebrafish embryos. *Nature Genetics* **40,** 1454–1460 (2008).

116. Quigley, I. K. & Kintner, C. Rfx2 Stabilizes Foxj1 Binding at Chromatin Loops to Enable Multiciliated Cell Gene Expression. *PLoS Genetics* **13,** e1006538 (2017).

117. Chung, M.-I., Peyrot, S. M., LeBoeuf, S., Park, T. J., McGary, K. L., Marcotte, E. M., *et al.* RFX2 is broadly required for ciliogenesis during vertebrate development. *Developmental Biology* **363,** 155–165 (2012).

118. Deblandre, G. A., Wettstein, D. A., Koyano-Nakagawa, N. & Kintner, C. A two-step mechanism generates the spacing pattern of the ciliated cells in the skin of Xenopus embryos. *Development* **126,** 4715–4728 (1999).

119. Nicetto, D. *On the way to differentiation.* Dissertation (Ludwig-Maximilians-Universität München, 2012).

120. Fang, J., Feng, Q., Ketel, C. S., Wang, H., Cao, R., Xia, L., *et al.* Purification and Functional Characterization of SET8, a Nucleosomal Histone H4-Lysine 20-Specific Methyltransferase. *Current Biology* **12,** 1086–1099 (2002).

121. Nishioka, K., Rice, J. C., Sarma, K., Erdjument-Bromage, H., Werner, J., Wang, Y., *et al.* PR-Set7 Is a Nucleosome-Specific Methyltransferase that Modifies Lysine 20 of Histone H4 and Is Associated with Silent Chromatin. *Molecular Cell* **9,** 1201–1213 (2002).

122. Pokrovsky, D., Forné, I., Straub, T., Imhof, A. & Rupp, R. A. W. A systemic cell cycle block impacts stage-specific histone modification profiles during Xenopus embryogenesis. *PLoS Biology* **19,** e3001377 (2021).

123. Corvalan, A. Z. & Coller, H. A. Methylation of histone 4's lysine 20: a critical analysis of the state of the field. *Physiological Genomics* **53,** 22–32 (2020).

124. Young, N. L., DiMaggio, P. A., Plazas-Mayorca, M. D., Baliban, R. C., Floudas, C. A. & Garcia, B. A. High Throughput Characterization of Combinatorial Histone Codes. *Molecular & Cellular Proteomics : MCP* **8,** 2266–2284 (2009).

125. Yang, H., Pesavento, J. J., Starnes, T. W., Cryderman, D. E., Wallrath, L. L., Kelleher, N. L., *et al.* Preferential Dimethylation of Histone H4 Lysine 20 by Suv4-20. *The Journal of Biological Chemistry* **283,** 12085–12092 (2008).

126. Oda, H., Okamoto, I., Murphy, N., Chu, J., Price, S. M., Shen, M. M., *et al.* Monomethylation of Histone H4-Lysine 20 Is Involved in Chromosome Structure and Stability and Is Essential for Mouse Development. *Molecular and Cellular Biology* **29,** 2278–2295 (2009).

127. Schotta, G., Sengupta, R., Kubicek, S., Malin, S., Kauer, M., Callén, E., *et al.* A chromatin-wide transition to H4K20 monomethylation impairs genome integrity and programmed DNA rearrangements in the mouse. *Genes & Development* **22,** 2048–2061 (2008).

128. Evertts, A. G., Manning, A. L., Wang, X., Dyson, N. J., Garcia, B. A. & Coller, H. A. H4K20 methylation regulates quiescence and chromatin compaction. *Molecular Biology of the Cell* **24,** 3025–3037 (2013).

129. Liu, W., Tanasa, B., Tyurina, O. V., Zhou, T. Y., Gassmann, R., Liu, W. T., *et al.* PHF8 mediates histone H4 lysine 20 demethylation events involved in cell cycle progression. *Nature* **466,** 508–512 (2010).

130. Qi, H. H., Sarkissian, M., Hu, G.-Q., Wang, Z., Bhattacharjee, A., Gordon, D. B., *et al.* Histone H4K20/H3K9 demethylase PHF8 regulates zebrafish brain and craniofacial development. *Nature* **466,** 503–507 (2010).

131. Brejc, K., Bian, Q., Uzawa, S., Wheeler, B. S., Anderson, E. C., King, D. S., *et al.* Dynamic Control of X Chromosome Conformation and Repression by a Histone H4K20 Demethylase. *Cell* **171,** 85–102.e23 (2017).

132. Shoaib, M., Chen, Q., Shi, X., Nair, N., Prasanna, C., Yang, R., *et al.* Histone H4 lysine 20 mono-methylation directly facilitates chromatin openness and promotes transcription of housekeeping genes. *Nature Communications* **12,** 4800 (2021).

133. Barski, A., Cuddapah, S., Cui, K., Roh, T.-Y., Schones, D. E., Wang, Z., *et al.* High-Resolution Profiling of Histone Methylations in the Human Genome. *Cell* **129,** 823–837 (2007).

134. Congdon, L. M., Houston, S. I., Veerappan, C. S., Spektor, T. M. & Rice, J. C. PR-Set7-mediated monomethylation of histone H4 lysine 20 at specific genomic regions induces transcriptional repression. *Journal of Cellular Biochemistry* **110,** 609–619 (2010).

135. Trojer, P., Li, G., Sims, R. J., Vaquero, A., Kalakonda, N., Boccuni, P., *et al.* L3MBTL1, a Histone-Methylation-Dependent Chromatin Lock. *Cell* **129,** 915–928 (2007).

136. Gurvich, N., Perna, F., Farina, A., Voza, F., Menendez, S., Hurwitz, J., *et al.* L3MBTL1 polycomb protein, a candidate tumor suppressor in del(20q12) myeloid disorders, is essential for genome stability. *Proceedings of the National Academy of Sciences* **107,** 22552–22557 (2010).

137. Boccuni, P., MacGrogan, D., Scandura, J. M. & Nimer, S. D. The human L(3)MBT polycomb group protein is a transcriptional repressor and interacts physically and functionally with TEL (ETV6). *The Journal of Biological Chemistry* **278,** 15412–15420 (2003).

138. Tjalsma, S. J. D., Hori, M., Sato, Y., Bousard, A., Ohi, A., Raposo, A. C., *et al.* H4K20me1 and H3K27me3 are concurrently loaded onto the inactive X chromosome but dispensable for inducing gene silencing. *EMBO Reports* **22,** e51989 (2021).

139. Jørgensen, S., Schotta, G. & Sørensen, C. S. Histone H4 Lysine 20 methylation: key player in epigenetic regulation of genomic integrity. *Nucleic Acids Research* **41,** 2797–2806 (2013).

140. Sobering, A. K., Bryant, L. M., Li, D., McGaughran, J., Maystadt, I., Moortgat, S., *et al.* Variants in PHF8 cause a spectrum of X-linked neurodevelopmental disorders and facial dysmorphology. *Human Genetics and Genomics Advances* **3,** 100102 (2022).

141. Gabellini, D. & Pedrotti, S. The SUV4-20H Histone Methyltransferases in Health and Disease. *International Journal of Molecular Sciences* **23,** 4736 (2022).

142. Wu, H., Siarheyeva, A., Zeng, H., Lam, R., Dong, A., Wu, X.-H., *et al.* Crystal structures of the human histone H4K20 methyltransferases SUV420H1 and SUV420H2. *FEBS Letters* **587,** 3859–3868 (2013).

143. Wickramasekara, R. N. & Stessman, H. A. F. Histone 4 Lysine 20 Methylation: A Case for Neurodevelopmental Disease. *Biology* **8** (2019).

144. Nicetto, D., Hahn, M., Jung, J., Schneider, T. D., Straub, T., David, R., *et al.* Suv4-20h Histone Methyltransferases Promote Neuroectodermal Differentiation by Silencing the Pluripotency-Associated Oct-25 Gene. *PLoS Genetics* **9,** e1003188 (2013).

145. Berges, J. *H4K20 di-methylation and multiciliogenesis.* Dissertation (Ludwig-Maximilians-Universität München, 2021).

146. Angerilli, A. *Histone H4K20 methylation phases cytoskeletal dynamics with the cell cycle during Xenopus mucociliary epithelium formation.* Dissertation (Ludwig-Maximilians-Universität München, 2018).

147. Buenrostro, J. D., Giresi, P. G., Zaba, L. C., Chang, H. Y. & Greenleaf, W. J. Transposition of native chromatin for fast and sensitive epigenomic profiling of open chromatin, DNA-binding proteins and nucleosome position. *Nature Methods* **10,** 1213–1218 (2013).

148. Esmaeili, M., Blythe, S. A., Tobias, J. W., Zhang, K., Yang, J. & Klein, P. S. Chromatin accessibility and histone acetylation in the regulation of competence in early development. *Developmental biology* **462,** 20–35 (2020).

149. Liebler, D. C. & Zimmerman, L. J. Targeted Quantitation of Proteins by Mass Spectrometry. *Biochemistry* **52,** 3797–3806 (2013).

150. Moody, S. A. & Kline, M. J. Segregation of fate during cleavage of frog (Xenopus laevis) blastomeres. *Anatomy and Embryology* **182,** 347–362 (1990).

151. Angerilli, A., Tait, J., Berges, J., Shcherbakova, I., Pokrovsky, D., Schauer, T., *et al.* The histone H4K20 methyltransferase SUV4-20H1/KMT5B is required for multiciliated cell differentiation in Xenopus. *Life Science Alliance* **6** (2023).

152. Asensio-Juan, E., Fueyo, R., Pappa, S., Iacobucci, S., Badosa, C., Lois, S., *et al.* The histone demethylase PHF8 is a molecular safeguard of the IFNγ response. *Nucleic Acids Research* **45,** 3800–3811 (2017).

153. Dillon, S. C., Zhang, X., Trievel, R. C. & Cheng, X. The SET-domain protein superfamily: protein lysine methyltransferases. *Genome Biology* **6,** 227 (2005).

154. Kwon, T., Chang, J. H., Kwak, E., Lee, C. W., Joachimiak, A., Kim, Y. C., *et al.* Mechanism of histone lysine methyl transfer revealed by the structure of SET7/9—AdoMet. *The EMBO Journal* **22,** 292–303 (2003).

155. Fortschegger, K., de Graaf, P., Outchkourov, N. S., van Schaik, F. M. A., Timmers, H. T. M. & Shiekhattar, R. PHF8 targets histone methylation and RNA polymerase II to activate transcription. *Molecular and Cellular Biology* **30,** 3286–3298 (2010).

156. Session, A. M., Uno, Y., Kwon, T., Chapman, J. A., Toyoda, A., Takahashi, S., *et al.* Genome evolution in the allotetraploid frog Xenopus laevis. *Nature* **538,** 336–343 (2016).

157. Winterbottom, E. F., Ramsbottom, S. A. & Isaacs, H. V. Gsx transcription factors repress Iroquois gene expression. *Developmental Dynamics* **240,** 1422–1429 (2011).

158. Jing, Z., Yin, H., Wang, P., Gao, J. & Yuan, L. Centlein, a novel microtubule-associated protein stabilizing microtubules and involved in neurite formation. *Biochemical and Biophysical Research Communications* **472,** 360–365 (2016).

159. Kim, S., Zaghloul, N. A., Bubenshchikova, E., Oh, E. C., Rankin, S., Katsanis, N., *et al.* Nde1-mediated inhibition of ciliogenesis affects cell cycle re-entry. *Nature Cell Biology* **13,** 351–60 (2011).

160. Karunakaran, K. B., Chaparala, S., Lo, C. W. & Ganapathiraju, M. K. Cilia interactome with predicted protein–protein interactions reveals connections to Alzheimer's disease, aging and other neuropsychiatric processes. *Scientific Reports* **10,** 15629 (2020).

161. Nielsen, M. G., Turner, F. R., Hutchens, J. A. & Raff, E. C. Axoneme-specific beta-tubulin specialization: a conserved C-terminal motif specifies the central pair. *Current biology: CB* **11,** 529–533 (2001).

162. Sewell, M. T., Legué, E. & Liem, K. F. Tubb4b is required for multi-ciliogenesis in the mouse. *Development* **151,** dev201819 (2024).

163. Zhang, J., Zhang, Y., Liu, J., Luo, J., Yun, Y. & Cao, Y. Identification of TUBB4A as a Prognostic Biomarker of Melanoma by Transcriptomic Data and In Vitro Experiments. *Technology in Cancer Research & Treatment* **22,** 15330338231184842 (2023).

164. Zhou, F., Narasimhan, V., Shboul, M., Chong, Y. L., Reversade, B. & Roy, S. Gmnc Is a Master Regulator of the Multiciliated Cell Differentiation Program. *Current Biology* **25,** 3267–3273 (2015).

165. Brody, S. L., Yan, X. H., Wuerffel, M. K., Song, S.-K. & Shapiro, S. D. Ciliogenesis and Left–Right Axis Defects in Forkhead Factor HFH-4–Null Mice. *American Journal of Respiratory Cell and Molecular Biology* **23,** 45–51 (2000).

166. You, Y., Huang, T., Richer, E. J., Schmidt, J.-E. H., Zabner, J., Borok, Z., *et al.* Role of f-box factor foxj1 in differentiation of ciliated airway epithelial cells. *American Journal of Physiology-Lung Cellular and Molecular Physiology* **286,** L650–L657 (2004).

167. Yu, X., Ng, C. P., Habacher, H. & Roy, S. Foxj1 transcription factors are master regulators of the motile ciliogenic program. *Nature Genetics* **40,** 1445–1453 (2008).

168. Lewis, M. & Stracker, T. H. Transcriptional regulation of multiciliated cell differentiation. *Seminars in Cell & Developmental Biology. Cilia and centrosomes in development, physiology and disease* **110,** 51–60 (2021).

169. Tan, F. E., Vladar, E. K., Ma, L., Fuentealba, L. C., Hoh, R., Espinoza, F. H., *et al.* Myb promotes centriole amplification and later steps of the multiciliogenesis program. *Development* **140,** 4277 (2013).

170. Wang, L., Fu, C., Fan, H., Du, T., Dong, M., Chen, Y., *et al.* miR-34b regulates multiciliogenesis during organ formation in zebrafish. *Development* **140,** 2755–2764 (2013).

171. Rg, R. & Tj, G. MYB function in normal and cancer cells. *Nature reviews. Cancer* **8** (2008).

172. Funk, M. C., Bera, A. N., Menchen, T., Kuales, G., Thriene, K., Lienkamp, S. S., *et al.* Cyclin O (Ccno) functions during deuterosome-mediated centriole amplification of multiciliated cells. *The EMBO Journal* **34,** 1078–1089 (2015).

173. Attwooll, C., Denchi, E. L. & Helin, K. The E2F family: specific functions and overlapping interests. *The EMBO Journal* **23,** 4709 (2004).

174. Stefano, L. D., Jensen, M. R. & Helin, K. E2F7, a novel E2F featuring DP-independent repression of a subset of E2F-regulated genes. *The EMBO Journal* (2003).

175. Choksi, S. P., Byrnes, L. E., Konjikusic, M. J., Tsai, B. W. H., Deleon, R., Lu, Q., *et al.* An alternative cell cycle coordinates multiciliated cell differentiation. *Nature* **630,** 214–221 (2024).

176. Plouhinec, J.-L., Medina-Ruiz, S., Borday, C., Bernard, E., Vert, J.-P., Eisen, M. B., *et al.* A molecular atlas of the developing ectoderm defines neural, neural crest, placode, and nonneural progenitor identity in vertebrates. *PLoS Biology* **15,** e2004045 (2017).

177. Kim, S., Ma, L., Shokhirev, M. N., Quigley, I. & Kintner, C. Multicilin and activated E2f4 induce multiciliated cell differentiation in primary fibroblasts. *Scientific Reports* **8,** 12369 (2018).

178. Gentsch, G. E. & Smith, J. C. in *Eukaryotic Transcriptional and Post-Transcriptional Gene Expression Regulation* (eds Wajapeyee, N. & Gupta, R.) 23–42 (Springer New York, New York, NY, 2017).

179. Akkers, R. C., Jacobi, U. G. & Veenstra, G. J. C. Chromatin immunoprecipitation analysis of Xenopus embryos. *Methods in Molecular Biology* **917,** 279–292 (2012).

180. Hörmanseder, E., Simeone, A., Allen, G. E., Bradshaw, C. R., Figlmüller, M., Gurdon, J., *et al.* H3K4 Methylation-Dependent Memory of Somatic Cell Identity Inhibits Reprogramming and Development of Nuclear Transfer Embryos. *Cell Stem Cell* **21,** 135–143.e6 (2017).

181. Wills, A. E., Gupta, R., Chuong, E. & Baker, J. C. Chromatin immunoprecipitation and deep sequencing in Xenopus tropicalis and Xenopus laevis. *Methods* **66,** 410–421 (2014).

182. Phelps, W. A., Hurton, M. D., Ayers, T. N., Carlson, A. E., Rosenbaum, J. C. & Lee, M. T. Hybridization led to a rewired pluripotency network in the allotetraploid Xenopus laevis. *eLife* **12,** e83952 (2023).

183. Lu, X., Simon, M. D., Chodaparambil, J. V., Hansen, J. C., Shokat, K. M. & Luger, K. The effect of H3K79 dimethylation and H4K20 trimethylation on nucleosome and chromatin structure. *Nature structural & molecular biology* **15,** 1122–1124 (2008).

184. Ma, S. & Zhang, Y. Profiling chromatin regulatory landscape: insights into the development of ChIP-seq and ATAC-seq. *Molecular Biomedicine* **1,** 1–13 (2020).

185. Hahn, M., Dambacher, S., Dulev, S., Kuznetsova, A. Y., Eck, S., Wörz, S., *et al.* Suv4-20h2 mediates chromatin compaction and is important for cohesin recruitment to heterochromatin. *Genes & Development* **27,** 859–872 (2013).

186. Stessman, H. A. F., Xiong, B., Coe, B. P., Wang, T., Hoekzema, K., Fenckova, M., *et al.* Targeted sequencing identifies 91 neurodevelopmental disorder risk genes with autism and developmental disability biases. *Nature Genetics* **49,** 515–526 (2017).

187. Zaidi, S., Choi, M., Wakimoto, H., Ma, L., Jiang, J., Overton, J. D., *et al.* De novo mutations in histone-modifying genes in congenital heart disease. *Nature* **498,** 220–223 (2013).

188. Boonsanay, V., Zhang, T., Georgieva, A., Kostin, S., Qi, H., Yuan, X., *et al.* Regulation of Skeletal Muscle Stem Cell Quiescence by Suv4-20h1-Dependent Facultative Heterochromatin Formation. *Cell Stem Cell* **18,** 229–242 (2016).

189. Hanquier, J. N., Sanders, K., Berryhill, C. A., Sahoo, F. K., Hudmon, A., Vilseck, J. Z., *et al.* Identification of nonhistone substrates of the lysine methyltransferase PRDM9. *Journal of Biological Chemistry* **299** (2023).

190. Chin, H. G., Esteve, P. O., Ruse, C., Lee, J., Schaus, S. E., Pradhan, S., *et al.* The microtubule-associated histone methyltransferase SET8, facilitated by transcription factor LSF, methylates α-tubulin. *J Biol Chem* **295,** 4748–4759 (2020).

191. Weirich, S., Kudithipudi, S. & Jeltsch, A. Specificity of the SUV4–20H1 and SUV4–20H2 protein lysine methyltransferases and methylation of novel substrates. *Journal of Molecular Biology* **428,** 2344–2358 (2016).

192. Lasser, M., Sun, N., Xu, Y., Wang, S., Drake, S., Law, K., *et al.* Pleiotropy of autism-associated chromatin regulators. *Development* **150,** dev201515 (2023).

193. Neguembor, M. V., Xynos, A., Onorati, M. C., Caccia, R., Bortolanza, S., Godio, C., *et al.* FSHD muscular dystrophy region gene 1 binds Suv4-20h1 histone methyltransferase and impairs myogenesis. *Journal of Molecular Cell Biology* **5,** 294–307 (2013).

194. Hanel, M. L., Wuebbles, R. D. & Jones, P. L. Muscular dystrophy candidate gene FRG1 is critical for muscle development. *Developmental Dynamics* **238,** 1502–1512 (2009).

195. Wuebbles, R. D., Hanel, M. L. & Jones, P. L. FSHD region gene 1 (FRG1) is crucial for angiogenesis linking FRG1 to facioscapulohumeral muscular dystrophy-associated vasculopathy. *Disease Models & Mechanisms* **2,** 267–274 (2009).

196. Inoko, A., Matsuyama, M., Goto, H., Ohmuro-Matsuyama, Y., Hayashi, Y., Enomoto, M., *et al.* Trichoplein and Aurora A block aberrant primary cilia assembly in proliferating cells. *The Journal of Cell Biology* **197,** 391–405 (2012).

197. Goto, H., Inaba, H. & Inagaki, M. Mechanisms of ciliogenesis suppression in dividing cells. *Cellular and molecular life sciences: CMLS* **74,** 881–890 (2017).

198. Ishikawa, H. & Marshall, W. F. Ciliogenesis: building the cell's antenna. *Nature Reviews. Molecular Cell Biology* **12,** 222–234 (2011).

199. Pazour, G. J., Dickert, B. L., Vucica, Y., Seeley, E. S., Rosenbaum, J. L., Witman, G. B., *et al.* Chlamydomonas IFT88 and Its Mouse Homologue, Polycystic Kidney Disease Gene Tg737, Are Required for Assembly of Cilia and Flagella. *The Journal of Cell Biology* **151,** 709–718 (2000).

200. Robert, A., Margall-Ducos, G., Guidotti, J.-E., Brégerie, O., Celati, C., Bréchot, C., *et al.* The intraflagellar transport component IFT88/polaris is a centrosomal protein regulating G1-S transition in non-ciliated cells. *Journal of Cell Science* **120,** 628–637 (2007).

201. Schuh, L., Loos, C., Pokrovsky, D., Imhof, A., Rupp, R. A. W. & Marr, C. H4K20 Methylation Is Differently Regulated by Dilution and Demethylation in Proliferating and Cell-Cycle-Arrested Xenopus Embryos. *Cell Systems* **11,** 653–662.e8 (2020).

202. Kurup, J. T., Han, Z., Jin, W. & Kidder, B. L. H4K20me3 methyltransferase SUV420H2 shapes the chromatin landscape of pluripotent embryonic stem cells. *Development* **147,** dev188516 (2020).

203. Zhao, S., Mo, G., Wang, Q., Xu, J., Yu, S., Huang, Z., *et al.* Role of RB1 in neurodegenerative diseases: inhibition of post-mitotic neuronal apoptosis via Kmt5b. *Cell Death Discovery* **10,** 182 (2024).

204. Vidarsson, H., Westergren, R., Heglind, M., Blomqvist, S. R., Breton, S. & Enerbäck, S. The forkhead transcription factor Foxi1 is a master regulator of vacuolar H-ATPase proton pump subunits in the inner ear, kidney and epididymis. *PloS One* **4,** e4471 (2009).

205. Crain, A. T., Butler, M. B., Hill, C. A., Huynh, M., McGinty, R. K. & Duronio, R. J. Drosophila melanogaster Set8 and L(3)mbt function in gene expression independently of histone H4 lysine 20 methylation. *Genes & Development* **38,** 455–472 (2024).

206. Pengelly, A. R., Copur, Ö., Jäckle, H., Herzig, A. & Müller, J. A histone mutant reproduces the phenotype caused by loss of histone-modifying factor Polycomb. *Science* **339,** 698–699 (2013).

207. Zhang, W., Zhang, X., Xue, Z., Li, Y., Ma, Q., Ren, X., *et al.* Probing the Function of Metazoan Histones with a Systematic Library of H3 and H4 Mutants. *Developmental Cell* **48,** 406–419.e5 (2019).

208. Policarpi, C., Dabin, J. & Hackett, J. A. Epigenetic editing: Dissecting chromatin function in context. *BioEssays* **43,** 2000316 (2021).

209. Hilton, I. B., D'Ippolito, A. M., Vockley, C. M., Thakore, P. I., Crawford, G. E., Reddy, T. E., *et al.* Epigenome editing by a CRISPR-Cas9-based acetyltransferase activates genes from promoters and enhancers. *Nature Biotechnology* **33,** 510–517 (2015).

210. Deniz, E., Pasha, M., Guerra, M. E., Viviano, S., Ji, W., Konstantino, M., *et al.* CFAP45, a heterotaxy and congenital heart disease gene, affects cilia stability. *Developmental Biology* **499,** 75–88 (2023).

211. Wang, Z.-J., Rein, B., Zhong, P., Williams, J., Cao, Q., Yang, F., *et al.* Autism risk gene KMT5B deficiency in prefrontal cortex induces synaptic dysfunction and social deficits via alterations of DNA repair and gene transcription. *Neuropsychopharmacology: Official Publication of the American College of Neuropsychopharmacology* **46,** 1617–1626 (2021).

212. Bröhm, A., Elsawy, H., Rathert, P., Kudithipudi, S., Schoch, T., Schuhmacher, M. K., *et al.* Somatic Cancer Mutations in the SUV420H1 Protein Lysine Methyltransferase Modulate Its Catalytic Activity. *Journal of Molecular Biology* **431,** 3068–3080 (2019).

List of Figures

List of Tables

Glossary

ATAC Assay for Transposase-Accessible Chromatin

bb basal body

bp base pair

c-myb MYB Proto-Oncogene, Transcription Factor

c.i. catalytically inactive

ccno Cyclin O

ChIP chromatin immunoprecipitation

CoMo control morpholino

dll1 Delta-like 1

DNA deoxyribonucleic acid

dnal4 Dynein Axonemal Light Chain 4

foxj1 Forkhead Box J1

GFP green fluorescent protein

GO Gene Ontology

H1H2Mo suv4-20h1/2 morpholino

H1Mo suv4-20h1 morpholino

H2Mo suv4-20h2 morpholino

H3K27ac histone H3 lysine 27 mono-acetylated

H3K4me3 histone H3 lysine 4 trimethyl

H3K9me3 histone H3 lysine 9 trimethyl

H4K20 histone H4 lysine 20

hCG human chorionic gonadotropin

HUA hydroxyurea

hyls1 Hydrolethalus Syndrome Protein 1

IC ionocyte

ICC immunocytochemistry

IFT intraflagellar transport

JmjC Jumonji C

L3MBTL1 Lethal(3)Malignant Brain Tumor-Like Protein 1

MBT mid-blastula transition

MCC multiciliated cell

mci Multicilin

MCI-hGR hormone inducible multicilin

MEF Mouse Embryonic Fibroblasts

MMR Marc's Modified Ringer's solution

n/a not applicable

NF Nieuwkoop and Faber stage

PCR polymerase chain reaction

PHF8 Plant HomeoDomain Finger Protein 8

PTM post-translational modification

RB1 Retinoblastoma protein 1

rfx2 Regulatory Factor X2

RNA ribonucleic acid

seq sequencing

SET Su(var)3-9, Enhancer-of-zeste and Trithorax

SSC small secretory cell

TAD topologically associated domain

tubb Tubulin Beta Class

wt wild-type

ZGA zygotic genome activation

Acknowledgements

It's not very often that you get a chance to publicly thank all of the people who have been there for you over the years, and I plan to make the most of this opportunity. The past five years have been a beautifully collaborative effort, both inside and outside the lab, and I am so grateful to all of the collaborators I've had along the way.

First and foremost, thank you to my supervisor, Prof. Dr. Ralph Rupp for giving me this exciting project and opportunity. I am consistently impressed by your passion for science and your encyclopedic knowledge of *Xenopus* biology. Thank you for your patience, support, and endless enthusiasm in our discussions. It is an honour to be your final student. I am also lucky to work with the best technicians in the business. Thank you, Barbara Hölscher, for your expert embryo stainings and the friendly attitude you bring to the lab every day. Thank you, Edith Mentele, for all of your support (both technical and emotional) with the frog work and for teaching me most of what I know about Bavarian culture. Thank you to Carmen Marthen for being my teammate in frog work and for keeping me entertained with an endless supply of wrestling stories. To my former lab mate, Daniil Pokrovsky, for the mass spectrometry contributions you made to my project, and for visiting so often it feels like you never left. To the former Rupp Lab members Alessandro Angerilli, Dario Nicetto, and Julien Berges, whose findings laid the foundation for the work presented in this thesis.

Thank you to everyone outside the lab who has given me scientific support throughout my PhD. To my TAC, Dr. Eva Hörmanseder and Dr. Tamas Schauer thank you for your valuable scientific insights on my project. Further thanks to Eva for allowing me to visit your lab and tag along on conferences, and to Tamas for his expert RNA-seq analysis. Thank you to Ana Janeva and Meghana Oak for your support in all things ChIP. Thank you to Dr. Tobias Straub for the bioinformatic support, Dr. Andreas Thomae for bioimaging support and instruction, and Dr. Stefan Krebs at LAFUGA for sequencing my samples.

I am also deeply thankful for the larger scientific communities I was a part of during my PhD. Prof Dr. Peter Becker, the community you've built within the Molecular Biology department is remarkable. I am lucky to have been able to work in such a friendly and scientifically stimulating environment. To Dr. Elizabeth Schroeder-Reiter, thank you for always going above and beyond for the IRTG 1064. This program has brought so much extra value to my time here, and the learning opportunities, friendships, and experiences you facilitated have been some of the highlights of my PhD.

Speaking of friendships, I am lucky to have a lot of people in this category to thank. Vera Kleene, Anna Kiss, Nik "Nikipedia" Eggers, Nadia Prayitno, and Iris Langstein-Skora, also known as Nik and the Chicks, thank you for the lunches, coffees, and Deutsch Donnerstag. We went through a very strange time together during the pandemic, and you made me happy to come to the lab every day. To the Greece crew, Gizem Kars, Muhunden Jayakrishnan, and my birthday twin, Fotios "Fotato" Gkountromichos, for being true pals and for finding more and more ridiculous ways to measure units of time. To all of the members of the Molbio department that I've overlapped with through the years; Chondamma, Namisha, Beyza, Lara, Anu, Lorenz and Drin (fellow West Siders), Viola, Angela, Eugenio, Andrea L., Irina, Elisa, Marco, Rupam, Hua Jie, Andrea T., Erika, Toby, Sophia, Jessica, and Freddie (sorry if I forgot anyone). I'm proud to be part of such an intelligent, fun, and diverse group of people. Thank you for all of the departmental seminars, Chromatin Days, International Dinners, impromptu kitchen gatherings, and Mensa visits. I couldn't imagine a better place to land for my PhD.

I also have so many communities and people to be thankful for outside of the BMC. Thank you to the Munich Colmcilles for giving me somewhere to run off my lab frustrations and for the unofficial Irish Pub tour of Europe. What started out as a sport I had never heard of ended up becoming a key part of my life in Munich. To the Canadians for letting us in on your culinary trip around the world and for making home feel a little bit less far away. You are the best possible argument for going to random Facebook meetups.

To Katherine Kokmanian, I am constantly in awe of you. Thank you for not only being one of the smartest people I know but also one of the most fun. To Coach Natasha Turner. We've been unknowingly following each other around our whole lives, it's such a joy that our paths finally converged. Karl Olsen, from Edinburgh to Munich, it's been pretty cool to watch this friendship grow. I can't wait to get the old band back together. Bisous to Clara Hermant. Thank you for always being up for one more beer and for showing me how much I need ping pong in my life. I'm so happy we finally made the time. Rodaria Roussou, thank you for your infectious energy, for being one of the first friends I made in Munich, and for teaching me how to say "Fast Pig" in Greek. Davide Crombie, it's pretty hilarious to come to Germany and meet a guy from East York who hangs out at the Fiery Grill. Thanks for being the fourth person we always imagined in the room. To Hilda Delgado, Munich's foremost Shakira impersonator. Thank you for being one of my most thoughtful and flexible friends. Beth Jenkins, I don't know how I would have made it through the past five years without you. Thank you for being a soulmate friend right from the beginning. You made the toughest times not just bearable, but a lot of fun. To many more Hopfests, DTRHs, and off-season holidays in the future.

Thank you to all of the friends and family who have supported me from far away: Jan Burgess, Micky Burgess, Sammy McGlynn, all of the Taits and Haldimands, Jackie MacDiarmid, James O'Connell, Emma Luker, Jason Asnis, Maddy Peters, Max Beef, Joan Haliburton, Terry Haliburton, Chelsea Campbell, Brent Campbell, Hayley McOstrich, Bre O'Handley, Ellen Austin, Maggie Tait, Katie Dodsworth, Paige Chisholm, Julia Matheson, and Emilie Scott.

The music of Sofia Kourtesis, Adrianne Lenker, Godspeed You! Black Emperor, boygenius, Waxahatchee, Khruangbin, Hermanos Gutierrez, and Beethoven was the soundtrack of my thesis and kept me sane and happy through the longest writing days.

It's not possible to overstate how grateful I am to Luke Haliburton, my partner through it all. Thank you for taking on this journey with me and helping me through some of the biggest challenges of the past five years: climbing mountains, keeping up the motivation, and troubleshooting my LaTeX document. I'm amazed by you as a person and inspired by your dedication, creativity, and sense of adventure. Thank you for everything. I'm so lucky to have you.

To my family, Mom, Dad, Jack, and Lola. The only reason I can go so far away is because I know I have you to come back to. You guys make me brave. You gave me the foundation to be able to see something like this through, and now I'm driving my own bus. I love you, and I owe it all to you.